DEPARTMENT OF PHYSICS
UNIVERSITY OF JYVÄSKYLÄ
RESEARCH REPORT No. 4/2003

DEVELOPMENT OF NEGATIVE ION SOURCES FOR ACCELERATOR, FUSION AND SEMICONDUCTOR MANUFACTURING APPLICATIONS

BY SAMI HAHTO

Academic Dissertation
For the Degree of
Doctor of Philosophy

To be presented, by permission of the
Faculty of Mathematics and Science
of the University of Jyväskylä,
for public examination in Auditorium FYS-1 of the
University of Jyväskylä on September 12, 2003
At 12 o'clock noon.

Jyväskylä, Finland, September 2003

ISBN 978-951-39-3142-1
URN:ISBN:978-951-39-3142-1

Preface

The work done for this thesis was conducted in the Plasma and Ion Source Technology Group at the Lawrence Berkeley National Laboratory (LBNL) in Berkeley, California during years 2001 – 2003. During this time, I was lucky to be part of several interesting and educating projects that any one of could have been included into this thesis. I concentrated on two projects in the field of negative ions when writing down the thesis to have a coherent "plot".

First, I would like to thank Professor Ka-Ngo Leung for giving me the opportunity to work in his group at LBNL. I do not think there is any other place in the world to do ion source research and development ranging through so many different kinds of ion sources and their applications. I also thank him for his guidance and for giving me and my wife the opportunity to work together in the field of ion "sourcery".

I would like to thank Dr. Jani Reijonen for introducing LBNL and Berkeley to me in the beginning. I also thank him of the many fruitful discussions concerning ion sources, or any other subject, for that matter. I also would like to thank everybody working in the Plasma and Ion Source Technology Group, especially Frederic Gicquel, Darlene Hawkins, Dr. Qing Ji, Seaman Jiang, Hanna Koivunoro, Arun Persaud, Dr. Thomas Schenkel and Don Williams for forming such a fun and creative group of people. I like to acknowledge the mechanical and electrical workshop for their support in all the aspects of making the ideas to become reality: Jerry Fisher, Tom McVeigh, Steve Wilde and Paul Wong.

I would like to thank the Department of Physics in the University of Jyväskylä for giving me the opportunity to do my thesis research and some graduate studies in LBNL and UC Berkeley. I was lucky to be involved in the H^- project in the Jyväskylä Cyclotron laboratory during 1999 – 2000 when I was doing my Master thesis. This opened to me the world of ion sources and gave me a solid background education that made the PhD research a much more enjoyable experience. I especially would like to thank professor Esko Liukkonen for handling all the issues related to having my thesis reviewed and accepted.

I like to thank the Finnish Academy of Science and Letters; Vilho, Yrjö and Kalle Väisälä Foundation for their continuing financial support. The work was supported by the U.S. Department of Energy under Contract No. DE-AC03-76SF00098 and by Axcelis Inc.

I thank my family: my father, mother, brother and sister for their encouragement and support in all stages of my physics studies in Jyväskylä and in Berkeley.

Biggest gratitude I direct to my wife Sari, who has been there every step of the way: your love, understanding and support at home and participation in the actual research has made this a wonderful and unique experience.

Berkeley, August 2003

Sami Hahto

Abstract

The applicability of heavy negative ions as the drivers of inertial confinement fusion and for ion implantation applications was studied in the Plasma and Ion Source Technology Group at the Lawrence Berkeley National Laboratory (LBNL). In heavy fusion applications, negative ions provide a way of producing a totally space charge neutralized beam of stripped, neutral particles, thus avoiding charged-particle beam instabilities. An ion source experiment was set up to demonstrate the applicability of heavy negative ions for fusion driver beam applications. The source design and measurement results with negative chlorine and oxygen ions are presented. In ion implantation, the charging up of the target material can be avoided by using negative ions instead of positive ones. Boron is the most commonly used dopant in manufacturing of p-type semiconductors. A sputtering type, surface production ion source capable of producing commercially applicable amounts of negative boron ions was constructed and tested. A new design using an external RF antenna and non-cesiated source operation was implemented. Technical description of the ion source and achieved results are presented.

Contents

1. Introduction

Ion source technology, or more familiarly “ion sourcery”, has developed in the last two decades in many aspects. Traditionally ion sources are the feeders of charged particles to ion accelerators and storage rings. While this task is very important in the given field of nuclear and particle physics, as the ion source is often the limiting factor for the beam current and quality, in many respects ion sources are lacking more general applications which would manifest themselves in our everyday life. Since these early days, many uses have been found to particle accelerator other than nuclear or particle physics. Medical isotope production has increased the need for cyclotrons, with the accompanying ion sources. Large proton accelerators producing intense neutron beams for applications in basic research and applied sciences have been either constructed or are under way. In each case, the first and maybe the most important, part is the ion source.

New applications for ion sources have emerged in integrated circuit technology in recent years. In order to continue the trend of doubling the amount of transistors per integrated circuit every couple of years, new technologies are required to miniaturize the feature sizes. Ion sources play their part in this development, as ion projection lithography and focused ion beams are currently studies as the future lithographic tools for semiconductor industry.

Neutrons are needed in cancer treatment facilities in boron neutron capture therapy (BNCT). Traditionally the neutron flux is provided by a reactor or a large accelerator, which require big infrastructure around them and are not adaptable to hospital environment. Increased need for cargo screening techniques in airports and harbors has led to investigation of suitability of neutrons to this application. In all the above mentioned cases compact, ion source based deuterium accelerators are proposed as being the neutron generators.

The work done for this thesis was concentrating on the development of negative volume and surface ionization sources for heavy ion fusion and semiconductor industry applications. In both cases, the performance of the ion source will be the determining factor when negative ions are being considered for future fusion and lithography machines.

2. Properties of plasma

2.1 Definition of plasma

Plasma is often called the fourth state of matter, the others being solid, liquid and gaseous states. Plasma can be found in a huge variety of phenomena in the universe, from the flame of a candle to a core of a star. Over 99 % of the visible mass of the universe exists as plasma.

Plasmas are an essential part in all ion sources, as plasma provides an easy way of creating and controlling ion beams. The work described in this thesis is focused on volume and surface ion sources based on RF ionization.

A commonly used definition for plasma is the following: plasma is a quasineutral gas of ions, electrons and neutral gas molecules, which exhibits collective behavior when exposed to external electromagnetic forces. Usually a plasma has a zero net electric charge like neutral gas. The biggest difference between plasma and neutral gas are the quite freely moving charged particles, which make plasma a very good conductor, unlike neutral gas. This means that plasma behavior is dominated by macroscopic electric and magnetic forces, which don't have any effect on neutral gas.

The high mobility of the ions and especially electrons give rise to the collective behavior exhibited by plasmas. The best example of this behavior is the tendency of plasma to shield external electric fields so that the effect of the field is only felt by very few plasma particles in a small volume compared to the volume of the whole plasma. Also an important fact is that the flow of charged particles in plasma gives rise to electric currents, which in turn induce magnetic fields. These fields cause an "action at a distance"- force that manifests itself in a wide variety of phenomena in plasma.

2.2 Thermal properties of plasma

2.2.1 Temperature of plasma

Kinetic energies of plasma particles in thermal equilibrium follow the Maxwellian distribution[1]:

$$f(v_x, v_y, v_z) = n\left(\frac{m}{2\pi kT}\right)^{3/2} e^{-\frac{1}{2}m(v_x^2+v_y^2+v_z^2)/kT} \quad (1)$$

where n is the gas density, m is the particle mass, k is Boltzmann's constant, T is the plasma temperature and $v_{x,y,z}$ are the velocity components along the three coordinate axis.

Using equation (1) the mean energy of a plasma particle can be calculated to be

$$\overline{E} = \tfrac{3}{2}kT \tag{2}$$

which is divided equally between the three degrees of freedom x, y, and z,

$$\overline{E}_x = \overline{E}_y = \overline{E}_z = \tfrac{1}{2}kT \tag{3}$$

A common practice is to define the ion end electron temperatures in a plasma using electron volts (eV) instead of Kelvins. The temperature corresponding to the energy of 1 eV can be calculated using eq. (2),

$$1\,eV = kT \Rightarrow T = \frac{e}{k} = \frac{1.602 \cdot 10^{-19}}{1.38 \cdot 10^{-23}} = 11600\ \mathrm{K} \tag{4}$$

The term 3/2 was left out of equation (4) to get a definition of temperature, which is independent of the number of degrees of freedom.

Plasma temperature is somewhat misleading concept, as both the electrons and the ions have their own Maxwellian distribution and, thus, temperature. This can arise from the fact that the electrons collide more often with other electrons than with ions, and therefore the thermal distributions of ions and electrons never reach a common equilibrium distribution. In the presence of a magnetic field, even single particle species can have two different temperature components corresponding to the velocity components parallel and transverse to the magnetic field.

2.2.2 Degree of ionization of plasma

The degree of ionization of plasma is the ratio of the ion and neutral particle densities. An estimate for the degree of ionization for plasma, which is in thermal equilibrium, can be obtained from the so-called Saha- equation[2]

$$\frac{n_i}{n_n} \approx 2.4 \cdot 10^{15} \frac{T^{3/2}}{n_i} e^{-\phi_i / kT} \tag{5}$$

where n_i and n_n are the ion and neutral particle densities [1/cm^3], T is the plasma temperature [K] and ϕ_i is the ionization energy of the ion [eV].

2.3 Electric properties of plasma

2.3.1 Debye length

When an external electric field is introduced into the plasma, the ions and electrons move out to cancel the field. Plasma particles form a layer, a sheath, within which the electric field is attenuated almost to zero so that the plasma particles outside the sheath do not feel the electric field. The potential of an electrode that is introduced into the plasma is given by equation (6).

$$V(x) = V_0 \cdot e^{-\frac{x}{\lambda_D}} \qquad \text{[V]} \tag{6}$$

where V_0 is the potential of the electrode, x is the distance from the electrode and λ_D is the so called *Debye*- length. It is the distance from the electrode at which the potential is decreased to one over e times V_0 . λ_D is given by equation (7)

$$\lambda_D = \sqrt{\frac{kT_e\varepsilon_0}{e^2 n_e}} = 6.9 \cdot \sqrt{\frac{T_e}{n_e}} \qquad \text{[cm]} \tag{7}$$

where T_e is the electron temperature [K], ε_0 is the permittivity of empty space and n_e is the electron density [1/cm^3].

In figure 1, the exponential part of equation (6) is plotted as a function of x/λ_D. It can be seen that the voltage of the electrode immersed in plasma is attenuated to 1 % of the original value after about 4 Debye lengths.

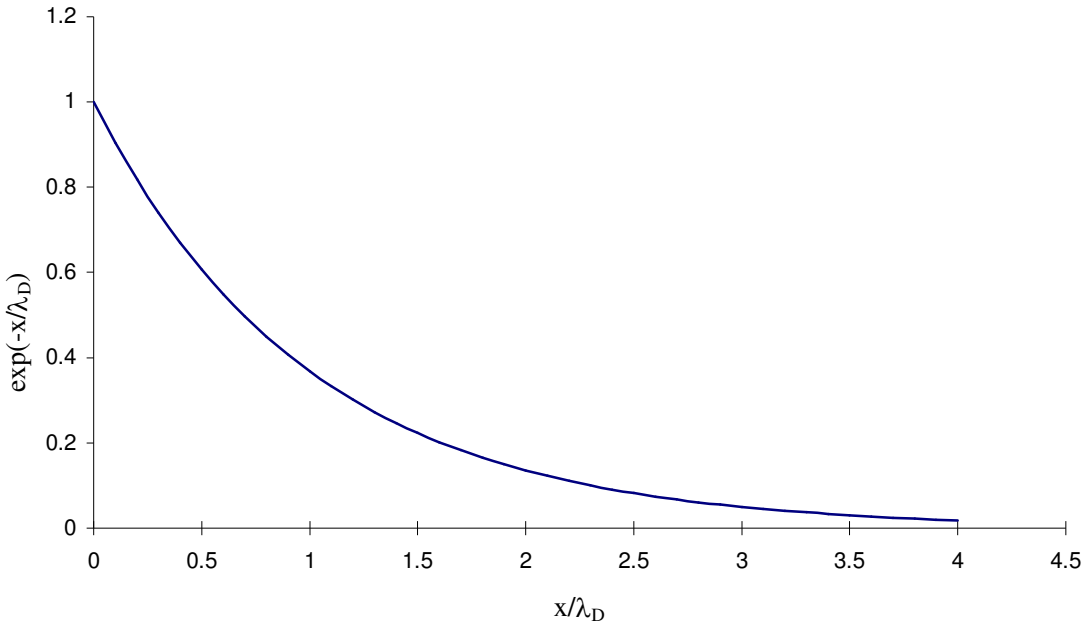

Figure 1*. The voltage of an electrode immersed in plasma as a function of the distance from the electrode.*

2.3.2 Plasma potential

When plasma is contained in a vessel the plasma particles collide with the vessel surface. Electron flux that the surface intercepts is higher than the ion flux because of the much higher mobility of electrons. This can be seen by writing a formula describing the current density of charged particles

$$j = nqv \tag{8}$$

where j is the current density of the charged particles intercepting the surface, n is the particle density, q is the electric charge of the particle and v is the particle velocity. In typical plasma the densities and charge states of the electrons and ions are usually the same. The velocity of an electron is larger than that of an ion by the ratio of the square root of their masses.

The fact that the electron current hitting the wall is much larger than the ion current leads to plasma assuming a positive potential relative to the vessel wall. This is usually in order of 5 – 15 V [3]. If the vessel is biased to some voltage, the plasma floats on top of that voltage by the value of plasma potential.

2.3.3 Charge neutrality

Plasma is usually considered to have a zero net charge. The charge neutrality can be written:

$$e\left(\sum Qn_{ip} - \sum Qn_{in}\right) - en_e = 0 \tag{9}$$

where Q is the charge state of the ion and the sum is taken over all the charge states of positive and negative ions and term n is the corresponding particle density. Plasma follows equation (9) to a very high degree if the plasma meets some basic requirements that are stated in equation (10)

$$\lambda_D << L,\ N_D >> 1,\ \omega\tau > 1 \tag{10}$$

where L is the dimension of the plasma, N_D is the number of charged particles inside a sphere of radius λ_D, ω is the plasma frequency and τ is the mean time between ion and neutral particle collisions.

Equation (10) states that the dimension of the plasma has to be large compared to the Debye length and that the charged particle density has to be large enough to enable the plasma to behave in a statistical, collective way. The last term in equation (10) indicates that the degree of ionization has to be sufficiently high, otherwise the plasma behavior will be governed by ion-neutral particle collisions.

2.3.4 Plasma frequency

When the charge neutrality of the plasma is disturbed, the plasma particles react by exerting a restoring force and try to reach a new equilibrium state. This restoring force results in oscillations of electrons and ions in the plasma. Usually the term plasma frequency is applied to the characteristic frequency with which the electrons are oscillating, as the ion oscillations are of lesser importance due to their much higher mass and thus lower mobility. The electron plasma frequency is defined by [1]:

$$\omega_{pe}^2 = \frac{e^2 n_e}{\varepsilon_0 m_e} \tag{11}$$

where ε_0 is the permitivity constant, n_e and m_e are the electron density and mass, respectively. This can be written in more usable form

$$f_{pe} = 8980\sqrt{n_e} \qquad \text{[Hz]} \tag{12}$$

In equation (12) the electron density n_e is in 1/cm^3.

Usually in plasma the electron plasma frequency is in gigahertz range. By substituting to equation (11) the ion plasma frequency can be calculated to be

$$f_{pi} = 210 \cdot Q\sqrt{\frac{n_i}{A}} \qquad \text{[Hz]} \tag{13}$$

where Q is the charge state of the ion, n_i is the ion density in 1/cm^3 and A is the ion mass number.

2.4 Magnetic properties of plasma

Magnetic fields have a fundamental importance in plasma physics and technologies based on the use of plasma. The electric conductivity of plasma is extremely good due to the high mobility of the plasma particles. This leads into the tendency of plasma to "freeze" magnetic field lines. If a plasma is created in a volume with an existing magnetic field and the field is later on changed somehow, there will be currents induced in the plasma that tend to maintain the original magnetic field profile. On the other hand an external magnetic field can't penetrate into plasma as the induced plasma surface currents will cancel the field.

Ion source technology benefits greatly from the above mentioned facts and that plasma seeks the volume containing the minimum magnetic field. This provides an easy way of controlling and creating plasmas.

2.4.1 Cyclotron frequency

The equation of motion for a charged particle in an electromagnetic field can be written in a form

$$m\frac{d\bar{v}}{dt} = q(\bar{E} + \bar{v} \times \bar{B}) \tag{14}$$

which in absence of electric field reduces to

$$m\frac{d\bar{v}}{dt} = q\bar{v} \times \bar{B} = qvB\sin\theta \tag{15}$$

where $\bar{v}$, m and q are the particle velocity, mass and charge, $\bar{E}$ and $\bar{B}$ are the electric and magnetic field vectors, B is the flux density of the magnetic field and θ is the angle between the velocity and magnetic field vectors.

Equation (15) indicates that the force the magnetic field exerts on a charged particle depends only on the velocity component transverse to the field. The direction of the force is transverse to both magnetic field and particle velocity vectors and acts thus as a central force for a circular motion. Particle velocity component parallel to the magnetic field is unaffected by the field and the particle can move freely along the magnetic field line in a spiral motion.

The relation between the central and magnetic forces can be written

$$m\frac{v_{\perp}^{\ 2}}{r} = qv_{\perp}B \tag{16}$$

where m is the particle mass, $v_{\perp}$ is the particle velocity component transverse to the magnetic field, r is the radius of the particle motion around the magnetic field line.

The frequency with which the charged particle rotates around the magnetic field line is called *the cyclotron frequency* and is given by

$$\omega_c = \frac{|q|B}{m} \tag{17}$$

This can be written in more convenient form for ions as follows

$$f_{ci} = 15.2 \cdot \frac{QB}{A} \qquad \text{[MHz]} \tag{18}$$

and for electrons

$$f_{ce} = 28 \cdot B \quad \text{[GHz]} \tag{19}$$

In the above equations Q is the ion charge state, A is the ion mass number and B is the magnetic field in teslas.

The *gyroradius,* or the so called *Larmor* radius, of the particle's circular motion around the field lines is given by

$$r_L = \frac{v_\perp}{\omega_c} = \frac{mv_\perp}{|q|B} \tag{20}$$

One thing to be noted about the circular motion of charged particles in a magnetic field is that the direction of the rotation is such that the magnetic moment of the particle motion is pointing to opposite direction of the magnetic field vector and plasma is thus weakening the magnetic field and acting as a diamagnetic material. Figure 2 shows the ion and electron trajectories in transverse magnetic field.

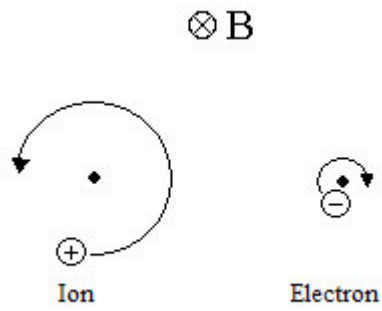

Figure 2*. Charged particle trajectories in transverse magnetic field*

2.4.2 Diffusion of charged particles in a magnetic field

Plasma particles are constantly interacting with each other. The charged particles are primarily interacting through Coulomb force while neutral particles are experiencing both elastic and inelastic collisions with each other and the ions and electrons. The particle motion is described by a diffusion equation, which gives the relation between the time and space variation of the local particle density. It can be written[4]:

$$\frac{\partial n}{\partial t} = \overline{\nabla} \bullet (D\overline{\nabla} n) \tag{21}$$

where n is the local plasma particle density and D is the diffusion coefficient.

Often there is a magnetic field present in the plasma and we have to consider the constant D in equation (21) in both parallel and transverse directions to the magnetic field. Particle diffusion rate along the magnetic field lines depends on the thermal velocity of the particle and the rate of collision with other particles. The parallel diffusion coefficient can be written in form[5]

$$D_{\parallel} \approx \frac{v_{th}^2}{f} \tag{22}$$

where v_{th} is the particle thermal velocity and f is the collision frequency.

In transverse direction to the magnetic field, the diffusion of charged particles arises from collisions with the neutral particles. As the charged particles are rotating around the magnetic field lines, the collisions with the neutral particles will change the phase of the rotation. This will lead to a gradual shifting of the center of the rotation and the particle will diffuse transversely through the magnetic field. Figure 3 presents the diffusion through transverse magnetic field.

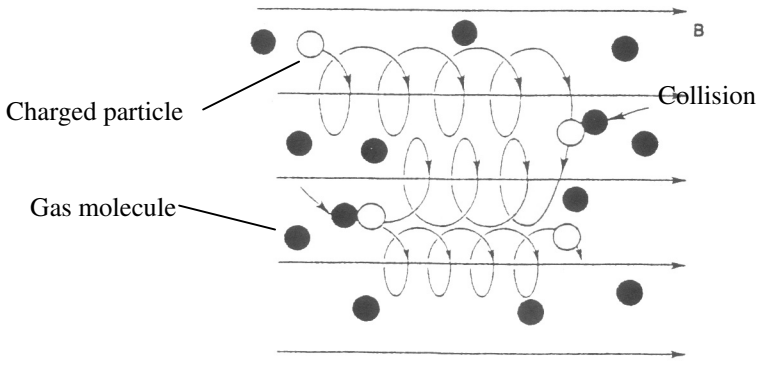

Figure 3*. Diffusion of charged particles through a transverse magnetic field*

In a typical ion source plasma (plasma density between 10^{10} – 10^{12} cm^{-3}) in the presence of magnetic fields the cyclotron frequency of the charged particles is much higher than

the collision frequency with other particles. In this case the transverse diffusion coefficient is given by[5]:

$$D_{\perp} = v_{th}^2 \frac{f}{f^2 + \omega_c^2} \approx f \frac{v_{th}^2}{\omega_c^2} = f \cdot r_L^2 \sim f \cdot m^2 \tag{23}$$

where r_L is the particle gyroradius and m is the particle mass. Equation 23 indicates that in a transverse magnetic field, the ion diffusion coefficient is much higher than the corresponding value for electrons.

2.4.3 Plasma confinement with magnetic fields

Plasma confinement is an important part in research and applications of plasma. It provides a way to control the shape and size of the plasma volume and slow down the loss rate of plasma particles. Often the easiest way to do this is to use magnetic fields.

When a charged particle moves in magnetic field it has a magnetic moment, which is given by equation

$$\mu = \frac{1}{2} \frac{m v_{\perp}^2}{B} \tag{24}$$

Particle's magnetic moment is a constant as well as the total kinetic energy E_k. The kinetic energy arising from the velocity component parallel to the field is given by

$$\frac{1}{2} m v_{\parallel}^2 = E_k - \mu B \tag{25}$$

From equation (25) we can see that when the particle with a non-zero transverse velocity component $v_{\perp}$ moves towards a stronger magnetic field region the parallel velocity component $v_{\parallel}$ will decrease. If the magnetic field is strong enough, the particle will be reflected back.

The most commonly used magnetic field geometries are the magnetic bottle, which is widely used in the Electron Cyclotron Resonance or ECR ion sources, and the so called multicusp magnetic field, which is typically used in bucket type ion sources. In both of

these geometries, the plasma is occupying a minimum magnetic field volume and is surrounded by stronger field regions.

In figure 4 a schematic of the magnetic bottle and multicusp field is presented.

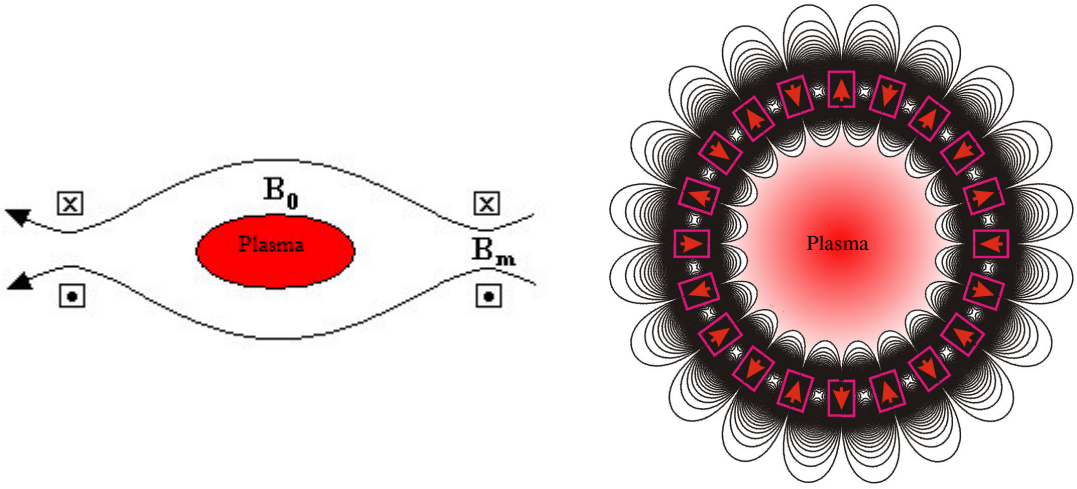

Figure 4*.(a) Magnetic bottle created by two coils. (b) Multicusp magnetic field*

Magnetic bottle is efficient in containing plasma with minimal losses. The losses are happening mainly through a small area at the ends of the bottle, through which the ion extraction is also done. This area has a magnetic field maximum, which decreases the beam quality. Plasma is confined in the minimum field region in the middle. The so called mirror equation gives the conditions for the trapping of the plasma particles

$$\frac{B_0}{B_m} = \sin^2(\theta) \tag{26}$$

where B_0 and B_m are the minimum and maximum magnetic field values. θ is the minimum angle between the particle velocity and magnetic field vectors for the particle to be trapped in the bottle.

In a multicusp magnetic configuration, permanent magnets are lined around the plasma chamber with alternating pole faces towards the plasma [6]. The Plasma is contained in the field free region at the center. This produces a large and uniform plasma distribution. Ions are extracted from the center of the plasma with minimal disturbances from the magnetic field.

The plasma is normally uniform in an area where magnetic field is less than 25 gauss[7].

Losses in multicusp field will happen through the cusp lines, RF antenna or filament surface and any exposed container surfaces that are not covered by a magnetic field. The lost particle density in unit time can be written[8]

$$\frac{dn}{dt} = nv\frac{S_{cusp} + S_{surface}}{V} \tag{27}$$

where n is the plasma density, v is the ion or electron average velocity, S_{cusp} and $S_{surface}$ are the loss areas through cusp lines and other surfaces, respectively, and V is the plasma volume.

The cusp loss area S_{cusp} is given by equation

$$S_{cusp} = L_{cusp} w \tag{28}$$

where L_{cusp} is the total length of the cusp lines and w is the so called cusp loss width, which is approximately[9]

$$w \approx \frac{\sqrt{m^{1/2} p}}{B} \tag{29}$$

In equation (29) m is the particle mass, p is the plasma pressure and B is the average magnetic field.

3. Formation of plasma

Most of the plasmas formed in laboratory conditions are generated using energetic electrons to knock the electrons out of neutral atoms. This is by far the easiest way of ionizing neutral gas, as electron mobility is high and the cross sections for electron – electron impact between the atomic and ionizing electrons are fairly high. Also the electrons that are knocked from the atomic orbitals become themselves ionizing particles if excited by some means, which minimizes the need for constant supply of ionizing electrons.

Most commonly used plasma formation processes are DC discharge, radio frequency (RF) and microwave ionization [1]. In the work done for this thesis the emphasis was on RF ion sources.

3.1 Arc discharge

Traditionally arc discharge has been the most popular way of ionizing gas and forming plasma. In principle arc discharge ion source consists of an electron emitting cathode and an anode, between which the material that is being ionized is injected in gaseous form. Usually the cathode is a filament, which is heated by driving electric current through it. The anode is positively biased with respect to the cathode. This voltage difference forms an electric field that accelerates the electrons that are ejected from the hot filament and they ionize the neutral atoms and molecules of the gas.

The current density of the electrons emitted from the filament is given by the following equation[10]

$$j = 120 \cdot T^2 e^{-\frac{\phi}{kT}} \qquad [\mathrm{A/cm^2}] \tag{30}$$

where ϕ is the work function of the filament material in Joules and T is the temperature of the filament in Kelvins.

When an electron is emitted from the filament, it is accelerated by the electric field created by the voltage between the cathode and the anode. The accelerating electric field affects the electron only in the few Debye lengths wide sheath that is formed around the filament. The electrons do not gain any energy after they leave the sheath, which means that after they lose enough kinetic energy in collisions in the plasma, they cannot ionize any more neutral particles. The secondary electrons emitted from the atoms usually do

not have enough energy to ionize the gas, which means that there has to be a constant supply of hot electrons from the filament. This limits the filament lifetime and the efficiency of the discharge.

3.2 Formation of plasma using RF field

A more elegant way of forming plasma is by using radio frequency (RF) electromagnetic field to heat the cold electrons. This is done by driving RF current in an antenna coil, which is immersed in the plasma volume or wrapped around the plasma container. The varying current in the antenna induces a varying magnetic field, which in turn induces an electric field. This electric field accelerates the free electrons in the neutral gas to high enough energies to start the discharge and form plasma.

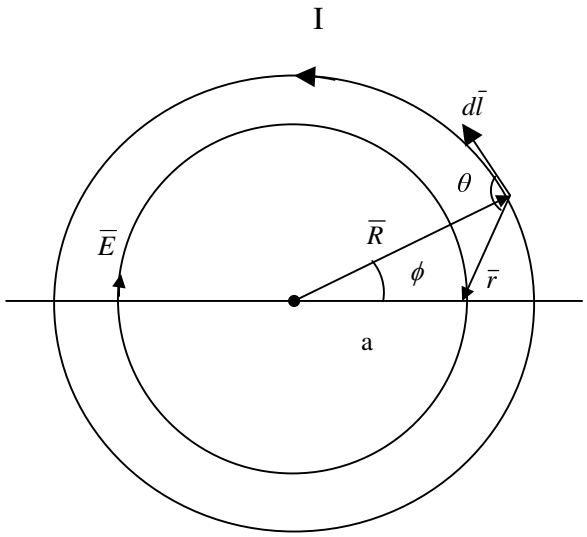

***Figure 5**. Current loop with radius R.*

Let's examine more closely the magnetic and electric fields induced in vacuum by an RF antenna loop presented in figure 5. The current is given by

$$I(t) = I_0 \sin(\omega t) \tag{31}$$

where I_0 is the amplitude of the current and ω is the angular frequency of the RF field.

The magnetic force at a distance *a* from the center of the loop is given by the law of *Biot-Sawart*:

$$d\bar{B} = \frac{\mu_0 I \cdot dl \cdot \sin(\theta)}{4\pi \cdot r^2} = \frac{\mu_0 I \sin\theta \cdot R d\phi}{4\pi \cdot r^2} \tag{32}$$

where θ is the angle between the vectors $d\bar{l}$ and $\bar{r}$, R is the radius of the loop and r is the distance from the point of interest to the infinitesimal current element *dl*. The magnetic field vector points up from the plane of the paper in figure 5.

By stating θ and r as a function of ϕ equation (32) can be written in form

$$dB = \frac{\mu_0 I \cdot \sin\left[\frac{\pi}{2} + a\sin\left(\frac{a \cdot \sin(\phi)}{\sqrt{(R\cdot\cos(\phi) - a)^2 + (R\cdot\sin(\phi))^2}}\right)\right] \cdot R \cdot d\phi}{4\pi\left[(R\cdot\cos(\phi) - a)^2 + (R\cdot\sin(\phi))^2\right]} \tag{33}$$

By integrating equation (33) from $\phi = 0$ *to* $\phi = 2\pi$ the magnetic field at any point in the plane of the loop can be solved. The induced electric and magnetic fields are related by the second Maxwell's equation:

$$\bar{\nabla} \times \bar{E} = -\frac{\partial \bar{B}}{\partial t} \tag{34}$$

By solving equation (34) in cylindrical coordinates we get

$$\frac{\partial E_\phi}{\partial r} = -\frac{\partial B(r)}{\partial t} = -B_0(r)\omega\cos(\omega t) \tag{35}$$

where B_0 is the amplitude of the magnetic field. As a practical example let's define electric and magnetic field values of a single loop RF antenna with 4 cm radius and RF frequency of 13.56 MHz. Let's assume that the current amplitude I_0 is 40 A corresponding to about 1600 W of RF power. In figure 6 the magnetic field values

starting from the center of the loop are plotted. The calculation was made by solving equation (33) with MathCAD calculation software[11].

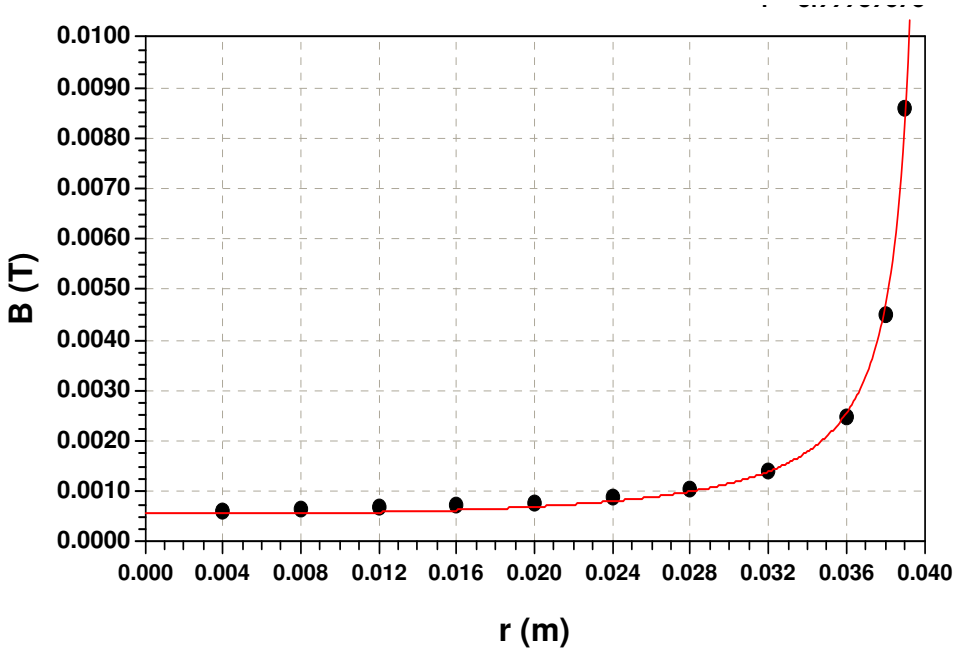

Figure 6. *Magnetic field B_0 at the plane of a current loop with 4 cm radius and 40 A of current.*

For practical electric field calculations an inverse quadratic equation is fitted in to the data points of figure 6. By letting this function to present the magnetic field, equation (35) becomes

$$\frac{\partial E_\phi}{\partial r} \cong -\frac{1}{a+b\cdot r+c\cdot r^2}\omega\cdot\cos(\omega t) \Rightarrow E_\phi = \frac{2\omega}{\sqrt{4ac-b^2}}\operatorname{atan}\left(\frac{2c\cdot r+b}{\sqrt{4ac-b^2}}\right) \tag{36}$$

where a, b and c are the coefficients of the fitted inverse quadratic equation and r is the distance from the center of the current loop. In figure 7 the calculated electric field amplitude E_0 based on the figure 6 magnetic field is plotted.

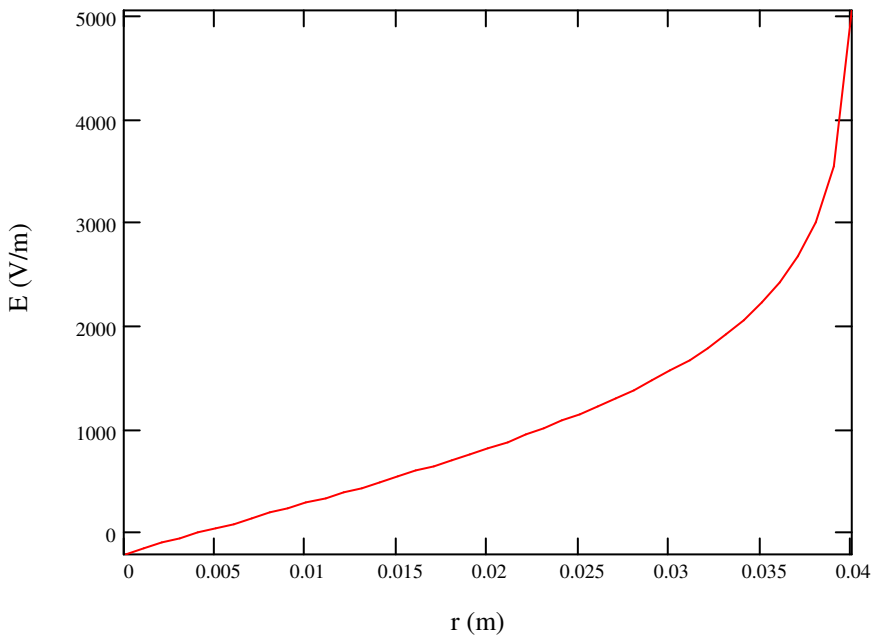

***Figure 7**. Electric field amplitude as a function of distance from the center of the loop, loop current I = 40 A and RF frequency f_{RF} = 13.56 MHz.*

From figure 7 it can be seen that the electric field is nearly zero at the center of the antenna loop. The field increases almost linearly up to 2.5 cm radius, after which it increases rapidly. The electric field distribution indicates that the RF field is creating most of the energetic electrons that are ionizing the gas relatively close to the antenna conductor.

Electron equation of motion in an RF electric field is

$$m\frac{dv}{dt} = eE_0 \sin(\omega t) \tag{37}$$

for which the solution is

$$v(t) = v_0 - \frac{eE_0}{m\omega}\cos(\omega t) \tag{38}$$

where E_0 is the amplitude of the electric field. In the above calculations the phase of the RF field is assumed to be zero.

As an example let's take the electric field value of 2 kV/m at r = 3.5 cm from figure 7 and solve the equation (37) for electrons accelerated by 13.56 MHz RF field. In figure 8 the

solved electron velocity and kinetic energy are plotted. An initial kinetic energy of 5 eV was used for the electrons.

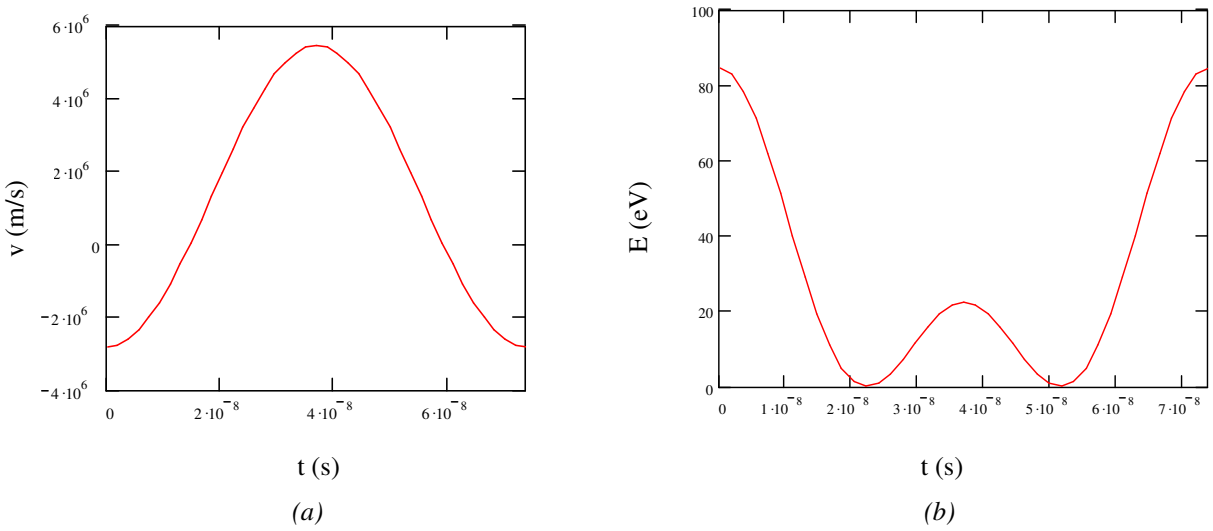

***Figure 8**. Electron velocity and kinetic energy during 13.56 MHz RF cycle calculated using 2 kV/m electric field amplitude and 5eV electron background energy.*

From figure 8 we can see that the electron kinetic energy has a maximum of about 80 eV. We have to average the kinetic energy over one RF cycle to get an idea of the ionization efficiency of the electron. The average kinetic energy in the case of figure 8 is 30 eV. This is higher than the first ionization energy of most elements.

An interesting result that is obtained from equation (38) is that the average kinetic energy over one RF cycle is the same for all RF frequencies. This is due to the fact that the ratio E_0/ω stays constant.

It must be noted that in the presence of plasma the magnetic and electric fields induced by the RF are partially shielded by the plasma particles [57]. This dampens the amplitude of the B- and E- fields and smoothes the curves in figures 6 and 7. This means that the ionizing, hot electrons are formed closer to the chamber wall than indicated by the above calculations. The penetration depth of the RF fields increase with decreasing RF frequency and the field profiles are fairly similar in vacuum and plasma at RF frequencies below 2 MHz.

Traditionally 2 MHz RF field has been used in RF ion sources[12]. Plasma ignition has to be initiated in the 2 MHz case by injecting electrons from a filament or by other means[13]. Higher frequencies, typically 13.56 and 27.12 MHz, can ignite the plasma by themselves. Higher frequency RF fields have enough time to accelerate free electrons between the electron-neutral collisions to sufficiently high energies to start up the discharge. This will be described in more detail in section 3.1.

In order to heat the plasma with RF fields, the RF current has to be matched with a matching network to maximize the power loss to the plasma. In figure 9, two different types of matching networks are presented schematically.

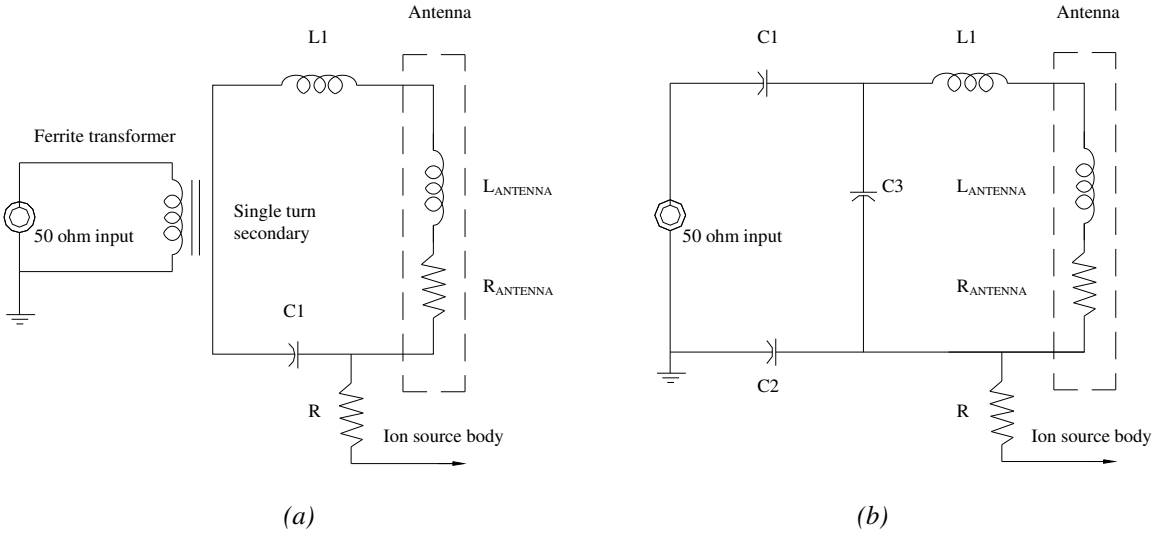

***Figure 9**. Schematic of (a) inductive and (b) capacitive matching networks*

Figure 9 (a) presents an inductively coupled network that uses a ferrite transformer to drive a series resonant circuit in the secondary that includes the antenna. The 50 ohm output impedance of the RF power supply is matched to the antenna by adjusting the transformer turn ratio and tuning the capacitor. This type of matching network suffers from somewhat poor efficiency due to the losses in the transformer especially at high RF power levels.

Figure 9 (b) presents a more recent development in matching network design[14]. It matches the RF power to the antenna through a capacitive voltage divider. The capacitive network has been found to operate at much higher efficiency than the inductive one at low RF frequency (2 MHz)[14]. At higher frequencies the two networks are comparable.

4. Ion formation in plasma

4.1 Positive ions

Most of the positive ions in laboratory plasmas are created by bombarding neutral gas with energetic electrons. The condition for ionization is that the kinetic energy of the ionizing particle is larger than the binding energy of the atomic electron that it is interacting with. This can be written in from

$$E_e > e\phi_i \tag{39}$$

where ϕ_i is the first ionization potential of the neutral atom.

Figure 10 shows the first ionization energies of all elements. The periodic behavior is clear, as the ionization energy gets bigger towards the noble gases in each group of the periodic table of elements.

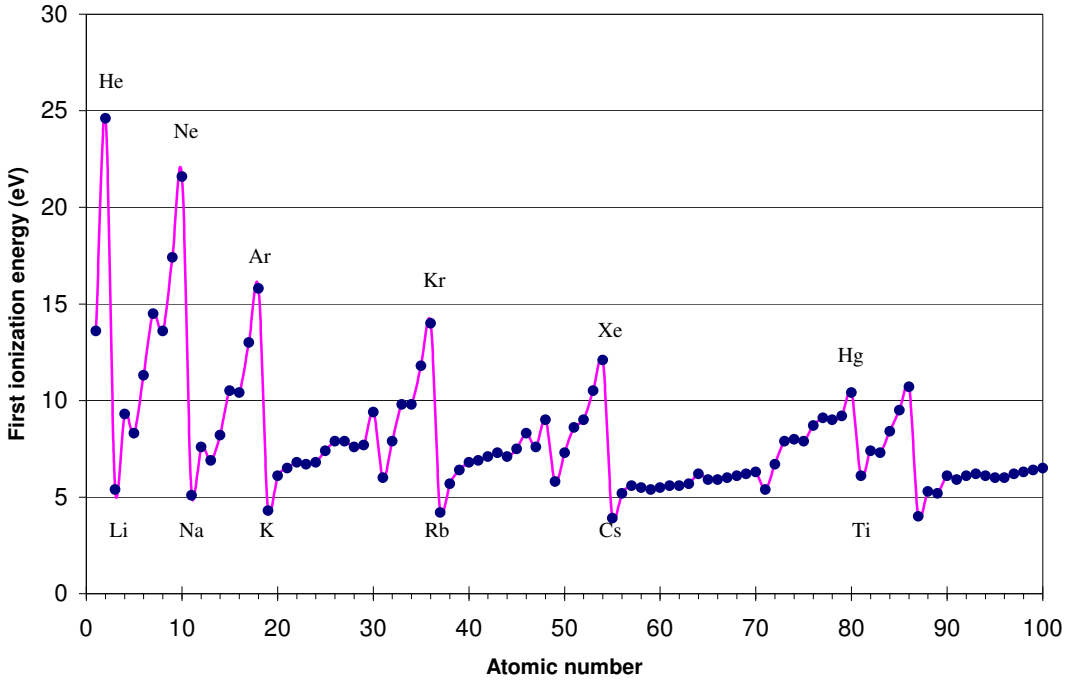

***Figure 10**. First ionization energies of the elements*

The ionization energies fall between 5 and 25 eV for all elements. The probability of ionization by electron impact varies with the incident electron energy. The cross section starts from zero at the ionizing electron energy equal to the ionization potential and has a maximum at around 2 to 4 times the first ionization potential. In figure 11 the ionization cross sections are presented as a function of the electron energy for some commonly used gases[15].

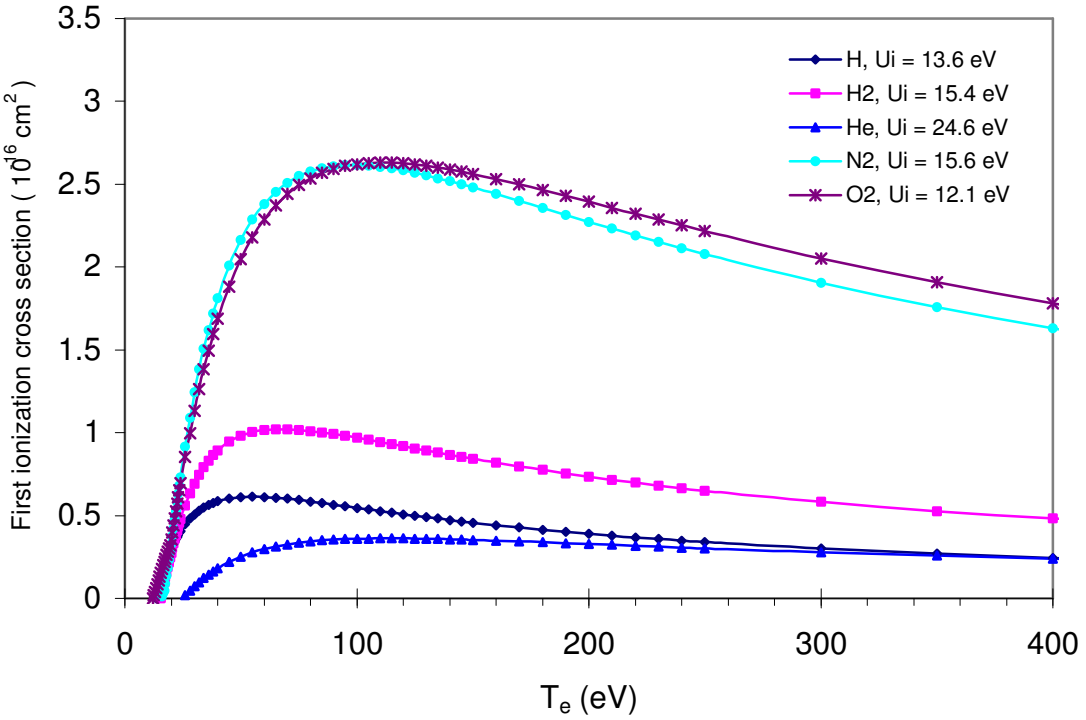

***Figure 11**. First ionization cross sections by electron impact for H, H_2, He, N_2 and O_2 as a function of ionizing electron energy*

The mean free path of the electron can be calculated using the following expression

$$\lambda = \frac{1}{n\sigma} = \frac{kT}{P\sigma} \qquad \text{[m]} \tag{40}$$

where n and σ are the neutral gas density and ionization cross section, P is the neutral gas pressure in units Pa, T is the gas temperature in K and k is the Boltzmann's constant.

As an example let's calculate the mean free path for an ionizing electron in hydrogen gas. We assume that the average electron energy over one RF cycle is 60 eV, which would approximately correspond to a two loop antenna with the diameter and RF current

described in the example in section 2.2. From the data of figure 11 we see that the ionization cross section for 60 eV electron in H_2 gas is $1 \cdot 10^{-16}$ cm^2. If the neutral gas is in room temperature and has a pressure of 10 mTorr, or 1.33 Pa, we get from equation (40) a mean free path of 30 cm for the electron. This is clearly quite large value compared to the dimensions of most ion sources. This indicates that a good electron confinement is needed in order to ignite and maintain a low pressure discharge in a hydrogen plasma. At higher pressure the mean free path of an ionizing electron decreases and plasma becomes easier to ignite and maintain.

Different RF frequencies cause the electrons to have different displacements during one RF cycle. As a comparison let's use the same antenna geometry and current mentioned above. We can integrate equation (38) over one half cycle and get the maximum displacement of an electron for different RF frequencies. With the values used above we obtain for the electrons at 3.5 cm radius in the antenna loop a displacement of 70 cm, 10 cm and 5 cm for 2 MHz, 13.56 MHz and 27.12 MHz RF frequencies, respectively. This explains why higher frequency RF field is capable of igniting and maintaining the plasma at lower pressure.

In a typical plasma chamber with about 10 cm diameter and length the electrons would be lost to the walls in the case of 2 MHz RF unless the gas pressure is in the range of hundreds of mTorr. For 13.56 MHz, the pressure range of a few tens of mTorr should be low enough for the ignition of plasma and for 27.12 MHz the displacement of electrons by the RF field is smaller than the source dimension so the electrons can oscillate back and forth without hitting the container walls and thus travel long enough path to ionize neutral atoms even at less than 10 mTorr pressure.

If the gas being ionized is mono atomic, like all noble gases, there is usually only singly ionized atomic ions present in the plasma. The ionization reaction can be written

$$A + e_f \rightarrow A^+ + 2e \tag{41}$$

where A is the gas atom and e_f is the hot ionizing electron.

If the source gas is molecular, the reaction described in (41) can become much more complicated. If we have a diatomic gas, the possible ionization reactions are

$$\begin{aligned}
&(a) \quad A_2 + e_f \rightarrow A_2^+ + 2e \\
&(b) \quad A_2 + e_f \rightarrow A^+ + A + 2e \\
&(c) \quad A_2^+ + e_f \rightarrow A^+ + A + e \\
&(d) \quad A + e_f \rightarrow A^+ + 2e \\
&(e) \quad A_2^+ + A_2 \rightarrow A_3^+ + A
\end{aligned} \tag{42}$$

The abundance of each ion species in (42) depends on the plasma parameters, such as neutral gas pressure, RF power and magnetic field configuration. If the gas pressure is high, reactions 42 (a) and (e) favor the production of A_3^+ -ions. At higher discharge or RF power the A_3^+ -ions are easily broken to A^+ and A_2^+. Low pressure favors the production of these lighter ions as well.

By placing a transverse magnetic field inside the plasma chamber, in front of the ion extraction aperture, the atomic ion component can be further increased in the extracted beam[16]. The magnetic filter lowers the temperature of the electrons behind the field, so they can break up the molecular ions, but cannot ionize neutral gas. For hydrogen, for example, the dissociation energy of the H_2 molecule is 4.52 eV, while the ionization energy is 15.4 eV.

4.2 Volume negative ion production

When we are studying negative ions, the term electron affinity has a fundamental role in it. It is defined as follows

$$E_a = E_n - E_- \tag{43}$$

In equation (43) E_a is the electron affinity and also the energy needed to detach the extra electron from the negative ion, E_n and E_- are the total energies of the neutral atom and the negative ion, respectively. In order to form a stabile negative ion the electron affinity of the element has to be positive. In figure 12 the electron affinities of most elements are plotted[18].

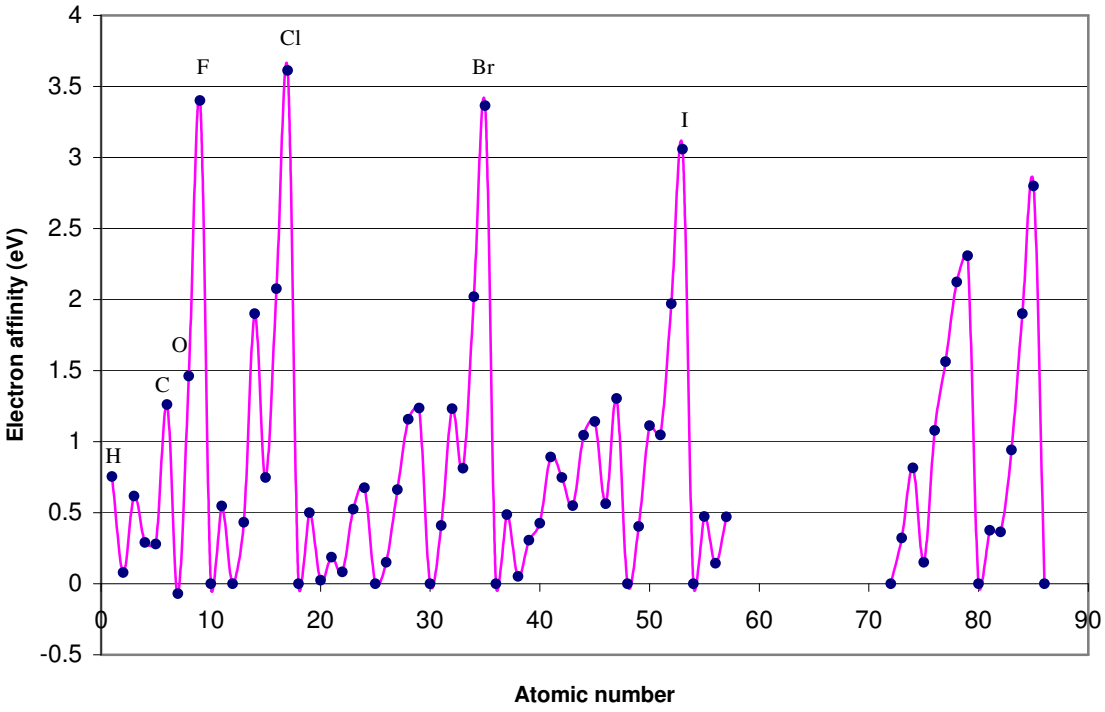

***Figure 12**. Electron affinities for most elements.*

Neutral atom can be described as an inert nucleus with point like positive charge surrounded by a negatively charged cloud of electrons. Let's place an extra electron at a distance R from the nucleus. α is the fraction of the electron cloud's charge within radius R of the nucleus and is smaller than unity. In this case the total potential energy of the electron at radius R is[17]

$$U_p = -\frac{(1-\beta)(1-\alpha)Q^2e^2}{R} \tag{44}$$

where β is a constant smaller than unity. Equation (44) indicates that the net force acting on the added electron is attractive, but it falls off much faster than regular Coulomb interaction because the term $(1-\beta)(1-\alpha) \to 0$ as $r \to \infty$, where r is the distance from the nucleus. The real picture is of course not this simple, as one has to describe the electron orbitals according to quantum mechanics, which limits the way a negative ion can form.

There are many different ways of creating negative ions. Most common are radiative attachment, dissociative attachment and capture of bound electrons[17].

In radiative attachment a neutral atom captures a free electron and because the resulting total energy of the negative ion is lower than that of the neutral atom, the extra energy will be emitted in the form of a photon. The cross sections for radiative processes are low, so they do not have great significance in ion source applications and the finer details are therefore overlooked here.

The most important negative ion production channels in a volume of the plasma are through collisional processes, where an electron impacts with a neutral molecule and dissociates it. Two of these collisional reactions are studied below.

4.2.1 Dissociative attachment

The most important volume negative ion production channel is the so called *dissociative attachment,* which is a two part process[17,19].

$$\begin{aligned} &(a) \quad XY + e_f \rightarrow XY(v'') + e \\ &(b) \quad XY(v'') + e_t \rightarrow XY^- \rightarrow X + Y^- \end{aligned} \tag{45}$$

In the first part of the process a fast electron e_f ($T_e \geq 10\,eV$) collides with a neutral molecule and excites it in to a high vibrational state. This vibrating molecule then captures a thermal electron e_t ($T_e \leq 1\,eV$) and forms an intermediate molecular negative ion. Usually the excess energy of the resulting molecular ion XY^- is disposed by the breakup of the molecule into neutral atom X and a negative ion Y^-, although some molecular states can also be stable.

In figure 13 the cross-sections for hydrogen and oxygen negative ion production as a function of the bombarding electron energy are presented[17].

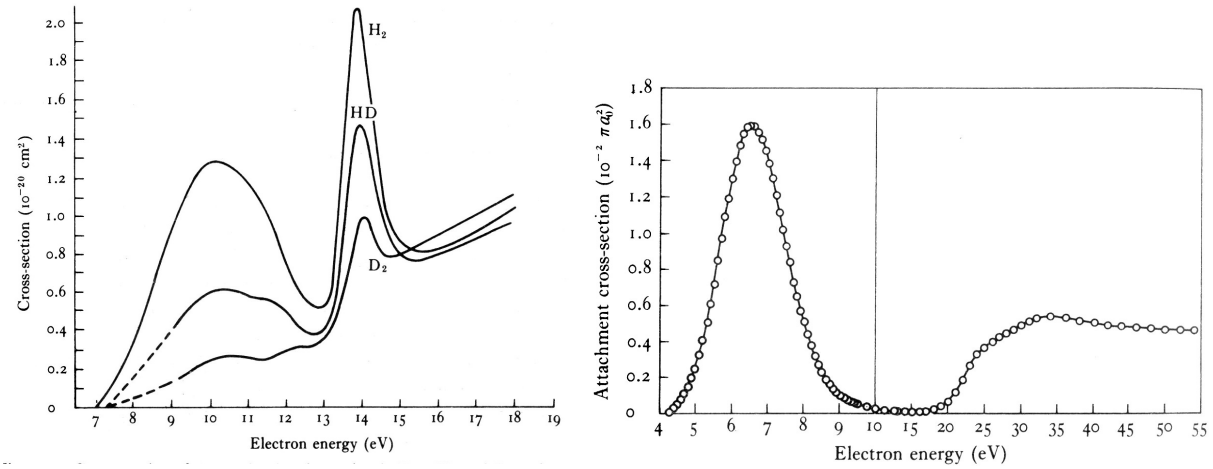

***Figure 13**. Cross sections for negative ion formation through dissociative processes for (a) H_2, HD and D_2 and (b) O_2.*

From the cross-section curves of figure 13, we can see that the maximum negative ion production cross sections for H_2 and O_2 are about $2 \cdot 10^{-20} cm^2$ and $5 \cdot 10^{-18} cm^2$, respectively. The sharp maximum peaks in the cross section curves, at 14 eV for H_2 and 6.5 eV for O_2, correspond to excitation of the gas molecule and negative ion formation through dissociative attachment.

If we compare these values to the positive ion formation cross sections of figure 11, we see that the negative hydrogen ionization cross section is almost four orders of magnitude smaller than the positive ionization cross section. For oxygen the difference is much smaller, only two orders of magnitude. The difference in the relative negative ionization probabilities for hydrogen and oxygen can be explained with the different electron affinities of these elements, for hydrogen E_a = 0.75 eV and for oxygen E_a = 1.46 eV.

By examining reaction (45) we can see that a volume production negative ion source has to have two separate regions to maximize the negative ion yield through dissociative attachment. The hot plasma region has to contain enough fast electrons to excite gas molecules into vibrational states. The cold plasma volume has to have as few fast electrons as possible and a large amount of cold electrons. This is usually achieved by placing a dipole magnetic field in the plasma volume so that it separates the plasma chamber into a hot discharge region, where the main ionization of gas occurs, and an extraction region, where most of the negative ions are created.

4.2.2 Polar dissociation

Another collisional process forming negative ions is so called *polar dissociation*. This process goes as follows:

$$XY + e \rightarrow X^+ + Y^- + e \tag{46}$$

In polar dissociation the electron is not attached to the reacting molecule, like in dissociative attachment, but is just colliding with the molecule giving energy to it. If the excitation energy of the molecule is large enough, the molecule may break into a positive and a negative ion.

The energy dependence of the cross section of process (46) is different from the electron capture reaction of dissociative attachment. It is similar to the cross section curve of inelastic electron collision with neutral atom or molecule, see figure 11. The cross section starts from zero at a certain threshold energy and grows to a maximum value at 2 – 4 times the threshold energy. This behavior can be clearly seen in figure 12 (b). The polar dissociation cross section for O_2 starts from zero at 17 eV electron energy and increases to maximum value at around 35 eV electron energy.

4.3 Surface production of negative ions

Surface production of negative ions happens when a positive ion or a neutral particle interacts with a material (metal) surface with a low work function ϕ and captures an electron from the Fermi level of the metal. The work function of a material is the amount of energy needed to remove an electron from the surface. The work functions of some elements are presented in figure 13 [20].

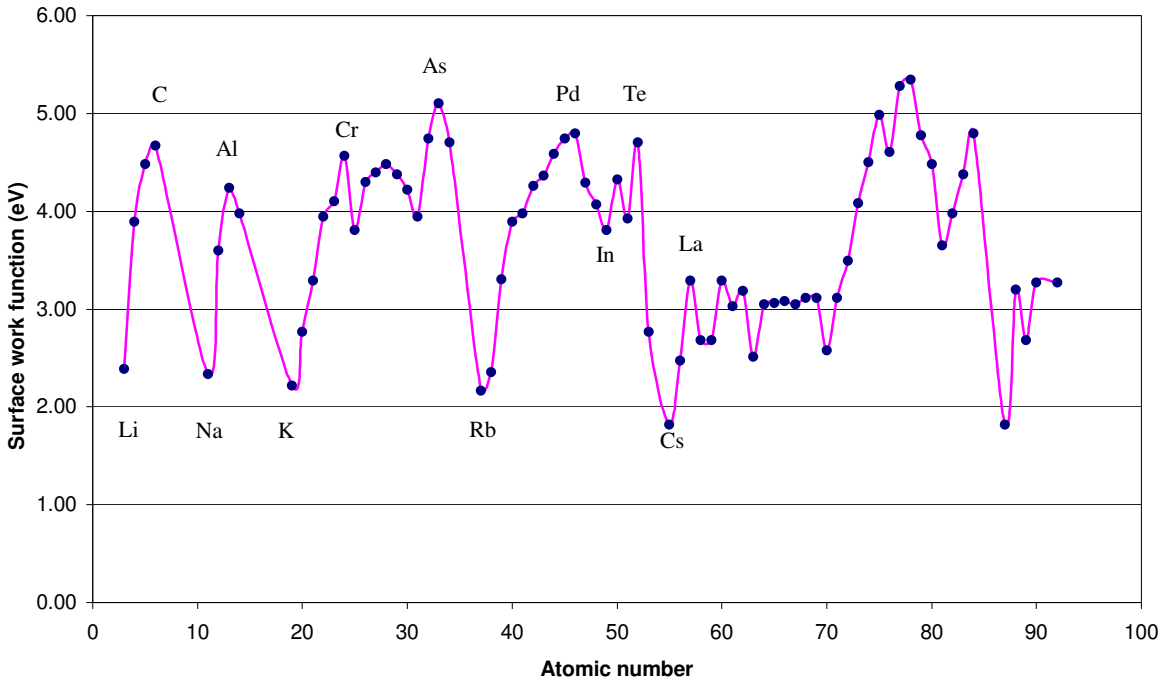

***Figure 13**. Surface work functions for most metallic elements*

In order to form negative ions effectively the electron affinity of the element being ionized has to be high. There are two different types of surface production reactions, which will be described here.

4.3.1 Reflection surface ionization

Usually the surface where the negative ionization happens is biased to a negative potential with respect to the plasma chamber walls and thus plasma itself. A plasma sheath is formed in front of the surface, usually called *converter surface*, and positive ions from the plasma are accelerated towards the converter through the sheath. Some of the ions are reflected back from the low work function surface and at the same time turned into singly charged negative ions. After passing through the sheath these backscattered negative ions have a maximum energy

$$E = 2eU_c \tag{47}$$

where U_c is the converter voltage with respect to the plasma.

The neutral particles of the plasma will also hit the converter surface and some of them are adsorbed into it. When the positive ion flux hits the surface some of the adsorbed atoms are ejected and are turned into negative ions with energy

$$E = eU_c \tag{48}$$

If the plasma has several different kinds of ions in it the negative ions ejected from the converter surface can have as many energies as there are different ion species. Let's take a hydrogen plasma as an example, which has H^+, H_2^+ and H_3^+-ions formed in the plasma volume. When these ions are accelerated through the sheath and hit the converter surface, they will break up and reflect from the surface and some of them are turned into H^- -ions. If the voltage across the plasma sheath is U_c, the emitted H^--ions will have energies of $2eU_c$, $1.5eU_c$ and $1.33eU_c$ corresponding to the incident H^+, H_2^+ and H_3^+-ions. Figure 14 shows a measured surface produced negative hydrogen ion spectrum[21].

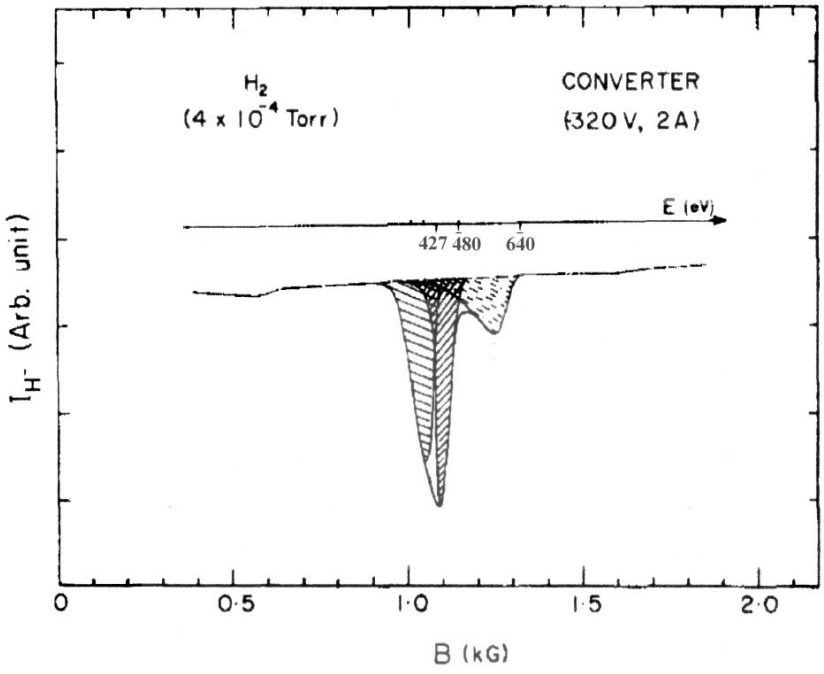

***Figure 14**. H^- peaks produced by reflection process.*

In the spectrum of figure 14, the converter voltage was 320 V, and there are 3 H^- peaks corresponding to maximum energies of 640 eV, 480 eV and 427 eV. These are the three

peaks arising from the three above mentioned positive hydrogen ion components present in the plasma.

4.3.2 Sputtering surface ionization

The second type of negative ion production in a converter surface is through *sputtering* mechanism. In sputtering ion source the converter is made out of the material that is being ionized. A heavy gas, usually argon or xenon, is used to create the background plasma. The converter is biased to 0.5 – 1 kV negative potential with respect to the ion source walls and the plasma. The positive ions from the plasma are accelerated through the plasma sheath and strike the converter. This results in ejection, or so called *sputtering*, of particles from the surface. If the work function of the converter material is low, some of these sputtered atoms are converted into negative ions in the surface and are accelerated through the sheath. Figure 15 shows a schematic diagram of the sputtering ionization process.

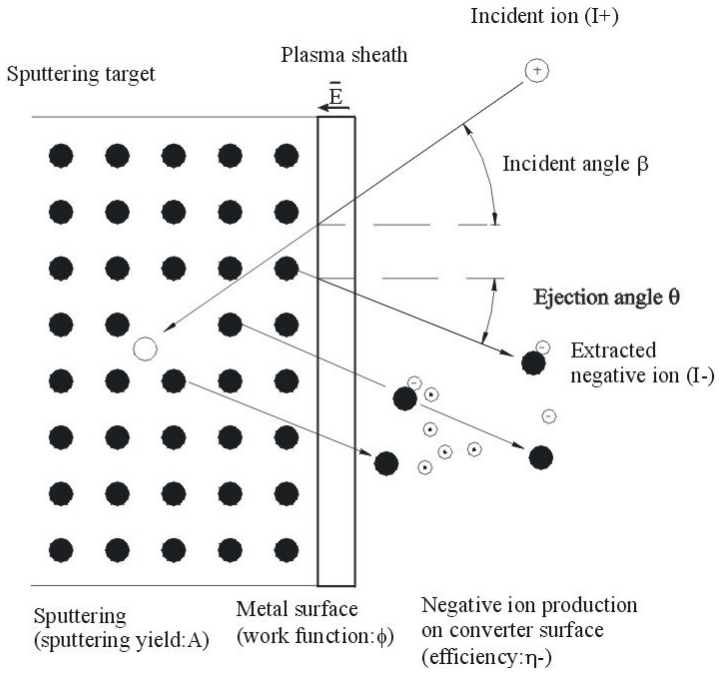

***Figure 15**. Sputtering ionization by incident heavy ions.*

The sputtering yield A of the converter material depends on the bombarding ion mass m_i, energy E_i and angle of incidence β. The converter voltage with respect to the plasma creates an electric field that is normal to the converter surface and accelerates the positive ions from the plasma with practically zero angle of incidence.

The total sputtering yield from material by ion bombardment (ion energy < 1 keV) can be estimated with the following expression[22]

$$A(E) = \left(\frac{3}{4\pi^2}\right) \cdot \alpha \frac{4M_1M_2}{(M_1 + M_2)^2} \frac{E}{U_0} \tag{49}$$

In equation (49), M_2 and U_0 are the mass and sublimation energy of the target material, M_1 and E are the mass and the energy of the bombarding ion and α is a constant depending on the value of the mass ratio M_2/M_1. Figure 16 shows a plot of α as a function of M_2/M_1 [23].

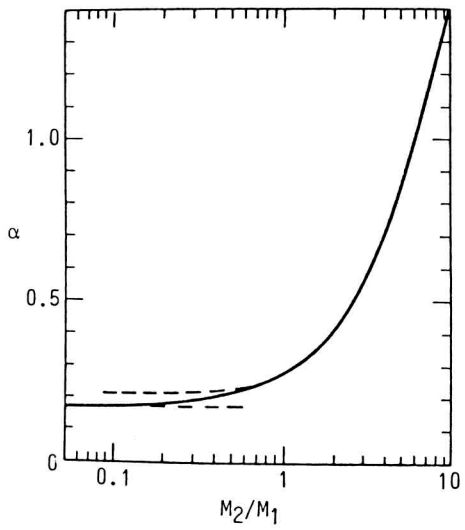

Figure 16*. Sputtering rate constant α as a function of the ratio of target atom and incident ion masses, M_2/M_1.*

The sputtered particles are emitted with an angular distribution that is strongly dependent on the incident ion energy. Figure 17 shows angular distribution of ejected *Mo* atoms as a function of normally incident Hg^+ ion energy [24]. At low energies most of the sputtered atoms are emitted at angles greater than 30 degrees. As the incident ion energy increases the angular distribution of sputter products gets more evenly spread towards the low ejection angles.

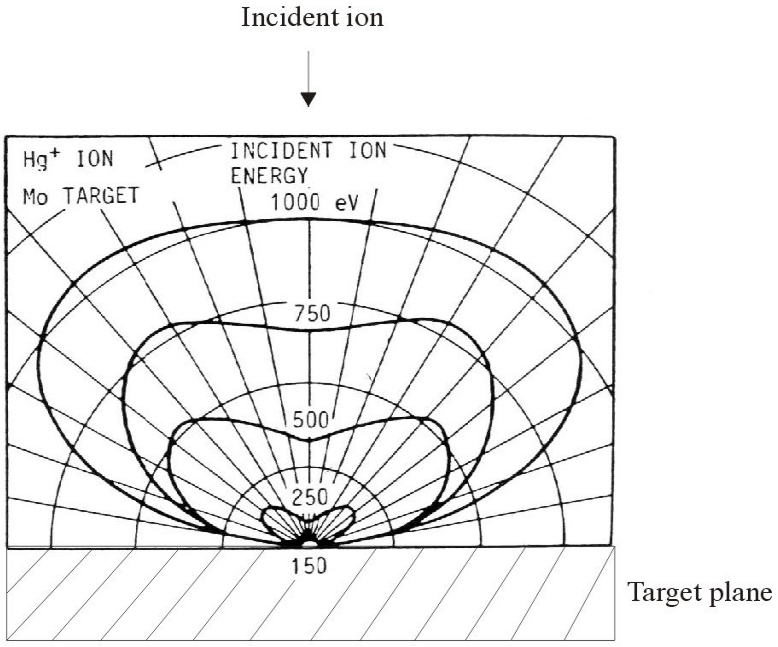

***Figure 17**. Angular distribution of sputtered Mo atoms at different normally incident Hg^+ ion energies.*

Equation (49) is approaching the sputtering as an elastic, hard sphere collision between the incident ion and the target atoms, which results in sputtering of single atoms from the target surface. The real sputtering phenomenon is more complex and can include in many cases the emission of clusters[25,26] . In experimental and theoretical considerations of metallic sputtering targets, the clusters of two and three atoms have been observed to have combined sputtering yields as high as 25 % of the single atom sputtering yield. The clusters with more than three atoms were dissociating very quickly to di- and tri-atomic clusters.

When the sputtered particles leave the target surface, they have probability P to form a negative ion by electron capture. The probability P can be expressed in form[27]

$$P(v) = (2/\pi)\exp(-(\phi - E_a)/(2av\cdot\cos(\theta)/\pi + 0.073 + 2\cdot 10^{-3}\cdot M) \qquad (50)$$

where ϕ is the target surface work function [eV], E_a is the electron affinity of the negative ion [eV], a is the decay factor for hydrogen, i.e., $2\cdot 10^{-5}$ [eV/m] and v, θ and M are the velocity, angle and mass number of the sputtered particle, respectively. The term $v\cdot\cos(\theta)$ is the velocity component normal to the target surface.

The total negative ionization efficiency η^- can be calculated by integrating the product of *P(v)* and *f(v)*, where *f(v)* is the velocity distribution function of sputtered particles:

$$\eta^- = \int_0^\infty P(v) f(v) dv \tag{51}$$

4.3.3 Effect of electropositive adsorbate on metal surface work function

To maximize the negative ionization efficiency the sputtering target work function has to be minimized. It has been demonstrated that by covering the sputtering target with electropositive materials from groups IA and IIA of the periodic table, especially cesium, which has the lowest work function of all elements (1.81 eV), the target surface work function decreases and the negative ion yields increase dramatically[28]. In general the work function of a cesiated surface is even lower than that of bulk cesium. The work function of the surface depends on the cesium coverage, which is illustrated in figure 18 [29].

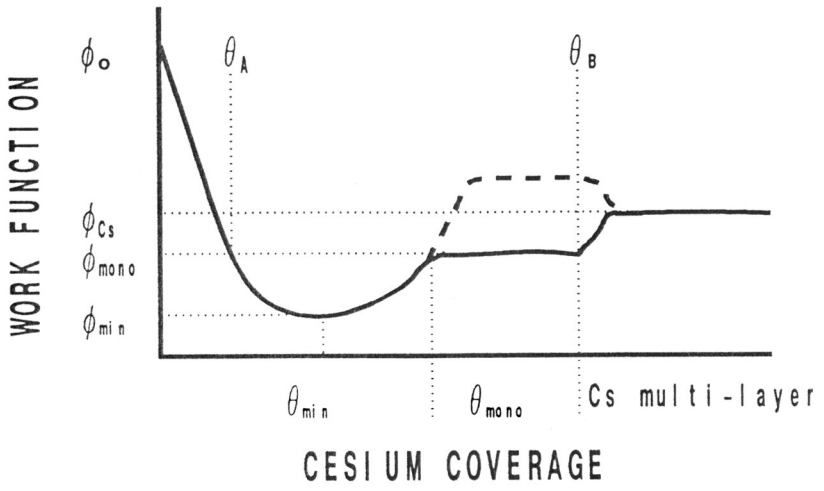

Figure 18*. General behavior of the surface work function with changing cesium coverage.*

In figure 18, the work function of the uncesiated surface is ϕ_0. The work function decreases with increasing cesium coverage until it reaches a minimum ϕ_{min} at around 60 % coverage of the surface. The work function then increases and reaches a stable value

ϕ_{mono} when a monolayer of cesium has been deposited. If multiple layers of cesium are formed, the work function is that of bulk cesium, ϕ_{Cs}.

The minimum work function of a metal surface covered with an electropositive adsorbate is given approximately by the semiempirical equation[30]

$$\phi_{\min} = 0.62(V_i + E_a) - 0.24\phi_0 \tag{52}$$

where V_i and E_a are the first ionization potential and electron affinity of the electropositive adsorbate material and ϕ_0 is the intrinsic work function of the metal surface. The value of $(V_i + E_a)$ is the lowest of all elements for cesium, 4.35 eV.

Let's take copper as an example. From figure 13 we can see that the uncesiated work function of a copper surface is 4.4 eV. From equation (52) we can calculate that an optimal cesiation would lower the work function to about 1.6 eV. From equation (50) we can see that the negative ionization probability for a copper atom at a certain velocity would increase by a factor of 16 in the case of optimal cesiation. This is a considerable increase if one is to maximize the negative ion yields.

5. Ion extraction and beam optics

Ion beam extraction is as important as the ion generation itself in ion sources. The basic principles governing the ion beam formation arise from three main concepts: the density and mobility of charged particles inside the plasma chamber, the strength of the electric field between the ion source and the extracting electrode and the space charge of the extracted ion beam. In this chapter the basics of the ion extraction and ion beam optics are presented.

5.1 Child- Langmuir law and perveance

The space charge limited current emission of charged particles is given by the law of C*hild- Langmuir*[1] :

$$j = 1.72\sqrt{\frac{Q}{M}}\frac{U^{3/2}}{d^2} \qquad [mA/cm^2] \tag{53}$$

where j is the current density of the ion beam, Q and M are the charge state and the mass number of the ion and U [kV] and d [cm] are the applied voltage and gap between the ion source body and the extracting electrode, respectively.

The assumption made in deriving equation (53) is that the ion source produces more charged particles that can be extracted due to their space charge. The other assumption is that the emitting surface is planar. The first condition is easily met in modern ion sources, but the emitting surface is rarely a plane. This means that the current density values given by equation (53) are upper limits for actual extractable current densities.

Another widely used definition when ion extraction and beams are considered is *perveance*. It is defined as follows:

$$P = \frac{I}{U^{3/2}}\sqrt{\frac{M}{Q}} \tag{54}$$

In many cases the ions can have charge state that is larger than one. In this case it is useful to define the *normalized current*:

$$I_n = I\sqrt{\frac{M}{Q}} \tag{55}$$

Normalized current I_n is also called *proton equivalent current*.

5.2 Beam emittance and brightness

The most important parameter that is used to describe an ion beam next to the ion current is the *beam emittance*. It is defined as the volume that the ion beam particles occupy in the six dimensional phase space (x, p_x, y, p_y, z, p_z), where x, y and z are the space coordinates of the beam particles and p_x, p_y and p_z are the corresponding linear momenta of the particles along the space coordinate axis.

Usually the longitudinal emittance projection along the beam axis is of no interest and only the two transverse emittance planes (x, p_x) and (y, p_y) are considered. In figure 19 the velocity vector definitions are shown.

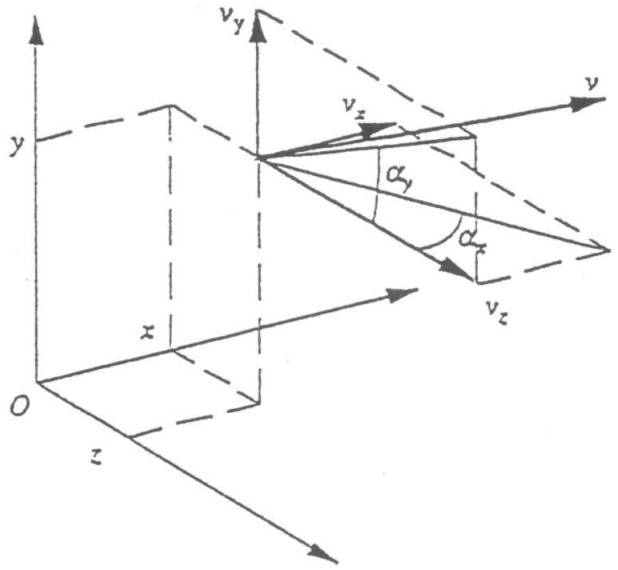

Figure 19. *Velocity vertors of an ion.*

In figure 19 α_x and α_y are the divergence angles of the x and y velocity components. Beam direction is chosen to be along z axis.

Let's consider the linear momentum of the ion along x axis. It can be written as

$$mv_x = m\frac{dx}{dt} = m\frac{dx}{dz}\frac{dz}{dt} = mx'v_z \propto x' \tag{56}$$

The gradient x' can be written in terms of the divergence angle α_x:

$$x' = \frac{dx}{dz} = \frac{v_x}{v_z} = \tan(\alpha_x) \tag{57}$$

Usually v_x is much smaller than v_z and $x' \approx \alpha_x$. In this case the beam emittance is defined as the area that the particles occupy in the *(x,x')* and *(y,y')* planes. The emittance pattern is usually an ellipse with half axis A and B. The emittance value is then given by the area of the ellipse

$$\varepsilon_{x,y} = \pi AB \qquad [mm\ mrad] \tag{58}$$

The emittance ellipse orientation indicates if the beam is divergent, convergent, parallel or focused. In figure 20 the emittance ellipses are shown for each of these cases.

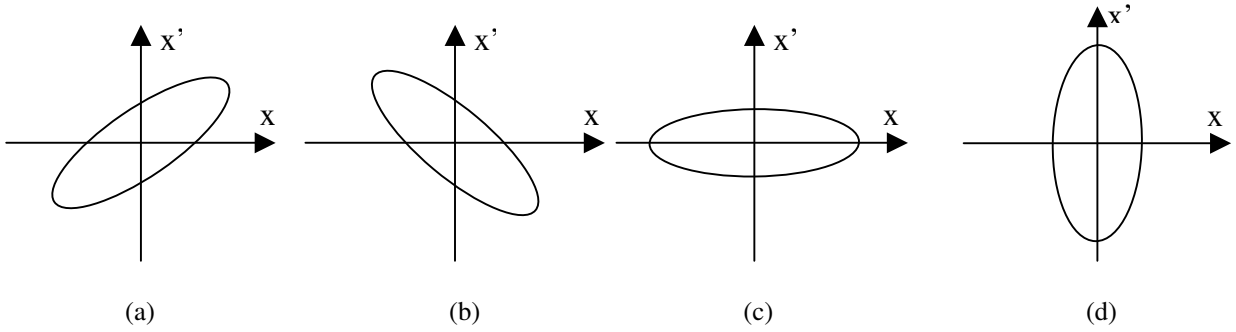

Figure 20. *The emittance ellipse orientation for (a) diverging, (b) converging, (c) parallel and (d) focused ion beam.*

In defining the emittance as the area the beam occupies in *(x,x')* and *(y,y')* plane we have neglected the effect of ion beam velocity along the beam axis, v_z. If v_z increases, beam divergence and thus the emittance will decrease. This effect is eliminated by using *normalized* emittance ε_n, which is given by:

$$\varepsilon_n = \beta\gamma\varepsilon \tag{59}$$

where $\beta = \frac{v_z}{c}$ is the ratio of the beam axial velocity and the speed of light and

$$\gamma = \frac{1}{\sqrt{1-\beta^2}}\,.$$

Widely used emittance definition is the *root mean square*, or *RMS*, emittance. It is given by:

$$\varepsilon_{rms} = \sqrt{\overline{x^2}\,\overline{x'^2} - \overline{(xx')}^2} \tag{60}$$

Equation (60) is often multiplied by 4 when measured emittance values are reported, as the $4\varepsilon_{rms}$ gives an emittance value that corresponds well to the area of the ellipse that is fitted to the emittance pattern.

Some practical formulas have been derived to estimate the emittance of a beam with Maxwellian energy distribution. For ion beam extracted from a circular aperture the normalized RMS emittance is given by equation[31]:

$$\varepsilon_{n,RMS} = 0.016325 \cdot R\sqrt{\frac{kT}{M}} \qquad [\pi\, mm\ mrad] \tag{61}$$

In equation (61) R is the extraction aperture radius in mm, kT is the ion temperature in eV and M is the mass number of the extracted ion.

The ion beam current and emittance are combined in definition of the beam *brightness B*:

$$B = \frac{I}{\varepsilon_x \varepsilon_y} \tag{62}$$

where I is the ion current and ε_x and ε_y are the transverse emittance values in *(x,x')* and *(y,y')* planes.

5.3 Ion beam space charge

After being extracted from the ion source, the space charge of the ion beam can blow out the beam considerably during transport. The strength of the space charge force F and the increase of the beam radius Δr are proportional to[1] :

$$F \propto \frac{I}{\sqrt{E}},\ \Delta r \propto \frac{I \cdot z^2}{E^{3/2}} \tag{63}$$

where I and E are the ion beam current and energy and z is transportation distance of the beam. It's clear from these relations that in order to reduce the beam blow up it is important to minimize the distance the beam has to travel and use as high energy as possible. In many cases this is not possible, however, and the space charge effect has to be minimized by other means.

This is usually accomplished by letting the ion beam pass through a background gas in the beam transport line. The beam ionizes the gas and creates a background plasma. In case of positive ion beam, the slow electrons from the background plasma are sucked into the beam potential well and neutralize the space charge of the beam. In case of negative ions the slow electrons are replaced by the positive ions created in the background

plasma. More than 99 % of the beam space charge potential can be neutralized by the background gas if the pressure is high enough, 10^{-4} – 10^{-3} Torr. In the case of high background gas pressure, the beam space charge is neutralized effectively. However, the ion beam current is reduced due to stripping and recombination losses. In figure 21 an example of the gas neutralization of the ion beam space charge potential is presented[32].

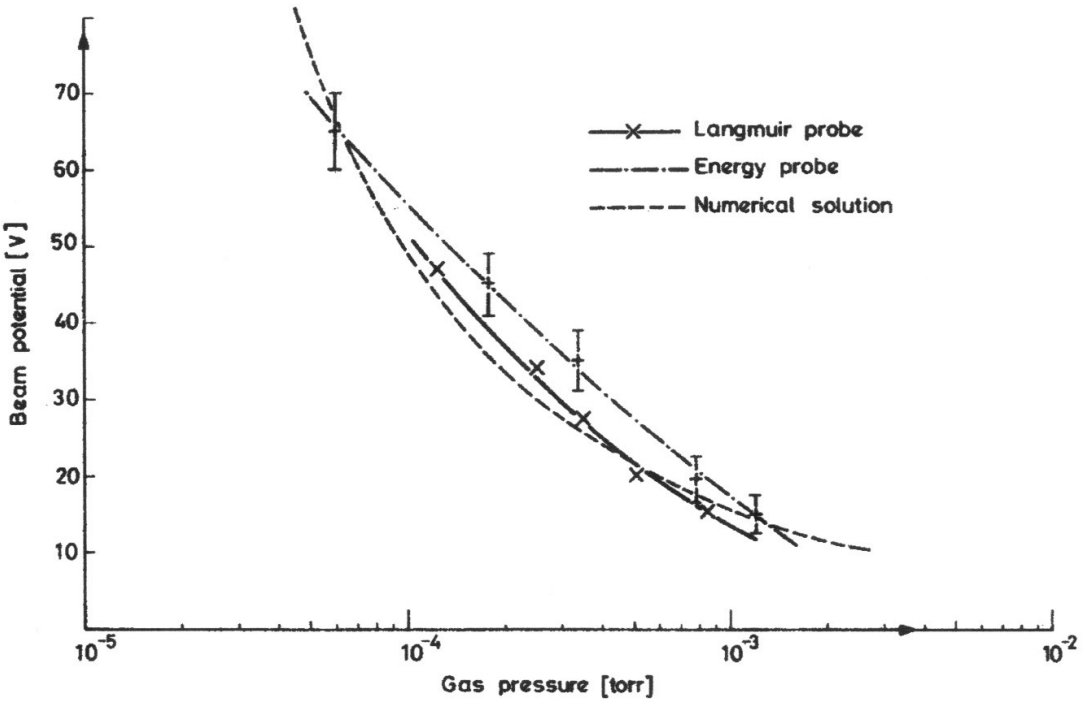

Figure 21. *Radial potential of a 20 keV, 20 mA He^+ beam in He gas as a function of the gas pressure. As the gas pressure increases from 10^{-4} torr to 10^{-3} torr, the ion beam radial potential decreases from 70 V to 10 V, which reduces the electric field blowing out the beam by a factor of seven.*

The space charge neutralization does not work if there are strong electric fields present in the neutralization area, as the slow background electrons and to a lesser degree the slow ions are swept away by the field. This prevents the space charge neutralization of ion beams in the area of electrostatic ion extraction.

Transverse magnetic field, as in a bending magnet, blocks the flow of neutralizing electrons and ions into the path of the ion beam and thus prevents effective space charge neutralization. In a solenoid magnetic field, on the other hand, the slow electrons and ions are focused towards the center axis and this enables space charge neutralization of the ion beam.

5.4 Volume extraction of ions

The volume extraction of ions happens when an extraction aperture is opened into one of the plasma chamber walls and an extraction voltage is applied between the plasma chamber and an extraction electrode. The electric field formed between the electrodes penetrates into the extraction aperture and accelerates ions from the source volume towards the extraction electrode.

5.4.1 Plasma meniscus

The boundary layer formed between the plasma and the extracted ion beam is called *plasma meniscus*. This is a few Debye- lengths wide region over which the extracting electric field is attenuated to zero. The charged particles that diffuse into the plasma meniscus start feeling the electric field and are extracted. If a round extraction aperture is used, the meniscus will acquire approximately circular form.

The position and degree of curvature of the meniscus depend on two opposing "forces" exerting pressure on it from opposing sides, the charged particles of plasma on the ion source side and the extracting electric field on the extraction side. The relative strength of these two determines where the meniscus is formed. In figure 22, three different plasma density values are used to demonstrate this effect by using IGUN ion optics simulation code[33].

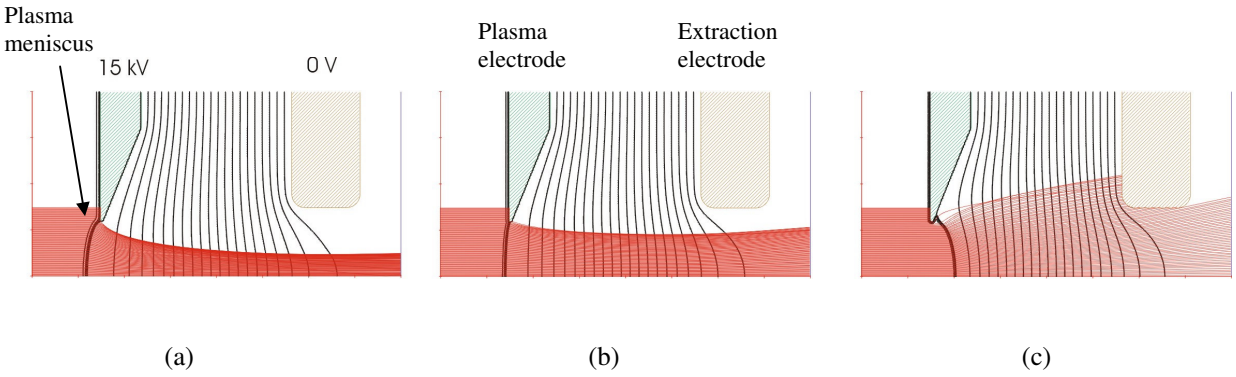

***Figure 22**. Plasma surface formation at 15 kV extraction voltage and hydrogen plasma density of (a), 6E10 1/cm^3, (b)1E11 1/cm^3 and (c) 3E11 1/cm^3.*

In figure 22 (a) the plasma is under dense and the meniscus is penetrating deep inside the ion source. This creates a concave meniscus, which is focusing the extracted ions strongly towards the center axis of the beam, which will lead later on to a strong beam blow up due to the beam space charge. Figure 22 (b) shows an intermediate density plasma, which creates a reasonably flat meniscus and is better matched extraction

condition for the ion beam. In the case of figure 22 (c) the plasma is over dense relative to the extracting electric field and the meniscus bows out and many of the ions are dumped to the extracting electrode.

The effect of space charge is evident in figure 22 (a) as the ion beam would over focus and the beam trajectories would cross the center axis if the space charge of the ions wouldn't exert a retarding force. This means that if a parallel beam is needed at some point after the extraction a flat emitting surface is not favorable but a concave one that compensates the space charge blow up of the beam by starting it from a focusing plasma meniscus.

The extractable current density depends on the ion density and temperature in the ion source and the strength of the extraction electric field. To achieve a desired extraction condition for the beam the plasma density, extraction voltage and the extraction gap can be adjusted.

The first centimeters of the ion extraction determine largely the behavior of the beam through rest of the transport line. The emittance and beam brightness are properties that strongly depend on the extraction geometry and ion temperature in the plasma.

5.4.2 Negative ion extraction from volume plasma

Negative ions can be extracted from the plasma volume similarly to the positive ions by opening an aperture to the plasma chamber wall and applying a voltage between the ion source and an extraction electrode. The extractable current density, which is a combination of the negative ion and electron current densities, has a maximum value given by the Child- Langmuir law, equation (53). Plasma meniscus formation is somewhat different to the case of positive ions. Figure 23 shows a schematic of the potential distribution across the plasma meniscus for positive and negative ion extraction.

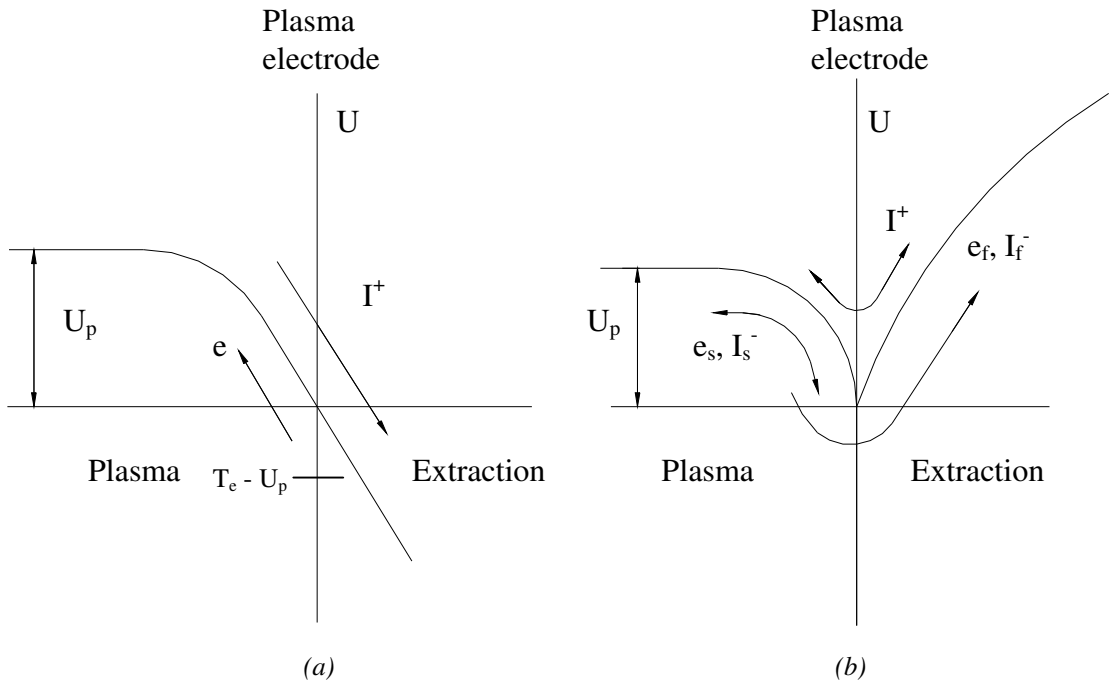

***Figure 23**. Potential distribution across the plasma meniscus region in (a) positive and (b) negative ion extraction. U_p is the plasma potential.*

Figure 23 (a) shows how in positive ion extraction all the ions that drift into the meniscus will fall down the potential well. Electrons will only be able to climb to a potential T_e - U_p to the extraction side after which they will be reflected back to the plasma. Electrons act as the shielding particles for external electric field in the plasma-beam boundary.

In the case of negative ion extraction, figure 23 (b), low temperature electrons and negative ions, e_s and I_s^-, with kinetic energy smaller than eU_p will be trapped in the plasma. Electrons and negative ions with higher kinetic energy than eU_p will be extracted from the source. Positive ions will climb the potential well up to a point $U_p + T_i$, where T_i is the ion thermal kinetic energy. Positive ions are taking the place of electrons in negative ion extraction as the shielding particles of external electric field in the plasma meniscus region.

From figures 23 (a) and (b) it can be seen that the charge distribution is different in positive and negative ion extraction and thus the plasma meniscus is also located in a different place. In general it is observed that the meniscus is extending further into the extraction side in the case of negative ions[34]. It must be stated that figure 23 is only an approximate presentation. The sharp potential dip occurs only if the extraction aperture is

very small or has a fine mesh over it, which forces the potential at the extraction aperture to a certain value. If the extraction aperture is large, the potential distribution can be without a minimum in the negative ion case, figure 23 (b).

5.4.3 Removal of electrons from negative ion beam

The biggest difference between positive and negative ion extraction is that the electrons from the plasma are also extracted with the negative ions. Because the mobility of electrons is much higher than the mobility of ions, the extracted electron currents are much higher than the ion currents. From equation (53) we can see that if the negative ion and electron densities would be same in the vicinity of the plasma meniscus, the extracted electron current density would be:

$$j_e = \sqrt{\frac{m_i}{m_e}} \cdot j_i = 43\sqrt{M_i} \cdot j_i \tag{64}$$

where j_e and j_i are the electron and ion current densities, m_e and m_i are the electron and ion masses and M_i is the mass number of the ion.

Quite often the electron density is much higher than the negative ion density in the plasma, which increases the relative extracted electron current even more. The electron current can have a considerable power if it is accelerated to a high voltage, which means special care has to be taken to handle the heat load. The extracted electron current also drains the high voltage power supply capacity. These reasons mean that either the electron flux from the plasma has to be minimized by lowering the electron density and/or temperature in the plasma, or the electrons have to be removed from the extracted beam as soon after the extraction and at as low energy as possible.

Typically the electrons are removed from the beam by placing a transverse magnetic field in the extraction region, which will deflect the electrons out of the beam. Figure 24 shows a schematic of two typical magnetic field configurations.

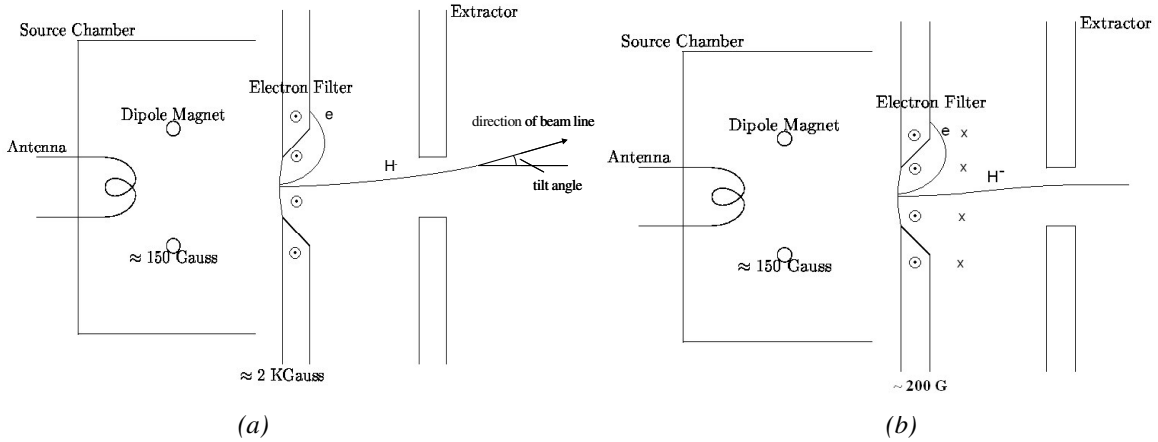

Figure 24*. Electron removal from the extracted ion beam by transverse magnetic field in (a) SNS H⁻ ion source[35] and (b) Jyvaskyla H⁻ ion source[36].*

In figure 24 (a) the electrons are reflected back to the plasma electrode by a relatively strong magnetic field ranging from few hundred gauss to two kilogauss. The ion beam is also deflected, which is taken into account by tilting the ion source with respect to the extraction column.

Figure 24 (b) shows an electron filter set up consisting of a dipole anti-dipole set up. The electrons are removed by the first dipole field, while the second dipole corrects the ion beam trajectories and the beam is displaced laterally from the original axis.

In some applications multiple apertures are used to extract the ions from the ion source. In this case it is possible to filter the electrons out of the ion beam by using a honeycomb structure, where the extraction electrode is a high aspect ratio channel with a weak transverse magnetic field across the electrode[37]. The schematic of this extraction filter is presented in figure 25.

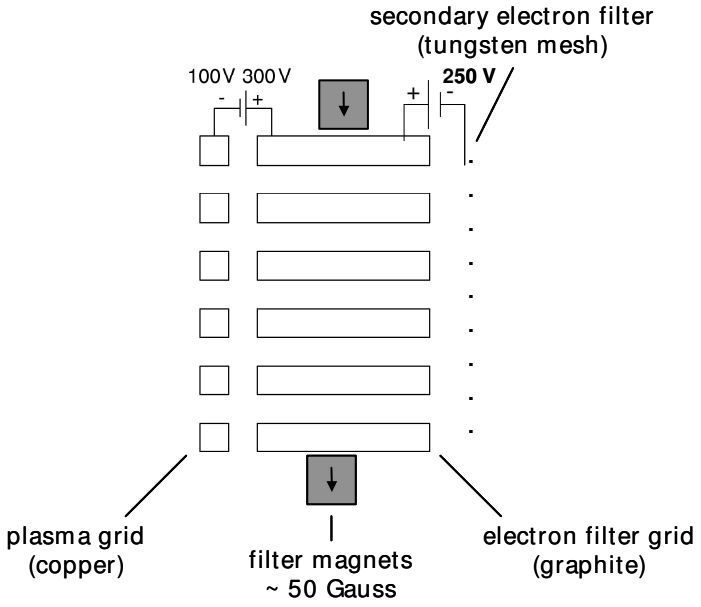

Figure 25. *Schematic of a honeycomb structured extractor/electron filter constructed at LBNL.*

5.5 Surface extraction of negative ions

In section 3.3 the surface production of negative ions was discussed in detail. There are two main negative ionization modes in a low work function surface, namely the reflection and sputtering surface ionization.

The process of *self extraction* is similar in both of these above mentioned ionization processes. The surface, where the ionization happens, is biased at a negative potential U_c with respect to the plasma, which has a potential U_p. This draws positive ions from the plasma to the surface. The negative ions that are created on the converter are accelerated from the surface because of the negative bias.

Figure 26 shows a schematic of a spherical converter surface similar to the one used in the experimental part of this thesis. The plasma sheath width is exaggerated to visualize it better. The ejected negative ions have a wide angular spread that follows from the sputtering mechanism. The ions are emitted with initial velocity $\overline{v}_i$ and have typically *10 – 30 eV* of kinetic energy and the average ejection angle ϕ is between *20 - 40 degrees* with respect to the normal of the converter surface. The ions are accelerated over the plasma sheath by the electric field $\overline{E}$, which is normal to the surface. This decreases the effective angle θ of the ions after they have reached their full energy with velocity $\overline{v}_a$ and

the ions can be directed by shaping the emitting surface. This makes it possible to focus the negative ions emitted from the converter surface to a smaller area and thus increase the current density of the beam.

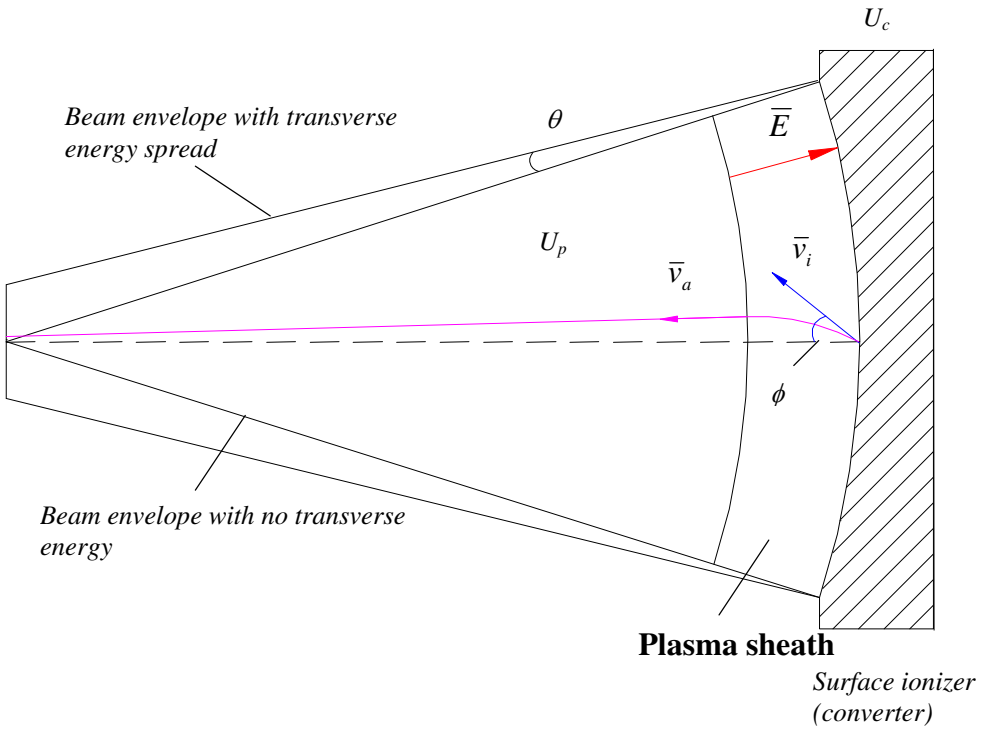

***Figure 26**. A schematic of a surface ionizer converter.*

The self extraction of the negative ions is taking place within plasma, which means that the ion beam space charge is neutralized very effectively. If the ions would not have any transverse energy, the ion beam extracted from a spherical surface would focus to a point. The sputtering mechanism introduces a spread into the ejected ion distribution, which sets a minimum size for the beam, depending on the ion mass, sputtering angle, initial velocity and the converter voltage.

The ion beam from the converter will pass through the plasma and will be extracted through an opening in the plasma chamber wall. The plasma is a very destructive environment for negative ions. This means that the ion source pressure should be as low as possible and converter voltage and thus the extracted negative ion energy should be maximized to improve the surviving fraction of the negative ion beam reaching the extraction aperture. Figure 27 shows the stripping cross section of negative hydrogen ions in hydrogen gas as a function of ion energy[38].

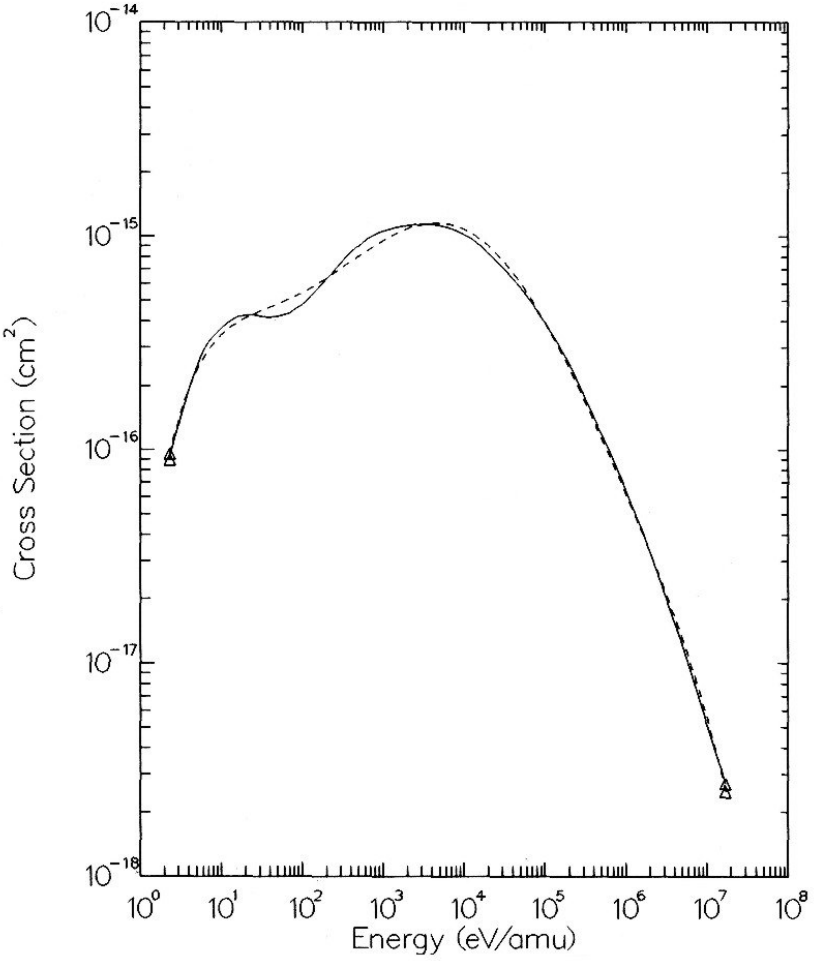

Figure 27*. Cross section for electron detachment for negative hydrogen ion in hydrogen gas as a function of H^- ion energy.*

As an example we can take equation (40) and the cross section data of figure 27 and estimate the mean free path between electron detachment collisions for negative hydrogen ion in hydrogen gas. If we have a 1 keV ion beam from the converter and 10 mTorr gas pressure in the ion source, the cross section for an electron detachment collision is 10^{-15} cm^2 and the neutral hydrogen gas density is about $3 \cdot 10^{14}$ cm^{-3}, which gives a mean free path of *3 cm*. To minimize negative ion losses the converter has to be closer than this distance from the extraction aperture or alternatively the source gas pressure has to be lower, which might be difficult because the lower gas pressure usually means lower plasma density. The plasma electrons will also increase the stripping losses of negative ions in plasma, so the above calculation gives only an upper limit for the mean free path of an ion in plasma.

According to equation (49), the sputtering yield from the converter surface is directly proportional to the energy of the incoming positive ion, which also means that higher converter voltages can produce more negative ions.

5.6 Simulation of ion extraction

The design and construction of an ion source extraction system usually starts with simulations of the extraction geometry. There are several computer codes available, which can simulate positive and negative ion extraction from plasma and can be operated by a personal computer (PC) in very reasonable computation time. This is an enormous help in the design process, as it usually shows immediately points of mismatch in the extraction geometry and helps to optimize the extraction voltage, electrode geometry and inter-electrode distances with very good accuracy.

The basic operating principles are very similar in all of them. During the first cycle the code calculates iteratively the potential distribution in a vacuum condition without any ion beam from the Poisson's equation:

$$\nabla^2 V = -\frac{\rho}{\varepsilon_0} \tag{65}$$

where V is the potential, ρ is the space charge density and ε_0 is the permittivity of vacuum.

The ions are then started from a predefined surface and the effect of the beam space charge on the potential distribution is then calculated. The plasma meniscus is calculated by the code and used as a boundary between the plasma and the ion beam. The ion trajectories are given by either the non-relativistic Lorentz force equation, (14), or by the relativistic Lagrangian:

$$L = eV - e(\overline{A} \bullet \overline{v}) - m_0 c^2 \left(1 - \frac{v^2}{c^2}\right)^{1/2} \tag{66}$$

where $\overline{A}$ is the magnetic vector potential, $\overline{v}$ and m_0 are the velocity vector and rest mass of the charged particle, V is the potential and c is the speed of light.

Three ion extraction simulation codes that were used in the work done for this thesis are presented below.

5.6.1 IGUN

IGUN is a simulation code for positive ion extraction from plasmas[33]. It is a 2D code capable of simulating axis symmetric and rectangular extraction geometries with axial magnetic fields. The program input consists of the electron and ion temperatures in the plasma, ion mass and charge state, plasma density and the plasma electrode bias with respect to the plasma. The geometry files are done either manually or by using a graphical input program.

5.6.2. PBGUNS

PBGUNS[39] is a 2D ion optics simulation code capable of simulating thermionic and field emission electron guns, positive and negative ion extraction from plasma and sputtering extraction of negative ions. Both axial and transverse magnetic fields can be included in the simulations and multiple ion charge to mass ratios can be used in same simulation. Electrons can be injected into negative ion beams to simulate the removal of electrons by transverse magnetic fields. The input files are made interactively and the simulation run can be stopped and modified without aborting the run. Ion transverse temperature can be included in the ion extraction from the plasma as a maxwellian energy spread. The plasma region is calculated using a finer mesh than the rest of the geometry, which improves the accuracy of the calculation and shortens the simulation time compared to programs that do not have this feature.

5.6.3 KOBRA3-INP

KOBRA3-INP[40] is a 3D simulation code for steady state ion extraction problems. It can simulate non-symmetric geometries, unlike the 2D codes. Realistic 3D magnetic fields can be included in the simulation. The program accepts CAD files for geometry input.

6. Negative chlorine ion experiment

Fusion is the nuclear reaction that powers the sun and other stars in the universe. In fusion, light elements are fused together into heavier elements and the mass difference between the reaction constituents and the products is released in the form of energy. This extra energy creates radiation and heat that makes life here on earth possible.

Fusion has also been proposed to be the future energy source. The fossil fuels will run out eventually, and while fission reactors are efficient power sources, their drawbacks are the highly active reaction end products and the danger of critical melt down of the reactor. In fusion, on the other hand, the reaction fuel, hydrogen isotopes deuterium (D) and tritium (T), are abundant on earth. The fusion reaction produces more energy per mass unit than fission, and the fusion end products are less radioactive and have much shorter half life than the corresponding fission products. Fusion reaction in laboratory conditions cannot end up in a meltdown as in a fission reactor.

Two main types of fusion reactors are being developed currently [41]. The oldest type of fusion energy experiment is the *magnetic confinement* fusion. In a magnetic confinement fusion reactor the mix of deuterium and tritium gases is ionized inside a toroidal chamber by lasers or microwaves. The gas will be heated to several million K temperature and will be confined by the magnetic field. The biggest problem in this type of fusion reactor is that the fusion plasma is relatively sparse and it is difficult to reach the point of ignition for the fusion reaction.

The other approach is the *inertial confinement* fusion. In this process the fusion fuel is packed into a small pellet surrounded by an ablator layer. The pellet is bombarded by an intense laser or particle beam, which heats up the outer layer of the pellet and causes it to expand. This expansion creates a “thrust” that compresses the D-T fuel in the core of the pellet to high enough temperature and pressure to initiate the fusion reaction.

In the first experimental part of this thesis the production of heavy negative ions for inertial confinement fusion driver beams was studied.

6.1 Motivation for the experiment

Traditionally space charge neutralized positive ion beams have been considered as drivers for inertial confinement fusion. Intense positive ion beams are easily obtainable[42], and the neutralization of the ion beam space charge is reasonably straightforward. The difficulties of using positive ions arise from beam-plasma instabilities, the trapping of electrons from target chamber walls and the change of the average charge state of the ions by collisions with the residual gas. This has lead to consideration of using atomic neutral particles instead of positive ion beams as drivers for inertial confinement fusion [43].

Heavy negative ions would replace their positive counterparts in this approach. The extraction and acceleration of the ions will be essentially the same as for positive ions, but after the final focusing element, before the fusion target, the negative ions would be photoneutralized and would travel the remaining distance to the target as neutral atoms. This would eliminate all space charge forces, self-magnetic fields and beam-plasma instabilities of the beam.

Best candidates for the heavy negative ions can be found in the halogen group of the periodic table of elements. From figure 12 we can see that especially bromine (mass number 81, electron affinity 3.36 eV) and iodine (mass number 127, electron affinity 3.06 eV) would be suitable for heavy ion fusion due to their large mass and high electron affinity.

These elements would have to be heated to a vapor and the ion source has to operate at elevated temperatures to prevent the condensation of the vapor on cold surfaces. For initial estimates of achievable negative ion current densities from halogens chlorine was selected for this experiment. It has similar electron affinity (3.61 eV) to bromine and iodine, and high enough mass number (35). It is commercially available in gaseous form, and thus existing volume type ion source technology could be utilized in this experiment.

The negative chlorine ion experiment was conducted in Plasma and Ion Source Technology Group in Lawrence Berkeley National Laboratory (LBNL) in Berkeley, USA. It was performed in collaboration between LBNL and Princeton Plasma Physics Laboratory (PPPL) [44].

6.2 Experimental setup

The experimental system that was used in the negative chlorine experiment is presented in figure 28. The ion source was a multicusp source driven by 13.56 MHz RF power supply and accompanying matching network. The ion extraction was a two-electrode system with a movable faraday cup for ion current measurement. An electrostatic einzel lens was used to match the extracted ion beam into a dipole magnet, which was used as a mass analyzer to separate the different ion species in the ion beam. A pepper pot emittance measurement device could be installed in the place of the faraday cup for beam emittance measurements.

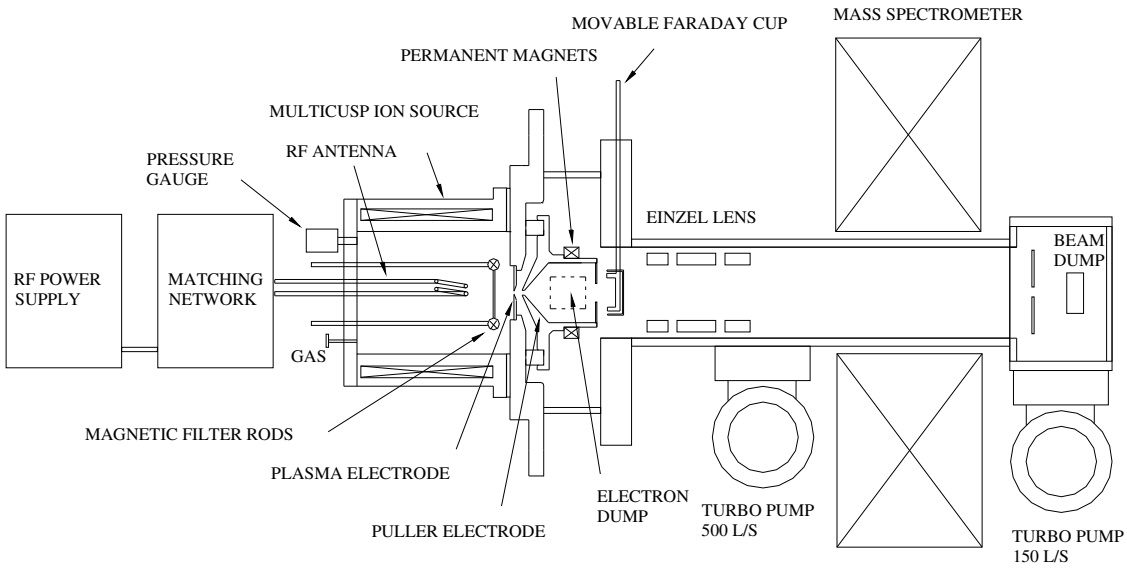

***Figure 28**. Schematic of the experimental setup.*

6.2.1 Ion source

A multicusp type volume ion source was selected for the negative chlorine experiment, as it has been proven to be able to produce high current densities of negative volume ions in the past [36,45]. It consists of 15 cm long, 10 cm diameter plasma chamber surrounded by 20 rows of water cooled SmCo-magnets. The magnetization direction of the magnets was alternating between pointing towards the center of the source and away from it. Figure 4 (b) shows a simulation of the multicusp field made with *Poisson Superfish*-simulation code [46]. This magnet geometry creates a large field-free region in the center of the ion source, and a uniform plasma density and plasma potential distribution can be achieved [7]. The uniform radial plasma density is required in order to have good ion optics.

Figure 29 shows a more detailed drawing of the multicusp source and the extraction electrodes constructed for the experiment.

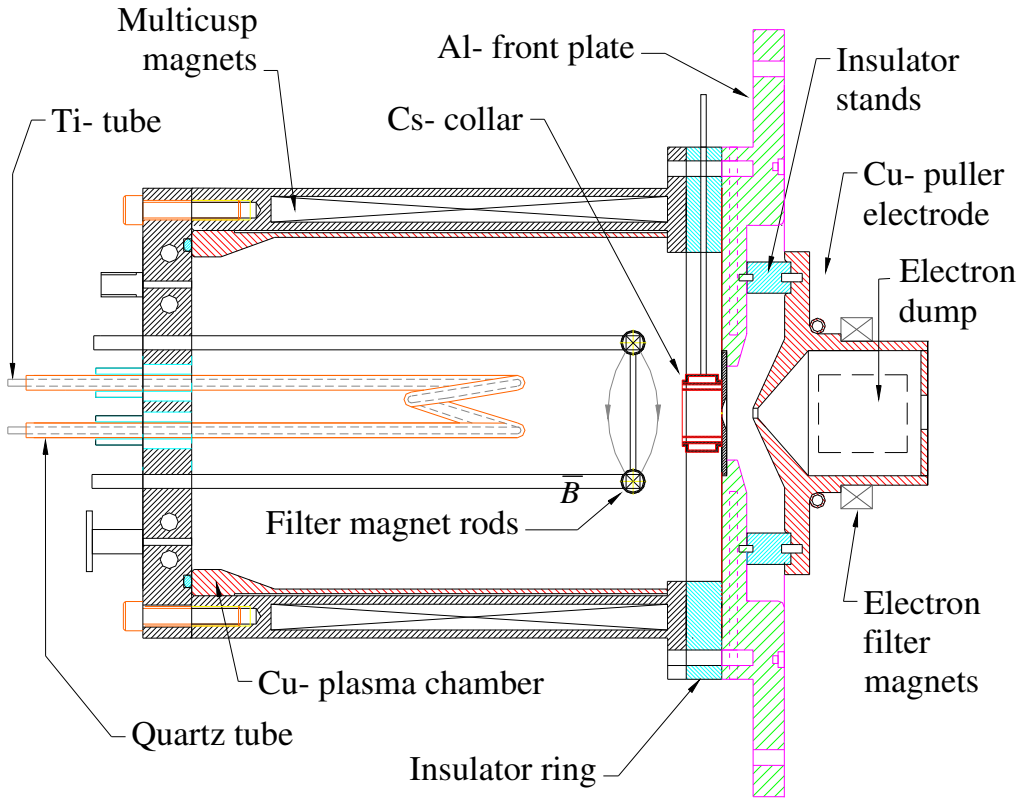

***Figure 29**. Schematic of the multicusp ion source and extraction used in the measurement.*

Titanium tube antenna running inside a quartz tube with 1.5 loops at 5 cm diameter was used in the experiment. Two antenna geometries were tested. The orientation of the first antenna loop was transverse with respect to the axis of the ion source as depicted in figure 29. This geometry was used to minimize the coupling of the RF field to the extraction region of the source. The second antenna had an axial antenna loop and was used to measure any effects that the different antenna geometry might have. Cooling water circulated inside the titanium tube, which keeps the antenna cool and minimizes the chance of a water leak into the source. In the case of a failure of the quartz tube, air gets into the vacuum first and stops the source operation promptly. A 13.56 MHz, 2.2 kW RF power supply was used to form the plasma. An inductive matching network similar to the one presented in figure 9 (a) was used to optimize the coupling of the RF field into the plasma.

A movable magnetic filter rod setup was used to create a transverse magnetic field in front of the extraction aperture. The measured magnetic field profile at the source axis is presented in figure 30. It had a peak field of 135 G and Full Width At Half Maximum (FWHM) of 2.4 cm.

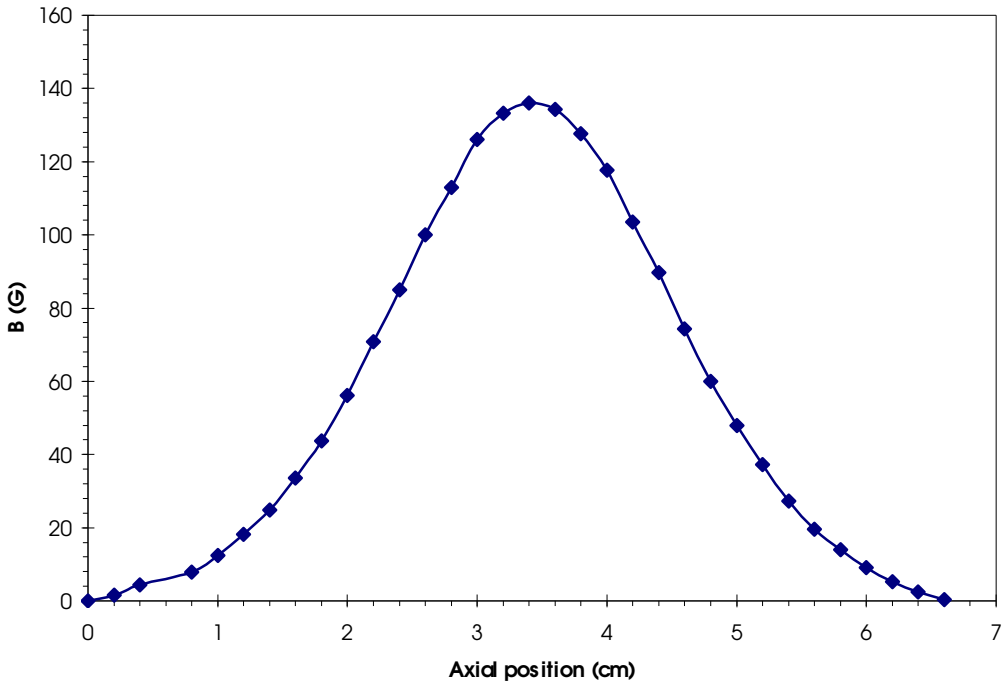

***Figure 30**. The measured transverse filter magnetic field at the axis of the source*

The filter magnetic field divides the ion source into two regions with different plasma densities and electron temperatures. The discharge region, which has energetic electrons and where most of the positive ion formation takes place, is where the RF antenna is situated. In this part of the source, some of the gas molecules are also vibrationally excited by electron impact. Some of the excited molecules will then diffuse to the extraction part of the source chamber. The magnetic field prevents the diffusion of energetic electrons into the extraction region, which is crucial for the negative ion formation as the fast electrons are very destructive for the negative ions.

Positive ions are able to diffuse through the dipole field through collisions with the neutral gas molecules, as described in section 1.4.2. Thermal, or slow electrons will diffuse through the transverse magnetic field with the positive ions. The vibrationally excited molecules then capture these slow electrons and form negative ions through the *dissociative attachment* process described in section 3.2.1.

The front plate of the ion source, where the actual plasma chamber was attached, was made of aluminum. It was insulated from the plasma chamber with an aluminum oxide insulator ring to enable the biasing of the front plate with respect to the plasma. This biasing technique in combination with the magnetic filter has been observed to reduce the amount of extracted electrons while increasing the negative ion current from the source [47].

The source was fitted with a cesium collar around the extraction aperture. The collar was a stainless-steel ring holding cesium getter wires, which will release cesium into the plasma when heated up. Pressurized air was used to control the temperature of the collar.

A stainless-steel gas delivery system compliant with toxic gas operation was constructed for the experiment. As chlorine is an extremely corrosive gas, all surfaces that were exposed to the high pressure chlorine for extended periods of time were manufactured from stainless-steel. The ion source chamber was made of copper as the source pressure is relatively low and the oxidation of the copper therefore will be slow compared to the duration of the experiment. The whole gas delivery line along with the ion source were set up inside a ventilated hood to prevent any escape of chlorine into the air in case of accidental rupture of the gas bottle or the gas delivery line.

All the o-rings that were used to make the vacuum seals in the source were of a type resistant to the corroding effects of chlorine. Special care was always taken when opening the source after operation to avoid contact of any chlorine residues with water as the reaction would create hydrochloric acid.

Figure 31 shows pictures of the ion source mounted on the test stand and a frontal shot showing the plasma chamber.

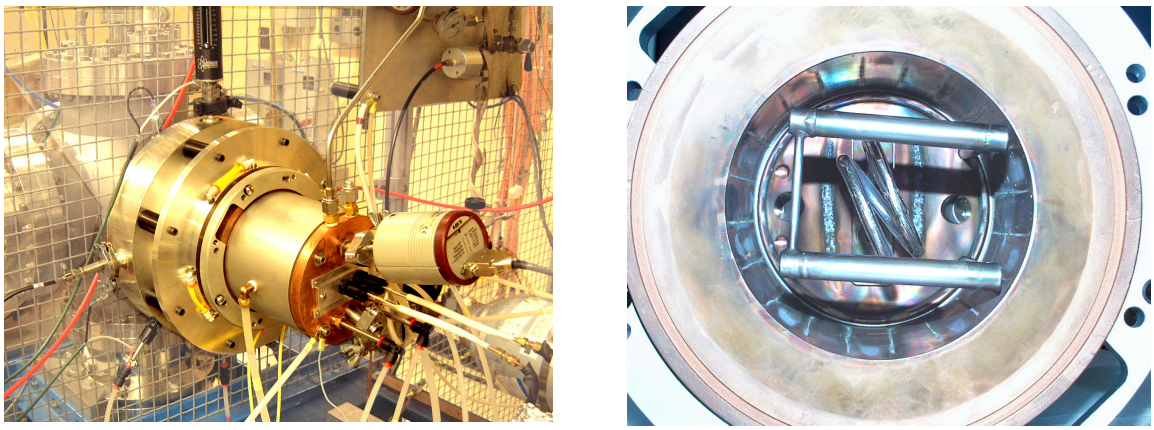

(a) *(b)*

***Figure 31**. (a) the ion source mounted on the test stand, (b) view of the plasma chamber*

6.2.2 Ion extraction

The ion extraction for the negative chlorine experiment was simulated with PBGUNS simulation code. The performance of the ion source was estimated from previous measurements with similar ion source. About 75 mA/cm^2 of positive Ar^+ ions were extracted at 2 kW of RF power from a 10 cm diameter, 20 cusp line ion source with a magnetic filter installed [48]. From figure 10 we can see that the first ionization energy for argon is 15.4 eV and for chlorine 13 eV. The mass numbers of argon and chlorine are 40 and 35, respectively. This means that the extracted positive chlorine ion density is similar to that of argon at same RF power. The extracted Ar^+ current density was used as an initial estimate for the extractable positive chlorine current density.

PBGUNS was used to optimize the extraction structure for two-electrode geometry. The plasma electrode aperture diameter was set to 2 mm, which is rather small but essential to avoid overloading the high voltage power supply by extracting too many electrons, which always accompany negative ions. The puller electrode aperture and the extraction gap were optimized using PBGUNS. The 4.6 mm gap size was selected such that the usable extraction voltage range was 10 – 25 kV, depending on the plasma density. Beam energy of 10 kV was needed to have enough beam current through the magnetic mass analyzer to have clean mass spectrums. The distance from the tip of the puller electrode to the beginning of the einzel lens was set to about 100 mm, which allows the ion beam to expand enough to the einzel lens. This is essential to enable the einzel lens to focus the beam to the dipole magnet entrance, which was a further 380 mm away from the last element of the einzel.

Figure 32 shows a plot of a PBGUNS simulation for positive chlorine ion beam. Simulation parameters were as follows: current density j = 45 mA/cm^2, electron temperature T_e = 5 eV, ion temperature T_i = 2 eV, extraction voltage U_{ex}= 25 kV and extraction gap 5 mm. The plasma region is calculated with 0.01 mm mesh size, while the rest of the geometry was calculated with 0.3 mm mesh size. The units on the axis are in cm in all the PBGUNS simulations made for this thesis unless otherwise specified.

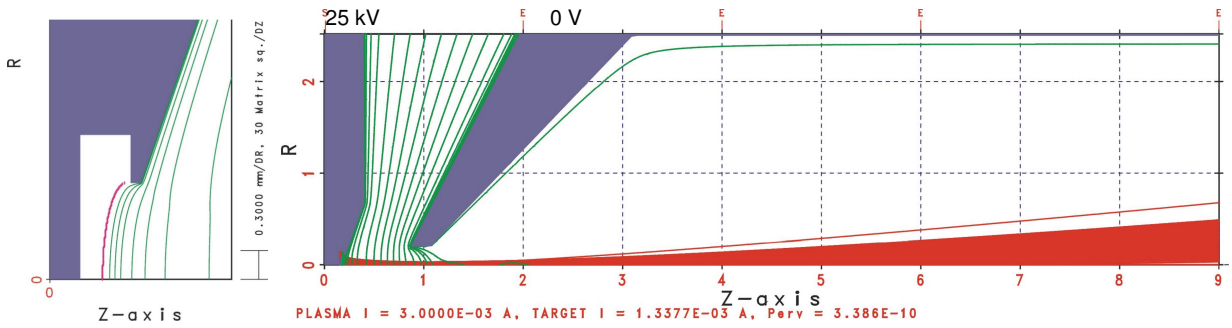

***Figure 32**. PBGUNS simulation for positive chlorine, j = 45 mA/cm^2, U_{ex} = 25 kV.*

Figure 33 shows a simulation for negative chlorine ions with the same input parameters as for the positive case above. One more parameter is needed in the case of the negative ions: the positive to negative ion ratio (PIR). This parameter has a big effect on the location and the form of the plasma meniscus and care has to be taken when choosing the value. In Figure 33 the ratio of positive to negative ions was 20, which is based on the data obtained from H^- ion source of similar structure to the one built for this work. A transverse magnetic field profile similar to the one in figure 37 was used in the simulation. Electrons were also injected into the ion beam and are swept away by the magnetic field.

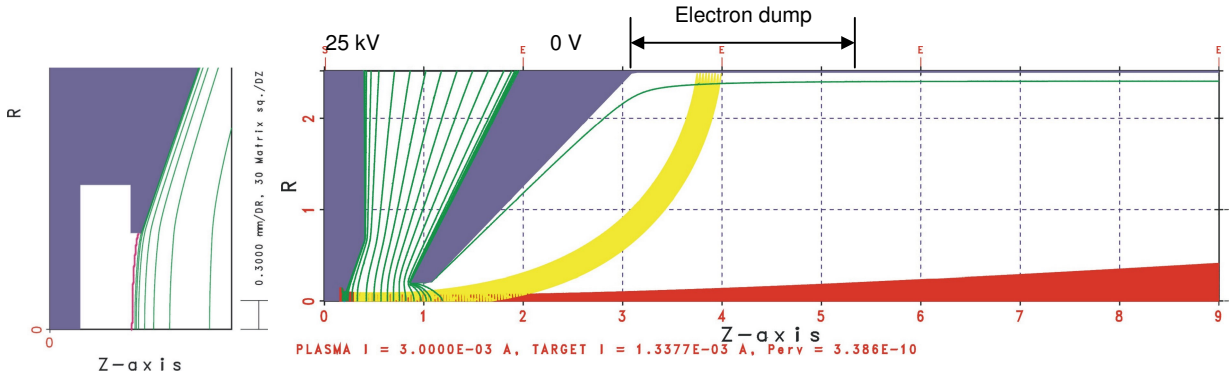

***Figure 33**. Negative chlorine simulation with j = 45 mA/cm^2, U_{ex} = 25 kV, PIR = 20.*

Figure 34 shows a negative chlorine simulation with positive to negative ion ratio of 2. This low value was assumed as the electron affinity of chlorine is high and the source geometry is optimized for negative ion production.

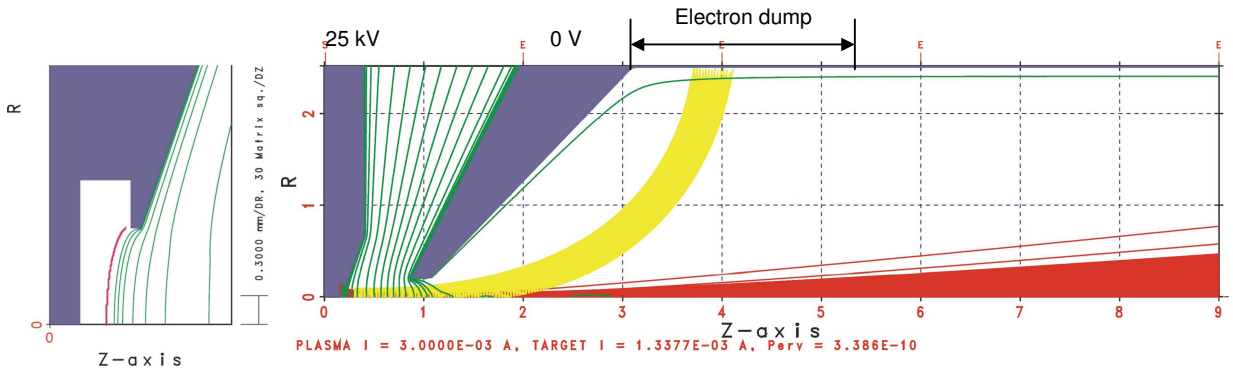

***Figure 34**. Negative chlorine simulation with j = 45 mA/cm^2, U_{ex} = 25 kV and PIR = 2.*

As it can be seen from the location and shape of the plasma meniscus in figure 34, it resembles more the positive ion case than the negative chlorine simulation with positive to negative ion ratio of 20. In the case that the positive to negative ion ratio is from 1 – 3, the meniscus and thus the ion optics for the positive and negative chlorine beam should be similar. This will be useful when comparing the ion source performance as it can be run in both positive and negative ion mode.

A PBGUNS simulation of the beam focusing with the einzel lens for the ion beam of figure 34 is shown in figure 35. The simulation starts from the end of the puller electrode and ends at the entrance to the mass analyzer magnet.

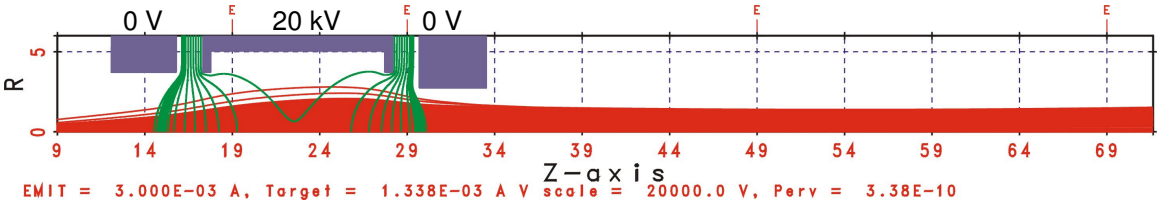

***Figure 35**. Focusing of the ion beam of figure 36 with the einzel lens to the mass analyzer magnet.*

The ion source extraction geometry was constructed with the guidelines given by the simulation runs and is shown in figure 36.

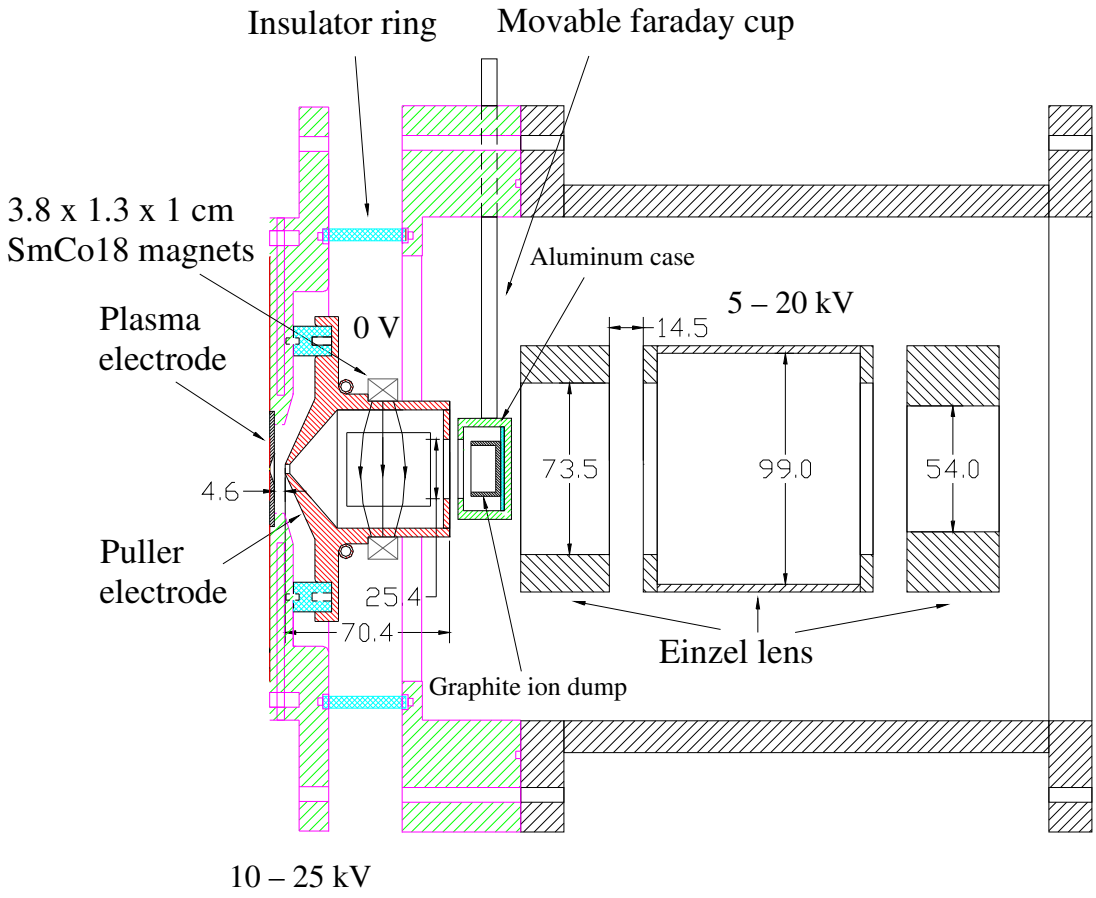

***Figure 36**. Schematic of the constructed extraction and einzel lens set up. Dimensions are in mm.*

A two-electrode extraction system was constructed consisting of a plasma electrode with 2 mm aperture diameter and a puller electrode with 4 mm aperture diameter. The gap between the electrodes was 4.6 mm. A magnetic electron filter was built into the puller. This was done by creating a transverse magnetic field across the puller electrode axis with two permanent magnets as indicated in figure 36. The electrons extracted from the ion source are deflected by the magnetic field and dumped into a water cooled copper target on the side of the puller. Ions will pass through the puller volume relatively unperturbed. This type of electron filter enables the monitoring of extracted electron current continuously and is a good indicator of any changes in the ion source even if the ion current is not monitored with the faraday cup. Figure 37 shows the measured transverse magnetic field at the axis of the ion beam through the puller electrode. The field had a peak value of 280 G and FWHM of 3.4 cm.

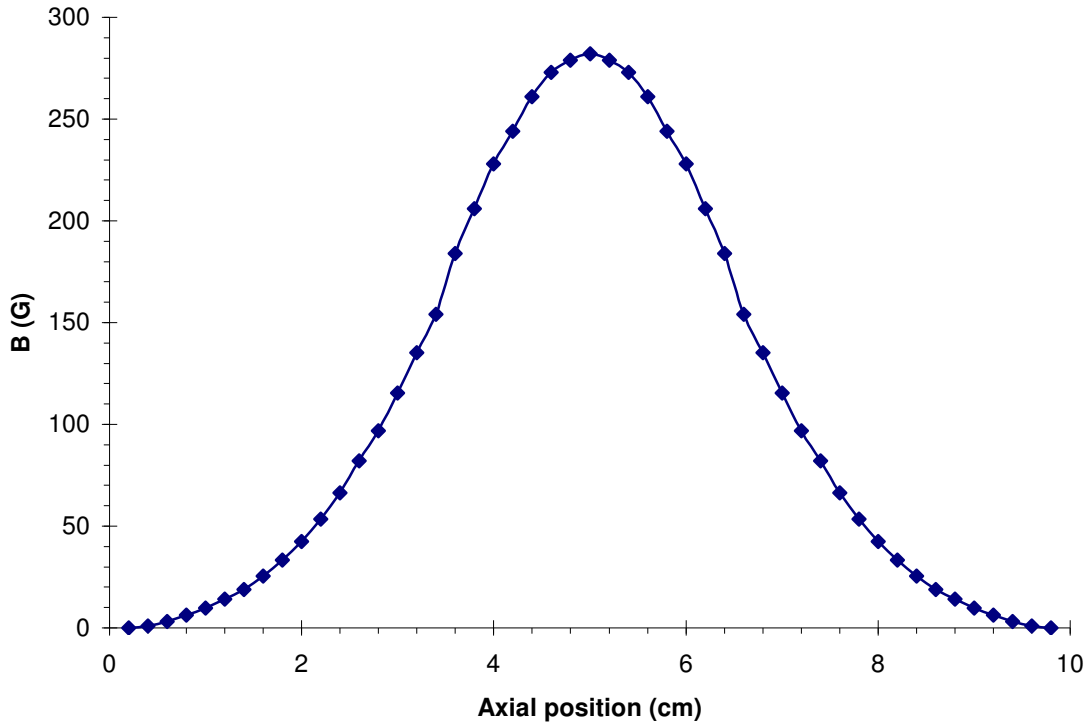

Figure 37*. The measured puller electrode electron filter magnetic field.*

The puller electrode has a 25 mm diameter aperture in the back end of the electrode. This helps to prevent the escape of any backscattered electrons from the electron dump.

A movable faraday cup was installed after the puller electrode. A graphite ion dump was placed inside an aluminum casing. The casing could be biased negatively with respect to the ion dump, which would prevent the secondary electrons created by the ion bombardment from escaping the faraday cup. The faraday cup could be moved up when the beam was injected to the mass analyzer magnet. It was quite easily replaceable by a pepper pot emittance measurement target plate.

An existing decelerating einzel lens set up was used in the experiments with minor modifications. The lens electrodes were made from stainless-steel. The outer electrodes were grounded while the middle electrode was biased to negative voltage between 5 to 15 kV.

Figure 38 (a) shows a back view of the puller electrode and 38 (b) the complete set up with the faraday cup installed.

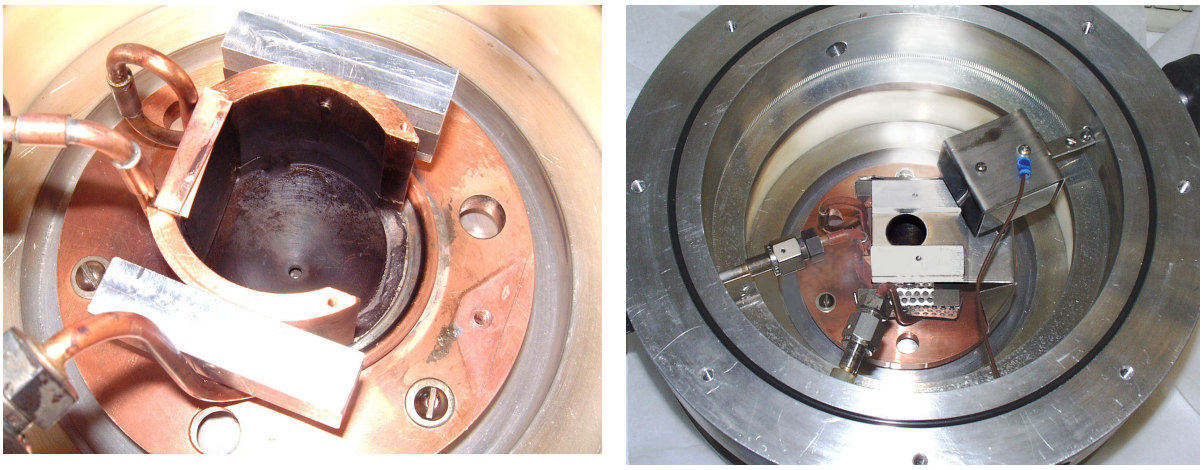

(a) *(b)*

***Figure 38**. (a) A back view of the puller electrode, (b) the complete set up with the faraday cup installed.*

6.2.3 Data acquisition and diagnostics

The test stand power supplies were controlled manually. The mass analyzer magnet had a computerized data acquisition and control system, which allowed automatic sweeps of the magnet current and plotting of the mass spectrum in digital format. This was done with LabView measurement software. The ion and electron currents were monitored with digital multimeters.

6.3 Measurements with oxygen plasma

The system was first tested using oxygen plasma. This was done to make sure that everything was functioning properly and to minimize the source operation time with chlorine, which is extremely corrosive and thus very hard on the experimental hardware.

6.3.1 Positive oxygen ions

Figure 39 shows a typical positive oxygen mass spectrum taken at 1500 W of RF power, 15 kV of acceleration voltage and 10 mTorr of source pressure.

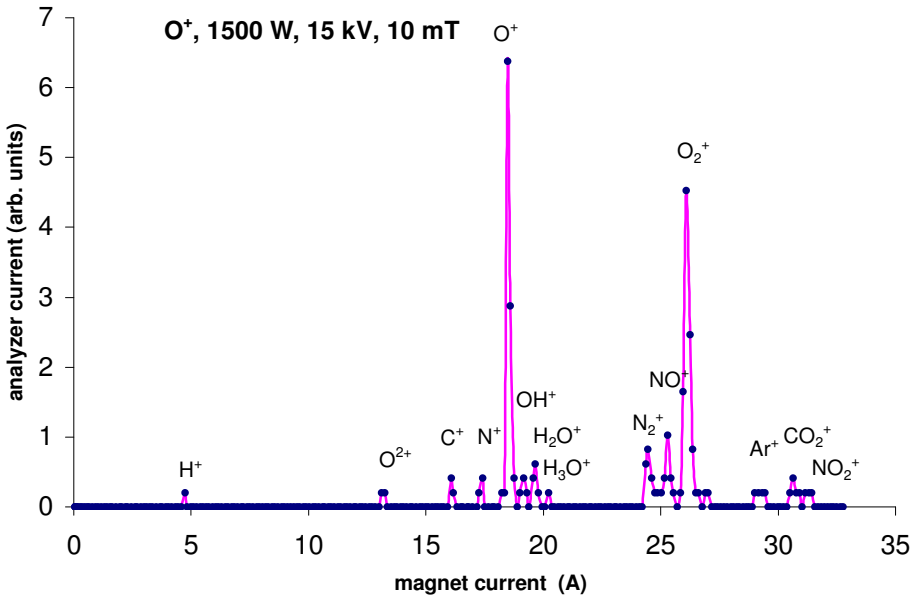

***Figure 39**. Mass spectrum for positive oxygen. Note the residual peaks from outgasing.*

Figure 40 shows positive oxygen spectrum at the same pressure and acceleration voltage but at higher RF power. The only differences to figure 39 are the higher fraction of O^+ and an emerging H_2^+ peak.

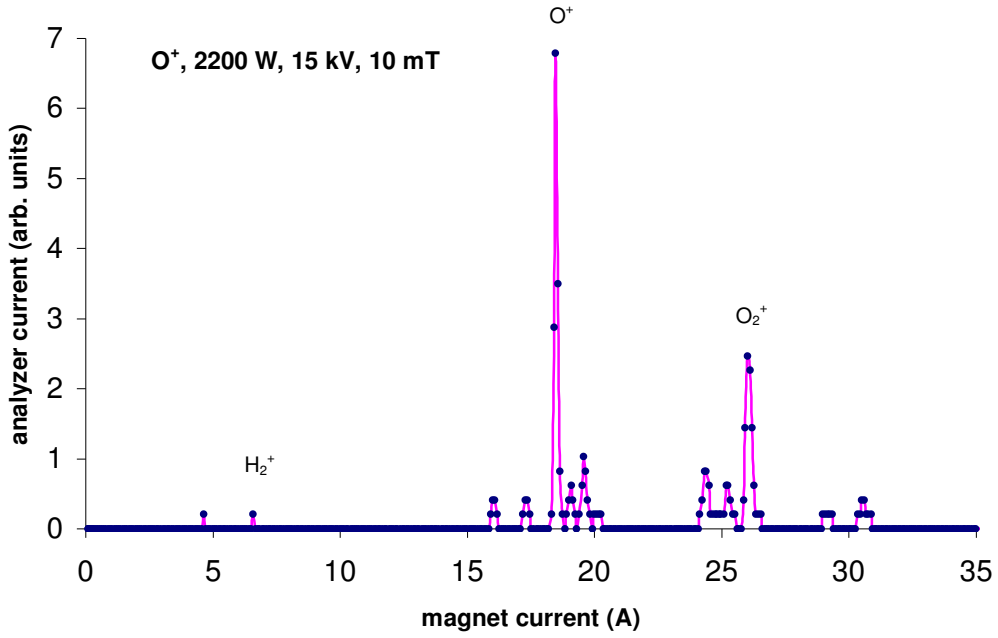

***Figure 40**. Mass spectrum for positive oxygen at 2200 W of RF power. Note the H_2^+ peak.*

As can be seen in figures 39 and 40, there are some impurities present in the source. The level of impurities went down as the source was operated for a few hours and the source cleaned up. It was especially important to get the levels of H_2O as low as possible, as chlorine reacts with water forming hydrochloric acid.

From figure 40 it can also be seen that the fraction of O^+ increases with the increasing RF power as described in section 4.1. In figure 39, 59 % of the oxygen current is O^+ while in figure 40 the fraction of O^+ is 74 %.

In figure 41 the measured total positive oxygen current as a function of accelerating voltage is presented for three different RF power levels. The measurement was done with 1.5 mm diameter extraction aperture. The magnetic filter rods were 12 mm away from the front plate in all the oxygen measurements.

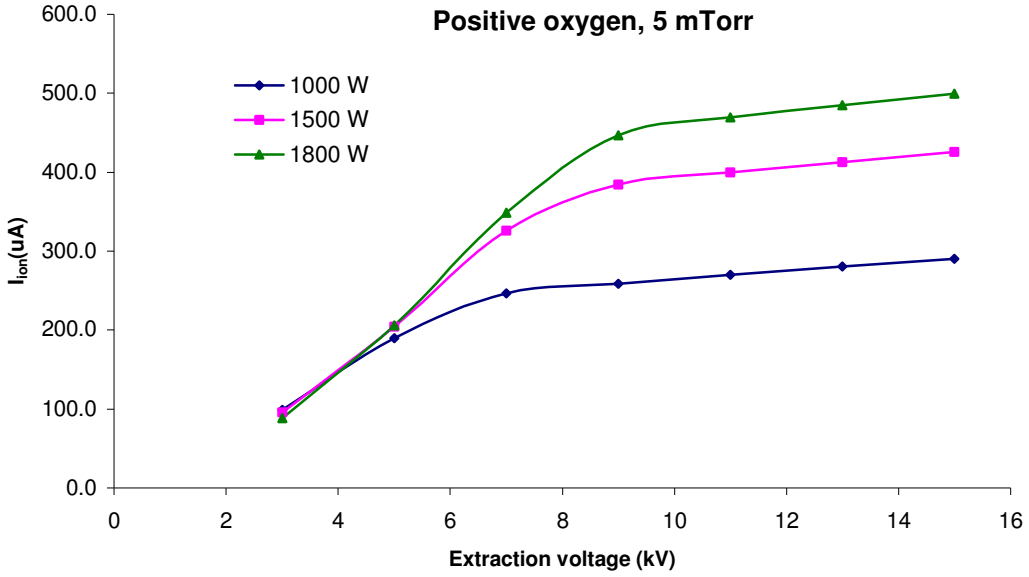

Figure 41. *Positive oxygen total current (O^+ + O_2^+) measured as a function of extraction voltage at 1 kW, 1.5 kW and 1.8 kW RF power, 5 mTorr source pressure and 1.5 mm extraction aperture.*

The saturation of the ion current can be seen in the curves of figure 41. In all cases the current reaches nearly constant value. The ion current increases with increasing extraction voltage until all the ions that diffuse into the plasma meniscus region are extracted and the current starts to saturate. The ion current is still increasing slightly even after reaching the saturation point, as the plasma meniscus is bulging more and more inside the ion source and thus the extracting area is getting larger.

The point of saturation increases with increasing RF power, as the plasma density gets higher.

Figure 42 shows the positive oxygen saturation current as a function of the RF input power. As can be seen, the current increases linearly with the increasing power.

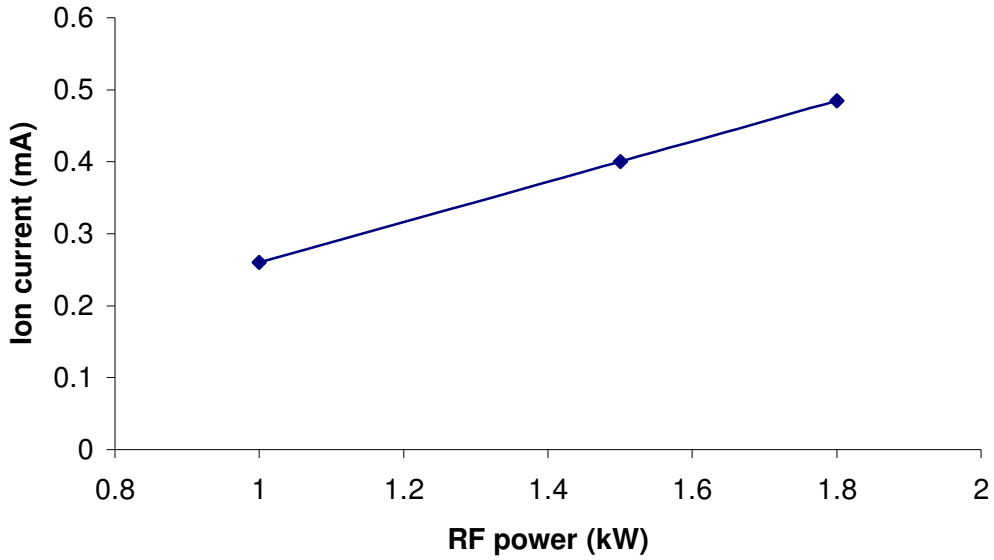

***Figure 42**. Ion saturation current for positive oxygen plasma as a function of the RF power at 5 mTorr source pressure and 1.5 mm diameter extraction aperture.*

Largest measured positive oxygen current density of 28 mA/cm^2 was achieved at 10 mTorr of source pressure and 2 kW of RF power, which was the maximum power of the RF supply. The ion species fractions were 76 % of O^+ and 24 % of O_2^+.

6.3.2 Negative oxygen ions

Next, the polarity of the extraction power supply was reversed and the negative ions were extracted from the source. Initial testing with positive oxygen ions showed that the ion source, extraction and beam diagnostics worked. A smaller 1.5 mm diameter aperture was used in the oxygen measurements in anticipation of high electron currents.

After a short time of extracting negative oxygen ions the pressure in the vacuum chamber started to climb and sparking occurred between the plasma and the puller electrodes. After opening and inspecting the extraction system it was noticed that the copper electron dump inside the puller electrode had started melting as the 50 mA electron beam was

hitting the dump at 20 keV energy. The electron beam was focused to a few millimeters wide area and the cooling of the dump was inadequate to handle the 1 kW electron beam power.

A revised electron dump was constructed from molybdenum, which has melting point of 2896 K and is much higher than the melting point for copper, 1358 K. The water cooling was also improved by increasing the size of the cooling lines. This proved to be sufficient to prevent the electron dump from melting. Graphite was also considered as the electron dump material, but as graphite is very porous, it traps air and thus takes long time to outgas. There is also an insulating oxide layer easily formed on the surface of graphite, which cannot be sputtered away easily by the electrons. This is why molybdenum was chosen.

Figure 43 shows a negative oxygen mass spectrum taken at 1.5 kW of RF power.

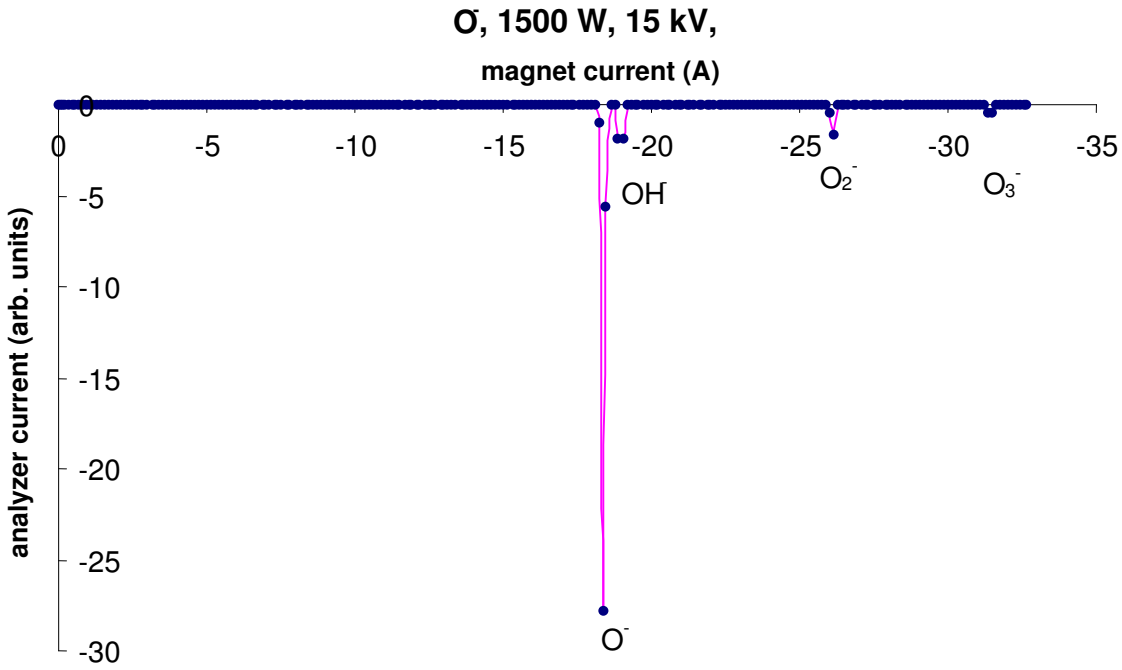

***Figure 43**. Mass spectrum for negative oxygen at 1500 W of RF power and 7 mTorr source pressure.*

As can be seen from figure 43 the negative oxygen spectrum was very clean with about 90 % of the beam being O^-.

Figure 44 shows the measured negative oxygen current as a function of extraction voltage at four different RF power levels.

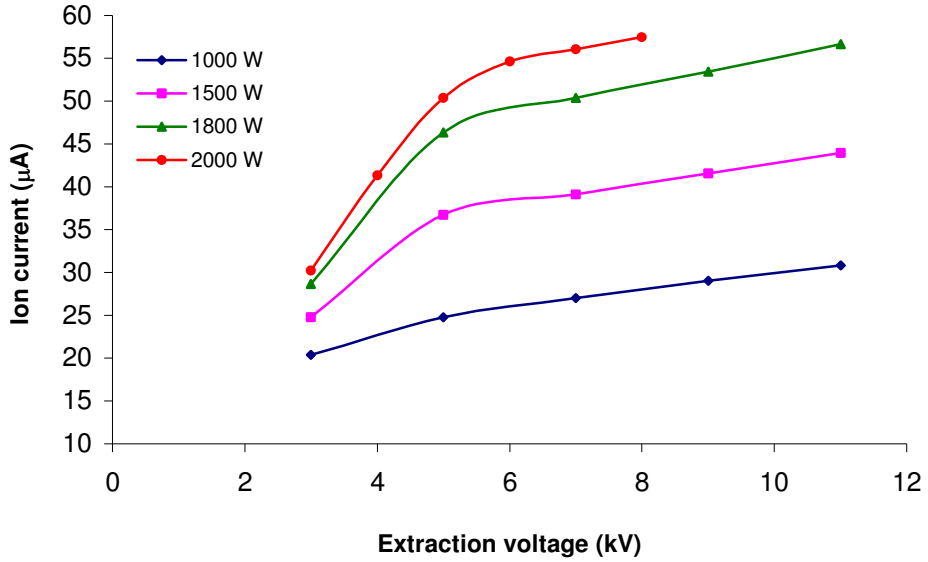

***Figure 44**. Negative oxygen total current measured as a function of extraction voltage at 1 kW, 1.5 kW, 1.8 kW and 2.0 kW RF power, 10 mTorr source pressure and 1.5 mm diameter extraction aperture.*

In figure 45 the atomic components O^+ and O^- of the measured oxygen current are plotted along the extracted electron current as a function of the extraction voltage. The data was taken at 1.5 kW of RF power and 10 mTorr of source pressure.

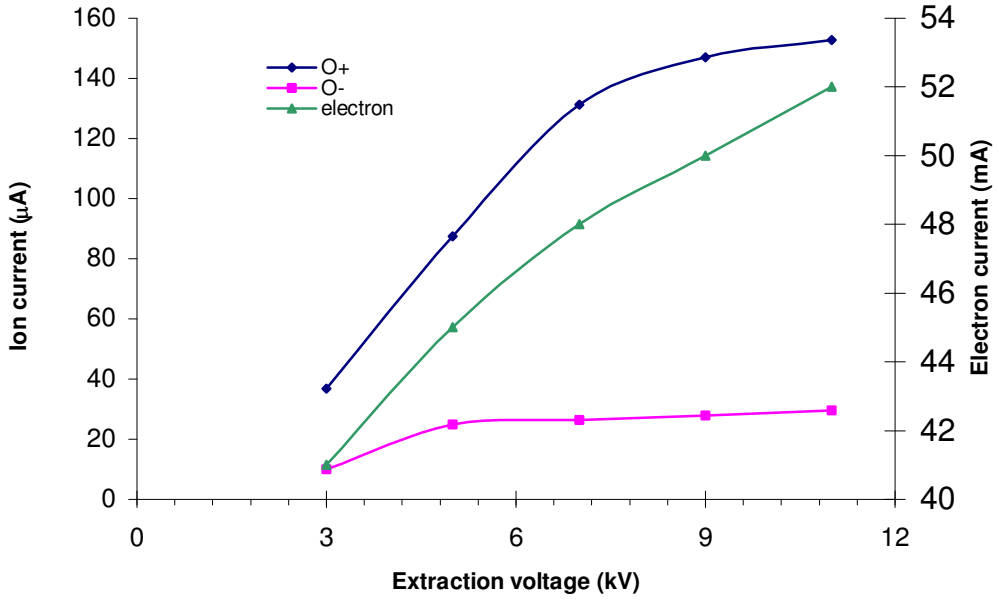

***Figure 45**. Measured O^+, O^- and electron currents at 1.5 kW RF power, 10 mTorr source pressure and 1.5 mm diameter extraction aperture.*

From figure 44 and 45, we can see that the ratio of the atomic positive and negative oxygen currents was about 6, and the electron to total negative ion current ratio was 1000! This value seems to be quite large, but if the charge neutrality condition, equation (9) is taken into account, it can be seen that the electron current indeed is quite high.

One can estimate the amount of electrons that should accompany the negative ions if both positive and negative total ion currents are known. This can be done with the following equation:

$$I_e = \sqrt{M_i \cdot 1836} \cdot \left(I_{i,+} - I_{i,-}\right) \tag{67}$$

where M_i is the mass number of the ion. In equation (67) it is assumed that the all the beam current is carried by one ion species. By using beam current values from figures 42 and 44, we can estimate using equation (67) that about 70 mA of electrons should be extracted at 1.5 kW of RF power.

Next, the biasing of the front plate to a positive voltage with respect to plasma was tested. In figure 46 the negative atomic oxygen and electron currents are plotted as a function of the front plate bias voltage.

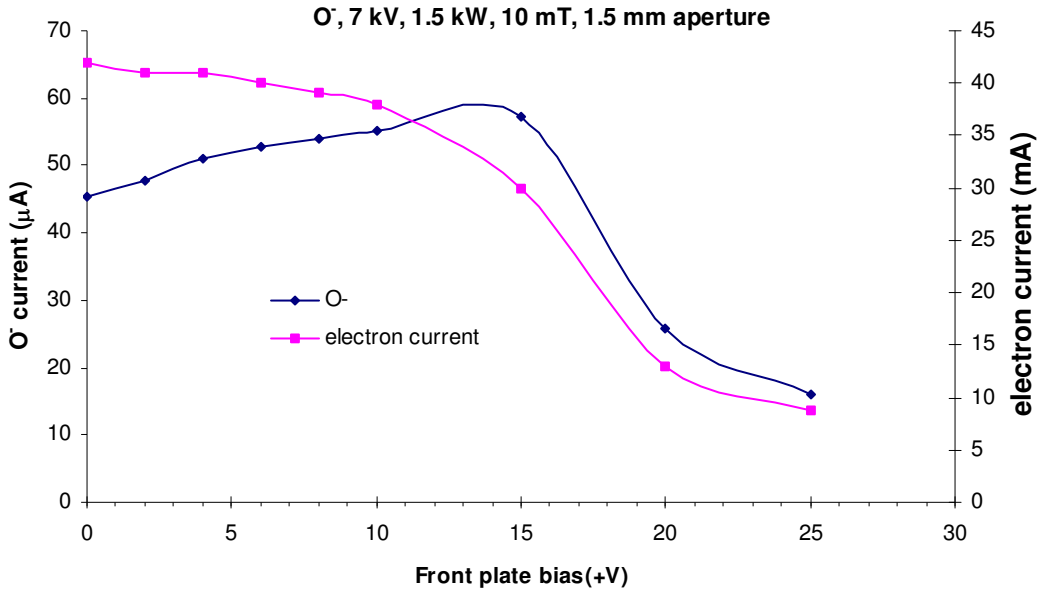

***Figure 46**. O⁻ and electron currents as a function of the front plate bias voltage.*

The O^- current increased with the front plate bias voltage reaching a maximum around +15 V bias voltage. At higher bias voltages the ion current went down rapidly. At the

same time the electron current decreased as the bias voltage increased. The decrease in the electron current and the increase in the O^- current can be explained as follows: The magnetic filter field prevents the fast electrons from getting into the extraction area of the ion source. Some of the slow electrons are able to diffuse through the magnetic field with positive ions. Usually the plasma potential in the discharge region of the ion source is more positive than in the extraction region. When the front plate is biased into a positive voltage, the plasma potential in the extraction region is raised and the potential gradient that is pulling positive ions from the discharge region into the extraction region gets smaller. This in turn lowers the influx of positive ions and the accompanying slow electrons. When the electron density goes down, the charge neutrality of the plasma enables more negative ions to diffuse into the extraction region, which explains the increase in the negative ion current.

The effect of the source gas pressure to the extracted O^- and electron currents is plotted in figure 47.

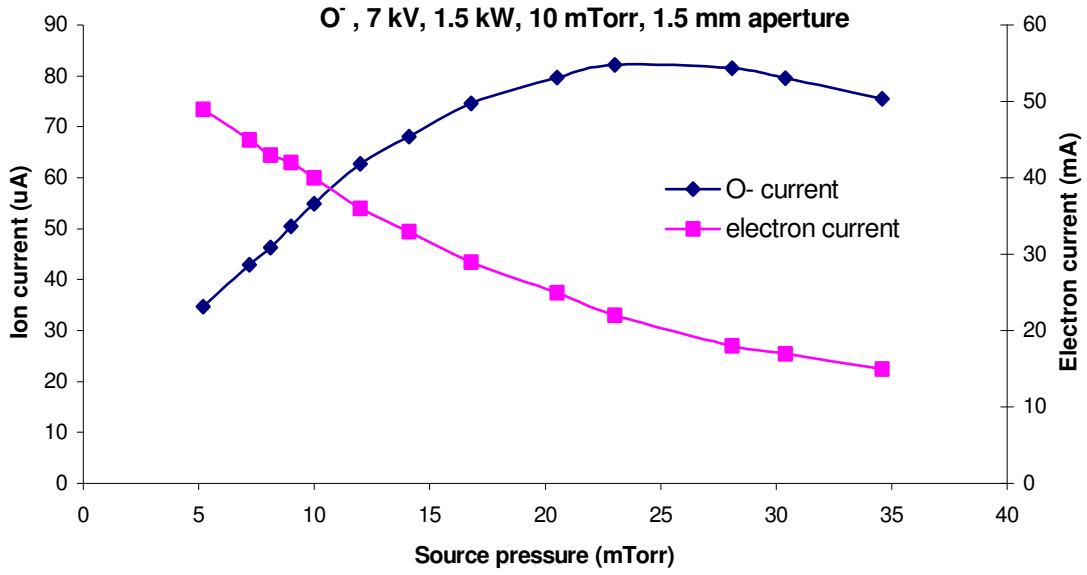

Figure 47. *The effect of source pressure on O^- and electron currents.*

As can be seen, the negative oxygen ion current reached a maximum value around 25 mTorr source pressure. The electron current was decreasing with increasing source pressure. This is probably due to the increase in the collision frequency of the fast electrons with the gas molecules, which slows down the electrons and thus lowers the extracted electron current, as can be seen from equation (8) in section 1.3.2. The lower electron temperature also increases the negative ion yield.

Figure 48 shows the measured saturation current of O^- ions as a function of ion source pressure and RF power.

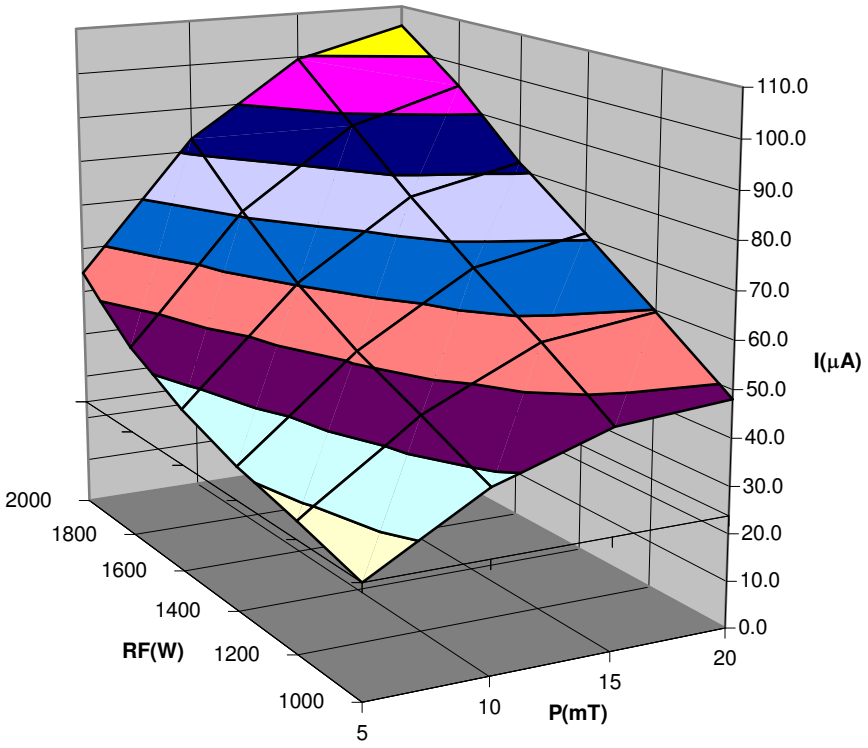

***Figure 48**. O^- saturation current extracted from a 1.5 mm diameter aperture as a function of source pressure and RF power.*

As can be seen from figure 48, the O- current increased linearly with RF power throughout the whole pressure range. The current peaked at about 20 mTorr source pressure. Maximum current density of 5.7 mA/cm^2 for O^- and 22 mA/cm^2 for O^+ was measured at 2.0 kW of RF power. The lowest achieved value for the electron-to-negative ion ratio was 300. To estimate the negative ion fraction of the total negative charge density in plasma, two things have to be taken into account. First, the electron current I_e has to be scaled to mass equivalent ion current by dividing I_e by $(m_i/m_e)^{1/2}$. Second, the temperature difference of electrons and negative ions has to be taken into account. In general, T_e can be estimated to be an order of magnitude larger than T_i in volume plasma. This means that the mass scaled, ion equivalent of the electron current has to be divided by $(10)^{1/2} \approx 3$. These above mentioned effects can be combined into a scaled electron current equation (68)

$$I_{e,scaled} = I_e / \left(3\sqrt{m_i / m_e}\right) \tag{68}$$

If I_i = 5.7 mA and $I_e = 300 \cdot 5.7$ mA = 1710 mA, $I_{e,scaled}$ = 3.3 mA. This would mean that 63 % of the negative charge in oxygen plasma would be O^- and 37 % electrons.

6.4 Measurements with chlorine plasma

After testing the ion source and diagnostics with oxygen, the source operation with Cl_2 was started. A 2 mm diameter extraction aperture was installed for the chlorine measurements as the higher electron affinity of chlorine was anticipated to increase the amount of negative ions and decrease the amount of electrons extracted from the source. The gas lines were baked and pumped down to remove any water vapor left in the tubing and the valves.

6.4.1 Positive chlorine ions

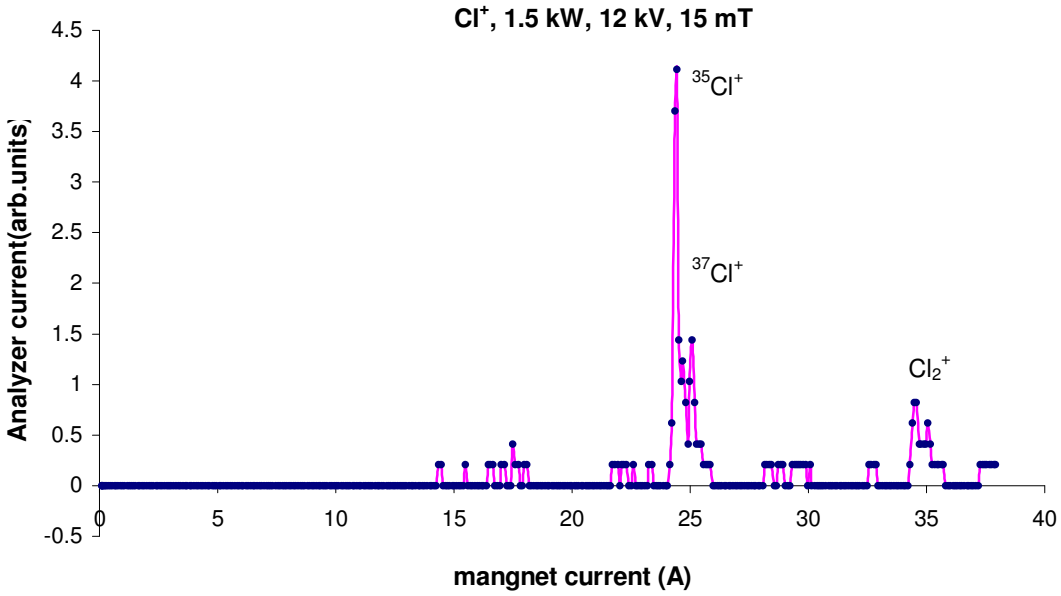

***Figure 49**. Positive chlorine spectrum at 1.5 kW RF power and 15 mTorr source pressure.*

Figure 49 shows a typical measured positive chlorine spectrum. In this spectrum the two isotopes of chlorine with mass numbers 35 and 37 can be seen. The relative peak heights of the isotopes 35 and 37 in the spectrum match well with the 76 % and 24 % natural abundance of the two isotopes. The molecular ion peak Cl_2^+ consists of three peaks with mass numbers of 70, 72 and 74. About 80 % of the positive chlorine beam was atomic at 1.5 kW RF power. The atomic chlorine percentage varied between 75 % - 85 % at RF powers from 1 kW – 2.2 kW and source pressures of 5 mTorr – 35 mTorr. This is much less than the variation in the case of atomic positive oxygen.

In figure 50 the measured positive chlorine total ion current is plotted as a function of the extraction voltage. If the positive chlorine saturation current of 0.85 mA from figure 50 is compared to the measured positive oxygen saturation current at 1 kW in figure 41, it can

be seen that the chlorine current was about factor of three higher. This is due to the fact that the electron impact ionization cross section increases with the mass number of the molecule [15], as can be seen in figure 11.

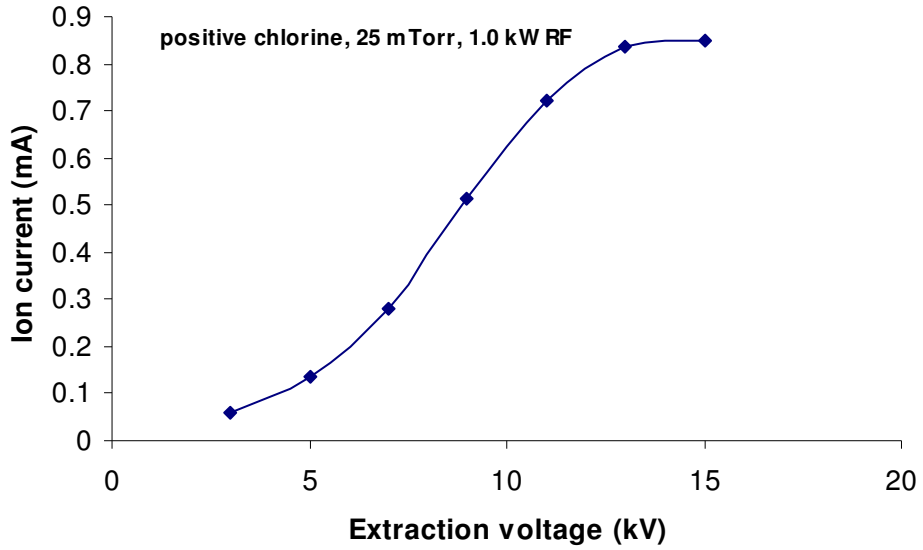

***Figure 50**. Measured positive chlorine total ion current from a 2 mm diameter extraction aperture at 10 mTorr source pressure and 1 kW RF power.*

Figure 51 shows the positive chlorine current as a function of source pressure. The positive chlorine current peaks slightly around 25 mTorr source pressure.

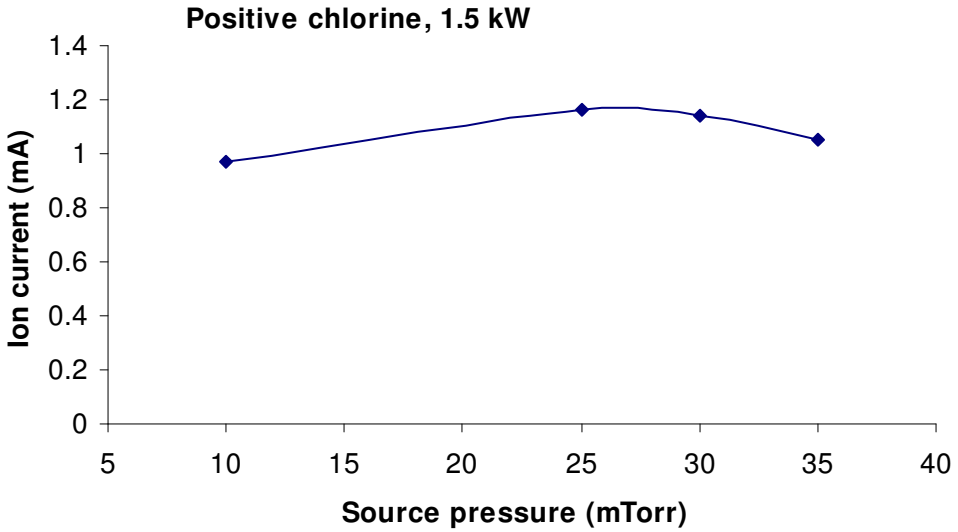

***Figure 51**. Measured positive chlorine current as a function of source pressure at 1.5 kW RF power, 2 mm diameter extraction aperture.*

Figure 52 shows the measured positive chlorine current as a function of RF power. The current increases linearly with RF power, as expected.

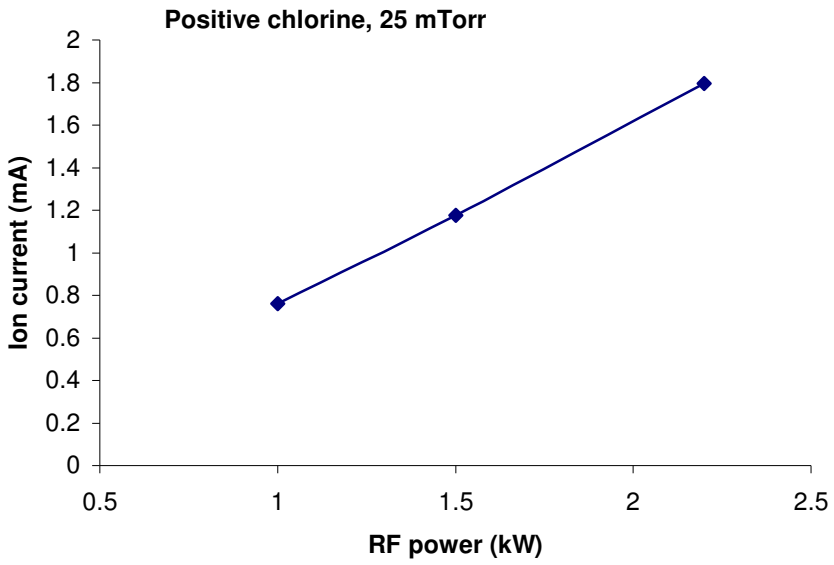

***Figure 52**. Measured positive chlorine current as a function of RF power at 25 mTorr source pressure and 2 mm diameter extraction aperture.*

Total positive chlorine current density of 57 mA/cm^2 was measured at 2.2 kW of RF power and 25 mTorr of source pressure. About 85 % of the beam was atomic chlorine.

6.4.2 Negative chlorine ions

Negative chlorine measurements were started using a 1.5 mm diameter extraction aperture. Figure 53 shows measured negative chlorine spectrum.

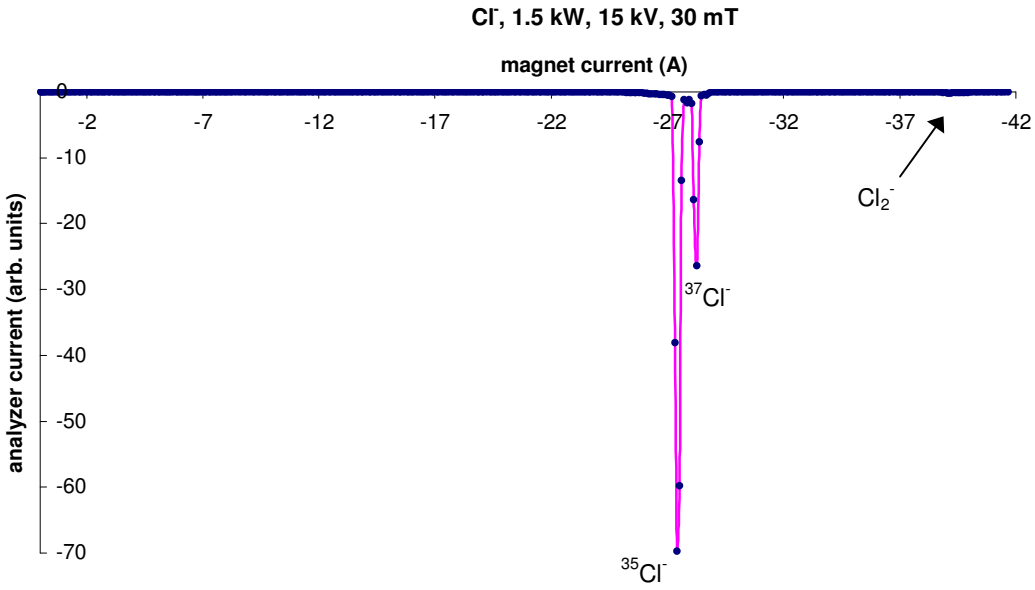

***Figure 53**. Negative chlorine ion spectrum at 1.5 kW of RF power and 30 mTorr source pressure.*

As can be seen from figure 53 the negative chlorine spectrum was very clean. 99.8 % of the beam was atomic negative chlorine and only a very small molecular peak was seen. The spectrum remained very similar to the one showed in figure 53 throughout the range of different RF power levels and source gas pressures.

Next, the ion currents for both negative and positive chlorine were measured with same conditions maintained in the ion source as closely as possible. In figure 54 the negative and positive chlorine ion current and the electron current are plotted as a function of the extraction voltage.

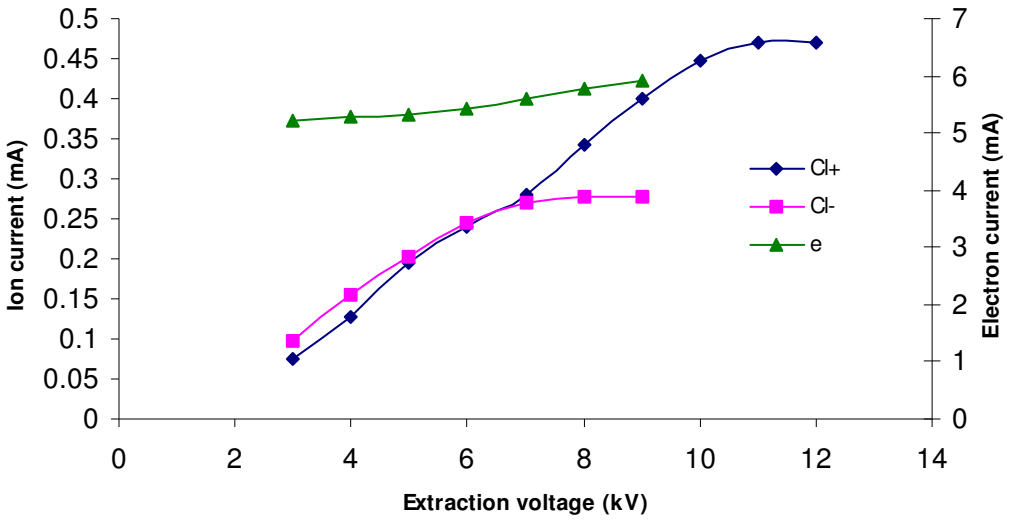

***Figure 54**. Measured negative and positive chlorine ion currents and the electron current as a function of the extraction voltage at 1.5 kW RF power, 10 mTorr source pressure, 1.5 mm diameter extraction aperture and no front plate bias.*

As can be seen from figure 54, the electron current was quite low. This indicated that the extraction aperture could be enlarged, as the electron current and thus the load of the power supplies and the electron dump was small.

Different antenna geometry was tried to compare the effect of the loop axis direction to the ion and electron currents. In figure 55 the two antennas used in the measurement are shown. The antenna on the left is the transverse 1.5 loop antenna that was installed in the source originally and the one on the right is the axial 2.5 loop antenna.

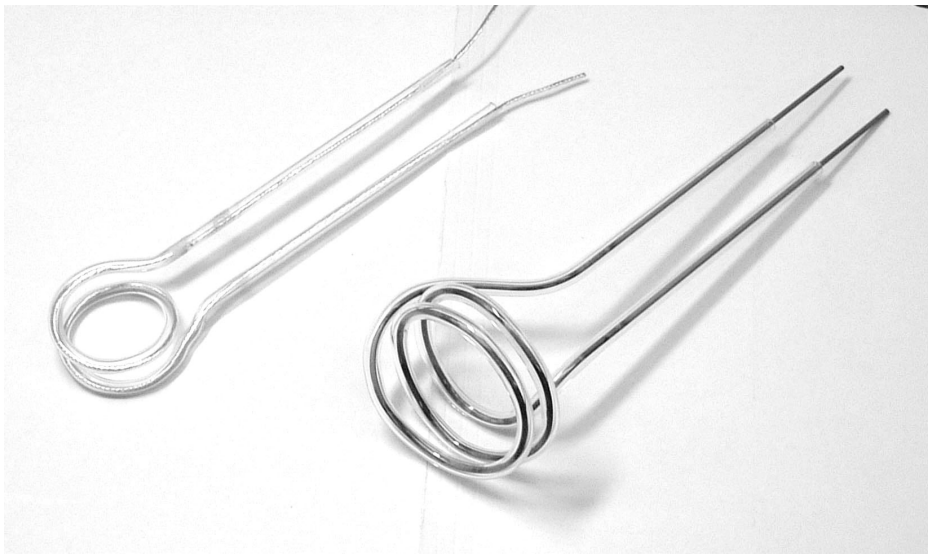

***Figure 55**. Two antenna geometries used in the chlorine experiment. The antenna on the left one is the transverse loop antenna while the one on the right is the axial loop antenna.*

In figure 56 the measured negative chlorine ion and electron currents are plotted for the transverse and axial antenna geometry at 1 kW RF power.

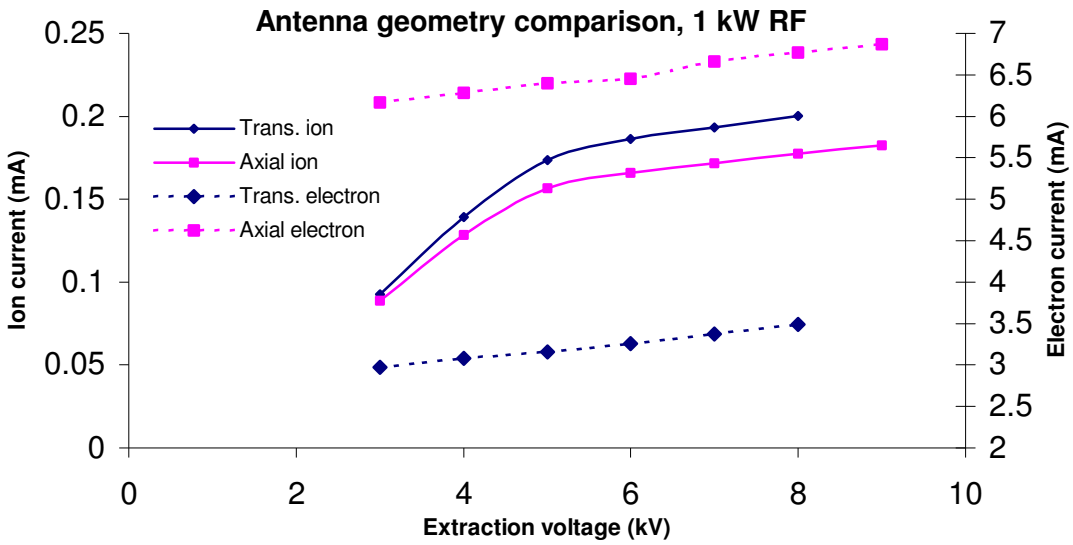

***Figure 56**. Negative chlorine ion and electron currents as a function of the extraction voltage for transverse and axial loop antennas.*

As can be seen from figure 56, the ion currents were very similar for both antenna geometries, but the electron current in the case of the axial antenna was factor of 2 – 3 higher than with the transverse antenna. This was an indication that the RF field couples

more to the extraction region of the ion source in the case of the axial antenna. The coupled RF field increases the amount of fast electrons in the extraction area, which increases the electron current and destroys more negative chlorine ions. Electrons are then taking the place of the destroyed negative ions, which increases the extracted electron current further.

Similar comparisons of different antenna geometries in multicusp ion sources have been made by axial energy spread measurements for ion beams [49]. Based on the antenna geometry comparison above the transverse antenna was used for the rest of the measurements.

After the antenna test a 2 mm diameter extraction aperture was installed into the source. The effect of the front plate bias on the negative ion and electron currents was measured next. In figure 57 the ion and electron currents are plotted as a function of the front plate bias.

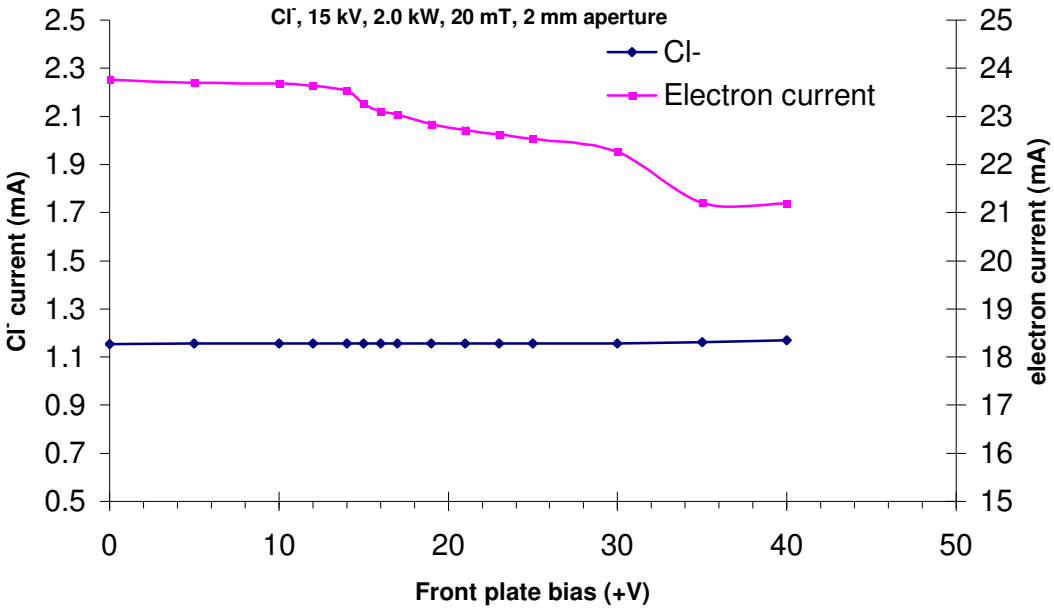

***Figure 57**. Effect of front plate bias voltage on negative chlorine ion and electron current at 2 kW of RF power and 20 mTorr source pressure.*

As figure 57 shows, that the front plate bias had very little effect on the negative chlorine current. The ion current increased by 1 %, or 0.01 mA, and the electron current decreased correspondingly by 10 %, or 2.5 mA, when the front plate was biased from 0 V to +40 V.

The source pressure can have a very big effect on negative ion and electron currents. The negative chlorine ion and electron currents are plotted as a function of the source pressure at figure 58.

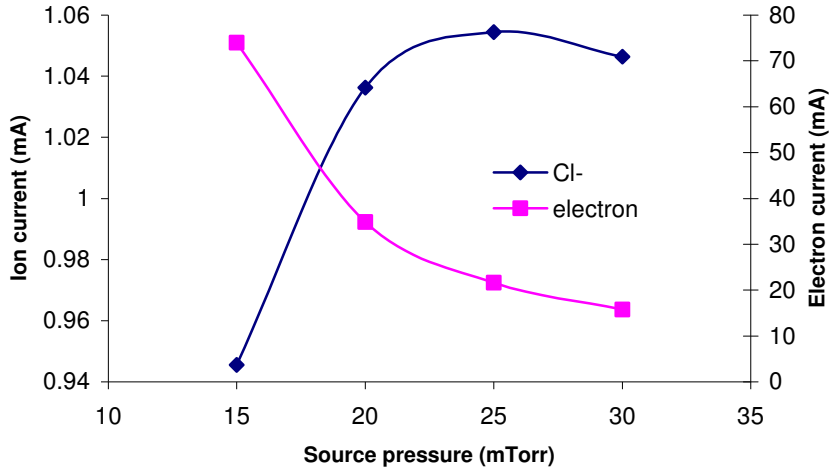

***Figure 58**. Negative chlorine ion and electron currents as a function of source pressure at 2 kW RF power.*

The ion current had a maximum at around 25 mTorr source pressure. The electron current decreased steadily with increasing source pressure similar to the oxygen measurement presented in figure 47.

From figures 57 and 58 it can be seen that the negative chlorine current changes very little as a function of source pressure and front plate bias. The same tests had much bigger effect on negative oxygen ion current, which can be explained by the lower electron affinity and thus negative ion fraction in the case of oxygen.

The effect of the ion source filter magnet position to the negative ion and electron currents was studied. In figure 59 the negative chlorine ion and electron currents are plotted as a function of the filter magnet distance from the front plate. The ion current decreased slightly with increasing filter distance from the front plate. The electron current had a minimum around 16 mm filter position, after which it started to increase. This was probably due to the fact that more energetic electrons could find their way around the filter rods. The larger fast electron concentration will also explain the decreasing ion current as the fast electrons are destructive to negative ions.

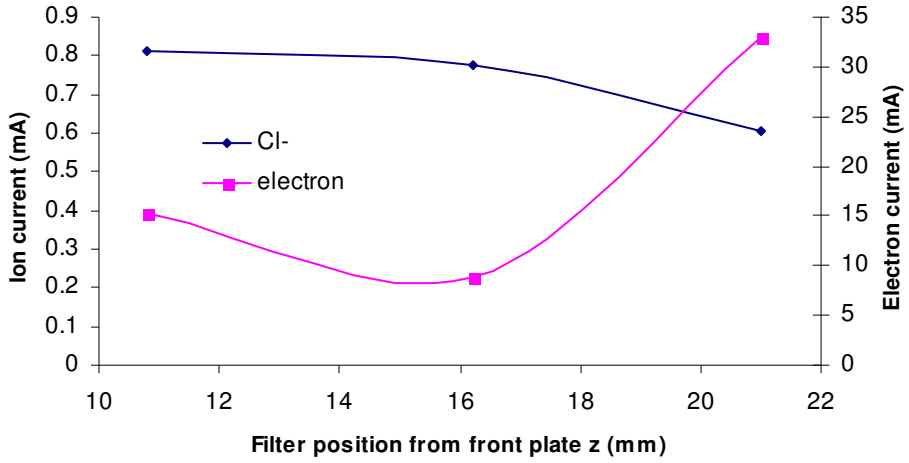

***Figure 59**. Effect of the axial position of the ion source filter magnets on the negative chlorine ion and electron currents at 1.5 kW RF power and 30 mTorr source pressure.*

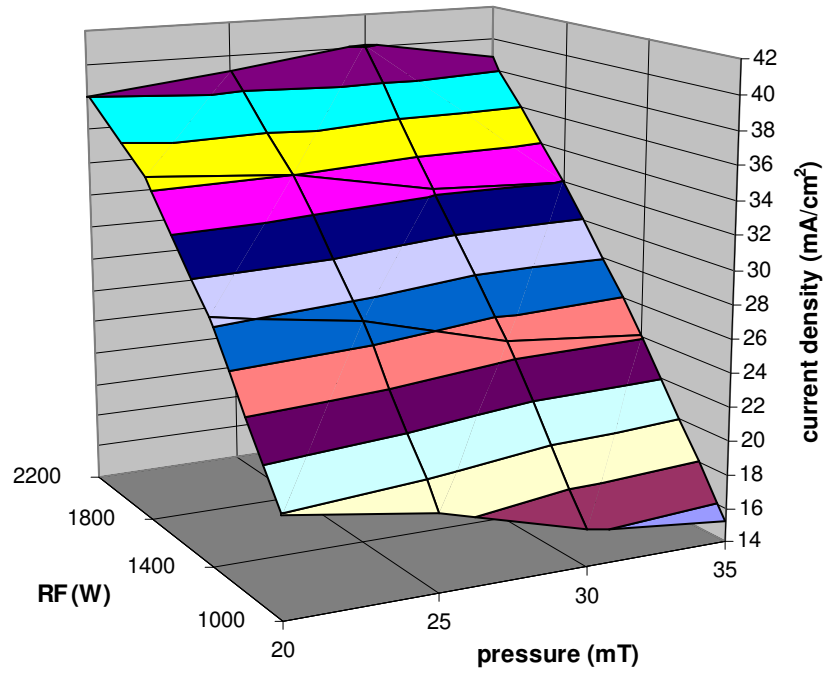

***Figure 60**. Negative chlorine ion current density as a function of RF power and source pressure.*

In figure 60 the negative chlorine ion current density is plotted as a function of the RF power and source pressure. As can be seen from figure 60, the maximum current density was about 40 mA/cm^2 at 30 mTorr source pressure. With decreasing RF power the maximum current density was reached at smaller source pressure. The downside in operating the source at lower pressure is that the electron current shoots up rapidly when the pressure goes down, as can be seen from figure 58.

After optimizing the antenna geometry, front plate bias and the source filter magnet position, a maximum negative chlorine current density of 45 mA/cm^2 was measured at 2.2 kW RF power, 32 mTorr source pressure, 15 mm axial filter position and +30 V front plate bias. It was found that 99.8 % of the beam was atomic Cl^- and the electron to negative ion ratio was 7. Positive to negative chlorine ion ratio was 1.3. By using equation (68) and the above mentioned negative chlorine current density and electron to negative ion ratio, the Cl^- fraction in the chlorine plasma was estimated to be as high as 99 %. When this value is compared to the negative ion fraction of 63 % in the case of oxygen plasma, the effect of the electron affinity (3.6 eV for Cl and 1.46 eV for O) on the negative ionization efficiency is quite obvious.

The effect of cesium on negative chlorine ion and electron currents was studied by adding a collar with cesium getter wires around the extraction aperture. The inner diameter of the collar was 20 mm and the length was 20 mm. Eight cesium getter wires were installed into fitting grooves. The collar plate is shown in figure 61.

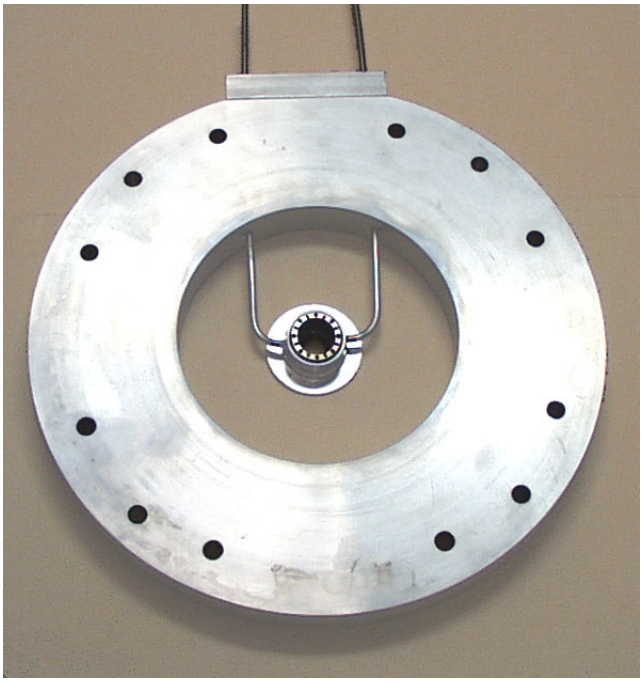

Figure 61*. The cesium collar used in the measurements.*

Figure 62 shows the measured negative chlorine ion current for the case without the collar and with the collar with and without cesium added. As can be seen, the collar decreased the ion current by a factor of three from the value measured without the collar. This follows from the fact that the collar blocks the diffusion of plasma particles into the

extraction aperture from all but the axial direction. After the cesium was added, the collar was heated gradually and the release of cesium was controlled by monitoring the source pressure. There was no increase in the ion current observed at any stage of the measurement, the ion current was actually smaller than without the cesium.

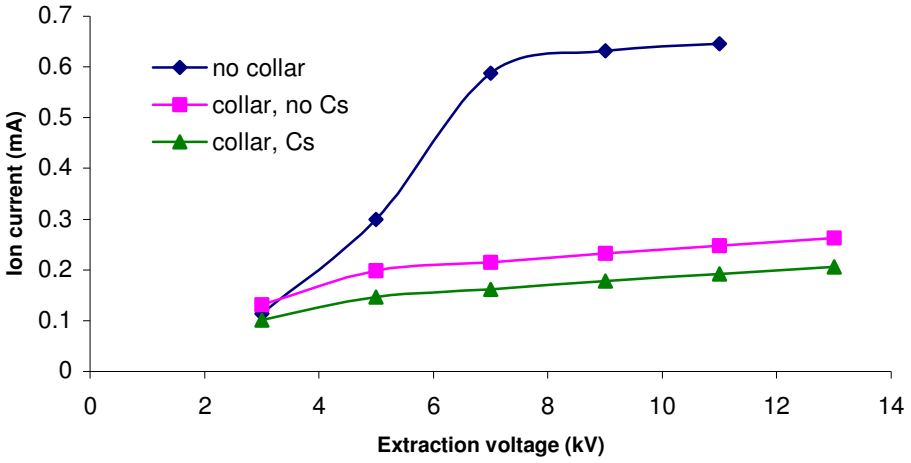

***Figure 62**.The effect of cesium on the negative chlorine ion current.*

The effect of the cesium on the extracted electron current is shown in figure 63. As can be seen, the addition of collar reduced the electron current by a factor of three. The addition of cesium had a striking effect on the electron current, as it dropped more than an order of magnitude from 2 mA to 0.15 mA.

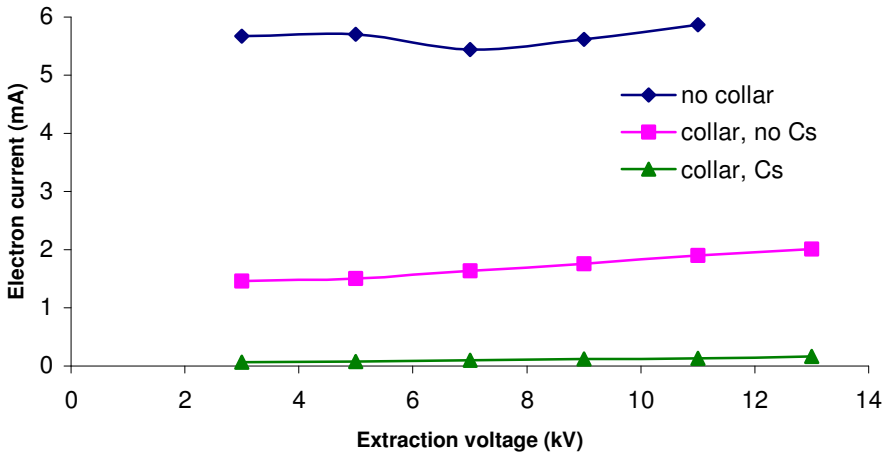

***Figure 63**. The effect of cesium on the electron current.*

Cesium gives a very big increase in the negative ion current in a case of lower electron affinity atoms like hydrogen [50]. But in the case of chlorine most of the negative charge in the extraction area is already carried by the ions, so the addition of cesium does not have

any positive effect. The electron current goes down because the massive cesium atoms have a very big collision cross section with the electrons and thus cesium "binds" electrons into these collisions and lowers the electron temperature and thus the influx of electrons into the extraction aperture area.

The ion beam emittance was estimated for both positive and negative chlorine ions. A pepper pot emittance measurement device was built and installed in the ion extraction column. A star shaped pattern of 0.25 mm diameter holes were drilled into a mask, which was placed at the exit of the puller electrode. The faraday cup was replaced by a copper target plate. Detailed description of the measurement technique is given in reference 52. In figure 64, the pepper pot mask and the target plate after an exposure are shown.

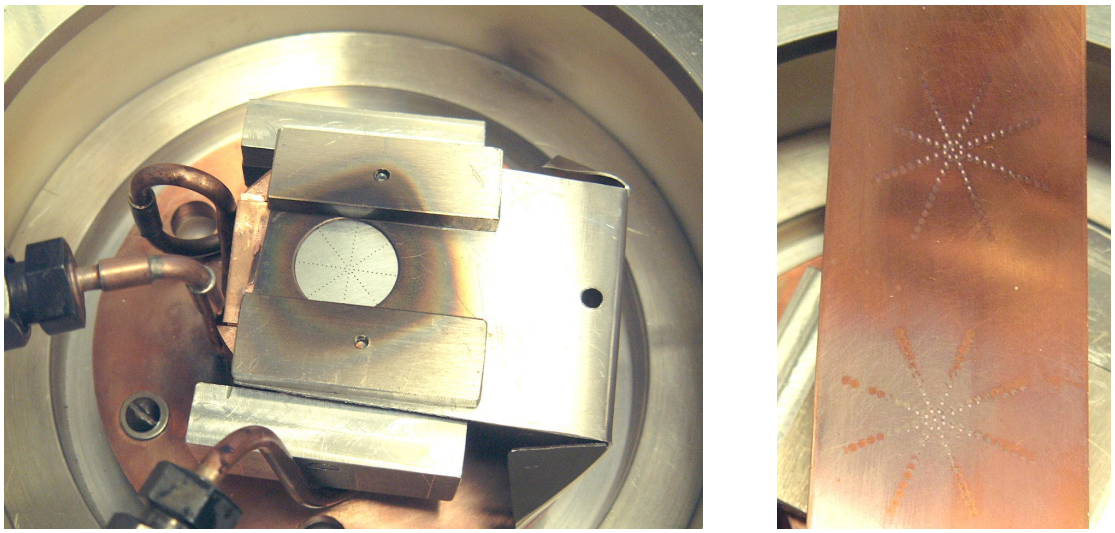

(a) *(b)*

***Figure 64**. (a) pepper pot emittance measurement mask, (b) target plate after a sample exposure.*

The ion source was operated at 1.5 kW RF power and 35 mTorr source pressure for both positive and negative ions during the emittance measurement. An earlier measurement at the same source parameters gave a positive chlorine current of 0.83 mA and a negative chlorine current of 0.65 mA. The measurement was done in both parallel and transverse direction to the puller electrode magnetic field, as the field distorts the ion beam in the direction transverse to the magnetic field.

From the spot size in the target plate the ion transverse temperatures were determined for positive and negative chlorine. The temperatures in parallel and transverse directions to

the magnetic field for the negative chlorine were 0.3 eV and 0.5 eV, respectively. For positive chlorine the temperatures were 0.2 eV and 0.5 eV.

In figure 65 the emittance pattern for positive and negative chlorine are shown. An approximate ellipse that holds the beam points inside was drawn in both cases. The area of the ellipse gives the emittance according to equation (58).

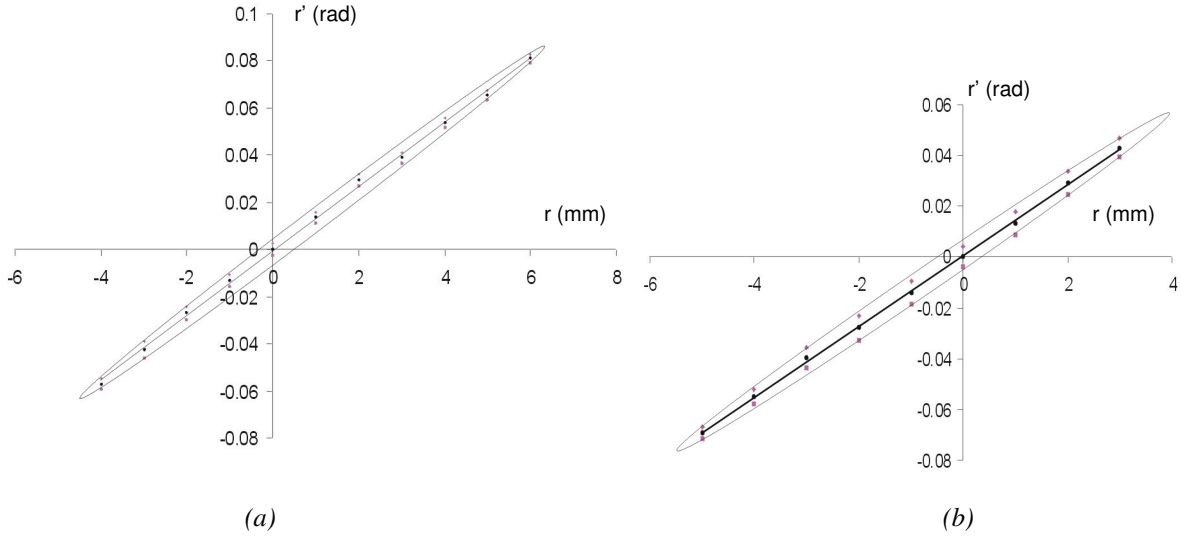

Figure 65. *(a) Positive chlorine and (b) negative chlorine ion beam emittance at 13 kV extraction voltage, 35 mTorr source pressure and 1.5 kW RF power.* I_{Cl}*+ = 0.83 mA,* I_{Cl}*- = 0.65 mA.*

The half axis of the emittance ellipses in figure 65 were determined and the un-normalized and normalized emittance was calculated using equations (58) and (59). For positive chlorine beam the emittance $\varepsilon = 134 \cdot \pi \cdot mm \cdot mrad$ and the normalized emittance $\varepsilon_n = 0.12 \cdot \pi \cdot mm \cdot mrad$. For negative chlorine beam $\varepsilon = 157 \cdot \pi \cdot mm \cdot mrad$ and $\varepsilon_n = 0.14 \cdot \pi \cdot mm \cdot mrad$. The positive ion emittance was a little smaller than the negative one, which was already indicated by the fact that the transverse ion temperature of the positive chlorine beam was smaller.

Figure 66 shows the emittance figures calculated with PBGUNS for positive and negative chlorine beam with the same parameters as in the emittance measurement above.

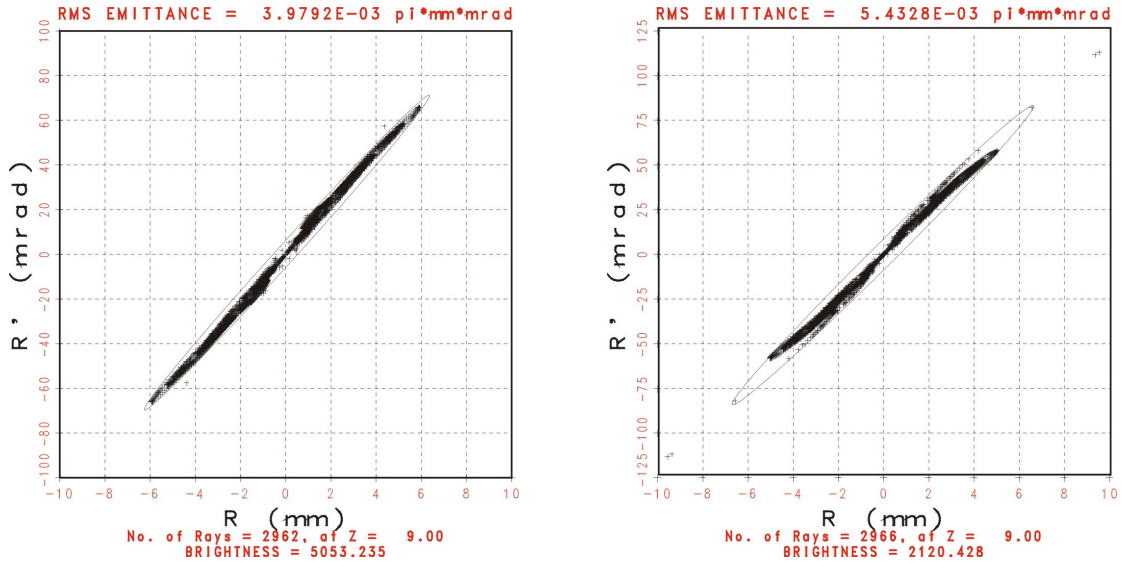

(a) *(b)*

***Figure 66**. Emittance pattern for (a) Cl^+ -ion beam and (b) Cl^- -ion beam.*

An ellipse covering the data points was drawn for the data in figure 66 and the emittance and normalized emittance were calculated. For positive chlorine simulation, $\varepsilon = 87 \cdot \pi \cdot mm \cdot mrad$ and $\varepsilon_n = 0.08 \cdot \pi \cdot mm \cdot mrad$. For negative chlorine, $\varepsilon = 110 \cdot \pi \cdot mm \cdot mrad$ and $\varepsilon_n = 0.10 \cdot \pi \cdot mm \cdot mrad$. These values are about 30 % smaller than the measured emittance values. This is probably due to the fact that the transverse magnetic field effects are not taken into account in the simulation.

7. Negative surface ion source development for semiconductor industry

Modern society is relying increasingly on integrated circuit technology based on semiconductor materials. Everything from a microwave oven to a personal computer is controlled by a microprocessor consisting of millions of circuit components integrated on a single semiconductor crystal. Silicon and germanium, which are the most commonly used circuit materials, are quite poor conductors in pure form. These materials contain no free electrons in the conduction band as all four valence electrons are bound in covalent bonds with neighboring atoms.

A very efficient way of increasing the conductivity of semiconductor materials is by adding minute amounts of impurities in the lattice structure. Usually only few parts per million of these additives are needed to dramatically change the behavior of the semiconductor crystal.

If the added material is increasing the amount of free electrons in the lattice, it is called an n-type dopant and the semiconductor material is n-type. Typical n-type additives are arsenic, antimony, bismuth, and phosphorous, which have five valence electrons and are called pentavalent elements.

If the impurity atom has fewer electrons than the semiconductor atom, there will be a hole in one of the covalent bonds, i.e. a missing electron. These holes act as charge carriers and the material is called p-type semiconductor. Most commonly used p-type impurity is boron, which is a trivalent element.

Most common methods of doping are ion beam implantation, direct deposition by heating, gas diffusion and liquid dopant spray-on process. In this work a new type of ion source was built and tested for negative boron production for ion beam implantation.

7.1 Motivation for the experiment

Negative ions have advantages in comparison to positive ions in ion implantation. When the implanted positive ions hit the target surface, a secondary electron cascade is emitted. If the target surface is insulating, like SiO_2 for example, it will charge up to the acceleration voltage of the ion beam and cause a voltage breakdown. When negative ions are used, on the other hand, the emitted charge of the secondary electrons is balanced by the negative charge of the incoming ions. The surface will acquire a positive voltage of only a few volts.

Most of the existing ion beam implanter machines are using BF_3 gas to form positive boron ions. BF_3 is a very toxic gas and has many components in the extracted ion beam. This is why an alternative method of negative boron ion production has been researched by several groups.

An elegant way of producing negative ions is through the surface sputtering process described in section 3.3.2. Several RF- type surface sputtering ion sources with a cesiated sputtering target/converter capable of producing negative boron ions have been constructed in the past [51, 52]. In these ion sources an RF antenna is immersed in the ion source chamber and forms the background plasma from argon or xenon gas. A cesium oven is connected to the ion source and constant feed of cesium vapor is fed into the source. A maximum current of 1 mA of B_2^- from a 10 mm diameter extraction aperture was reported in reference 52. One major drawback in all of the constructed sources is that they are relying on cesium to increase the negative ion yields to commercially usable levels. Cesium is a conducting material, which will diffuse everywhere and condense to any cold surface. This will lead into coating of insulators in the ion accelerator system, which will cause voltage breakdowns and cause interruptions in the implanter machine operation. As a part of this thesis, two non-cesiated RF type sputter sources were constructed and tested.

7.2 Multicusp- type sputtering ion source with internal antenna

7.2.1 Experimental setup

A proof of principle measurement was set up in the first stage of the negative boron experiment. An existing multicusp ion source was modified for the experiment. Figure 67 shows a schematic diagram of the ion source. The source chamber was 25 cm in diameter and 12.5 cm in length and was surrounded by 10 rows of permanent magnets in a multicusp arrangement. 13.56 MHz RF amplifier was used to form the plasma by coupling the RF field into an antenna inside the plasma chamber. A 20 mm diameter Lanthanum Hexaboride (LaB_6) converter/sputter target was immersed in the plasma through the back plate. LaB_6 provides the source of boron and the low work function (2.36 eV) surface for formation of negative ions. The plasma facing edge of the LaB_6 was machined into a spherical surface with a 79 mm radius of curvature to focus the ion beam. The converter was attached into a water cooled copper stand and the whole converter insert was surrounded by a quartz tube that left only the spherical surface of the LaB_6 exposed to plasma.

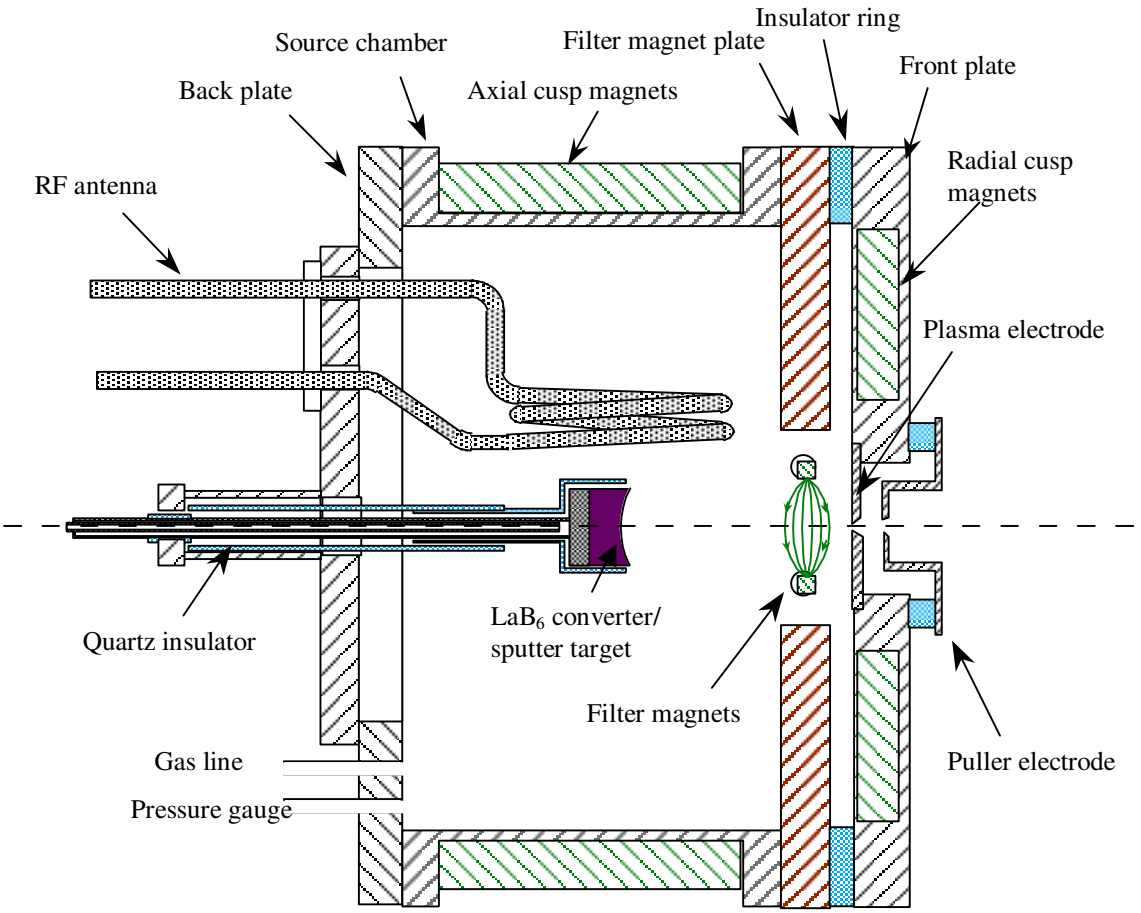

***Figure 67**. A schematic diagram of the 25 cm diameter, 12.5 cm long multicusp ion source with a movable LaB6 converter/sputter target.*

A filter magnet plate with two rods containing permanent magnets was installed in front of the extraction aperture. The created magnetic dipole field will decrease the extracted volume electron current from the source and also deflected the secondary electrons emitted from the converter surface. The front plate was insulated from the source to allow a bias voltage to be applied on it. Radial cusp magnets were embedded in the front plate to improve the plasma confinement. An exchangeable plasma electrode disc with a 3 mm diameter aperture was attached to the front plate. An insulated puller electrode with a 4.5 mm diameter aperture and a 3 mm gap to the plasma electrode was operated either electrically grounded or floating.

Figure 68 shows the photographs of the ion source back plate with a porcelain coated RF antenna and the LaB_6 converter installed and the ion source chamber.

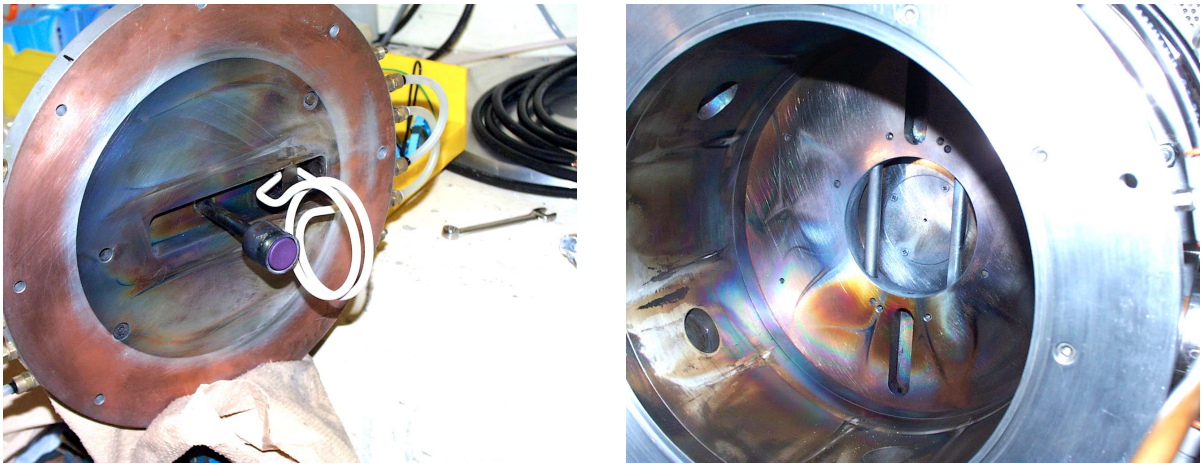

(a) *(b)*

***Figure 68**. (a) back plate with the RF antenna and the LaB6 converter, (b) ion source chamber with the filter magnet rods and the extraction aperture visible*

The extracted ion beam is mass analyzed using a magnetic deflection spectrometer and the ion beam current is measured with a faraday cup. Figure 69 shows a schematic diagram of the ion source and the mass spectrometer setup.

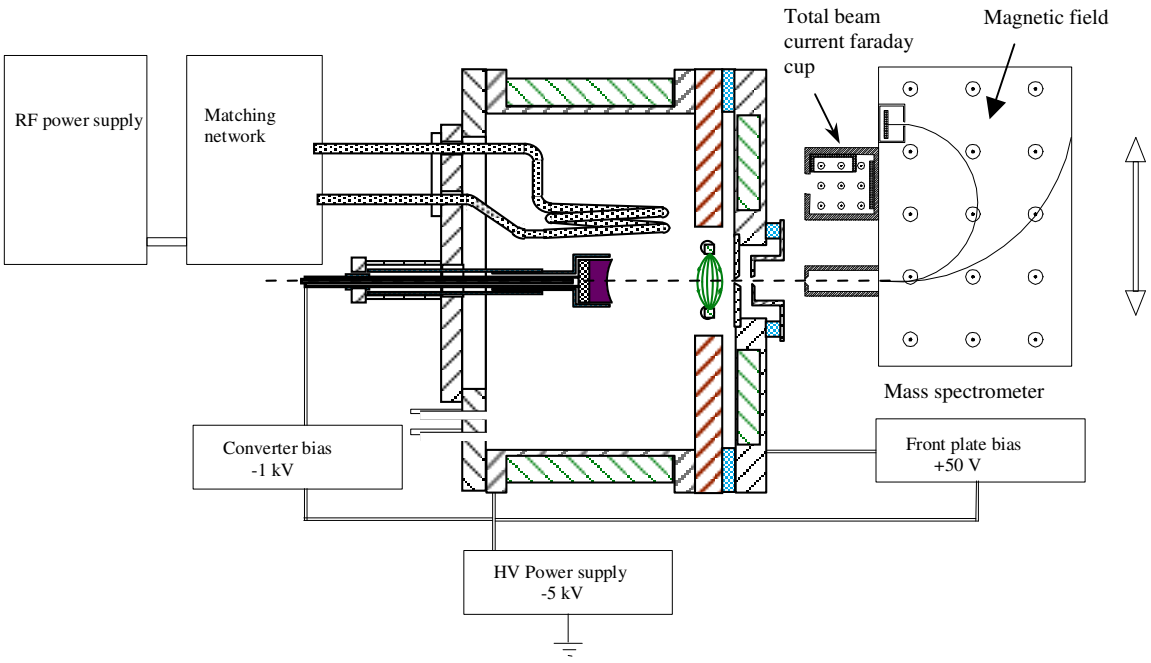

***Figure 69**. A schematic diagram of the ion source and the mass spectrometer.*

After passing through the puller electrode the beam enters the mass spectrometer through a slit. The spectrometer coil currents and thus the magnetic field is varied, which changes the beam trajectory radius inside the analyzer. The faraday cup with an entrance collimator reads the ion current of each mass component one by one as a function of the spectrometer magnetic field.

The whole spectrometer body is moveable, and a total ion current faraday cup is installed so that the mass scans and the ion current measurement can be performed without interrupting the source operation. The faraday cup has a transverse magnetic field and two separate beam dumps to enable the separation and measurement of the beam electron and ion currents.

7.2.2 Extraction simulations

The ion extraction was simulated by using the PBGUNS simulation program. The geometry was simulated for both volume and surface extraction of ions.

In figure 70, simulations of volume produced positive argon and surface produced negative boron extraction are presented. The target plane in both cases is located at the entrance of the faraday cup, which is an aperture of 10 mm diameter. Also the emittance patterns at the end plane for both cases are presented.

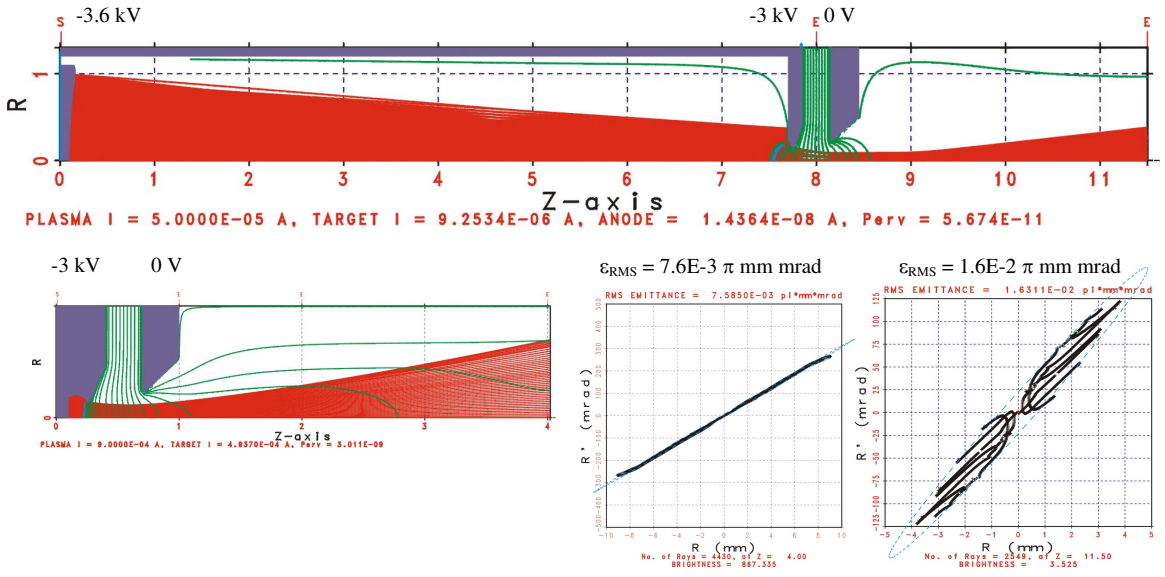

***Figure 70**. PBGUNS simulations of sputtering/surface extraction of B_2^- (top), volume extraction of Ar^+ (bottom left), emittance pattern of Ar^+ (bottom middle) and B_2^- (bottom right).*

The current density values used in the simulations of figure 70 were *7 mA/cm*^{2} for Ar^+ and *0.15 mA/cm*^{2} for B_2^-. The converter voltage was -600 V in the sputtering source. The emittance patterns display the effect of the higher transverse energy gained by the ions in the case of sputtering/surface extraction. The emittance of the sputtered ion beam is about a factor of two higher than the emittance of the volume produced ions.

A new faraday cup was designed with the help of KOBRA3-INP 3D-simulation code. Figure 71 shows the new magnetic field profile at the middle plane of the faraday cup and the KOBRA simulation with 0.5 – 3 keV electrons and boron ions injected into the cup.

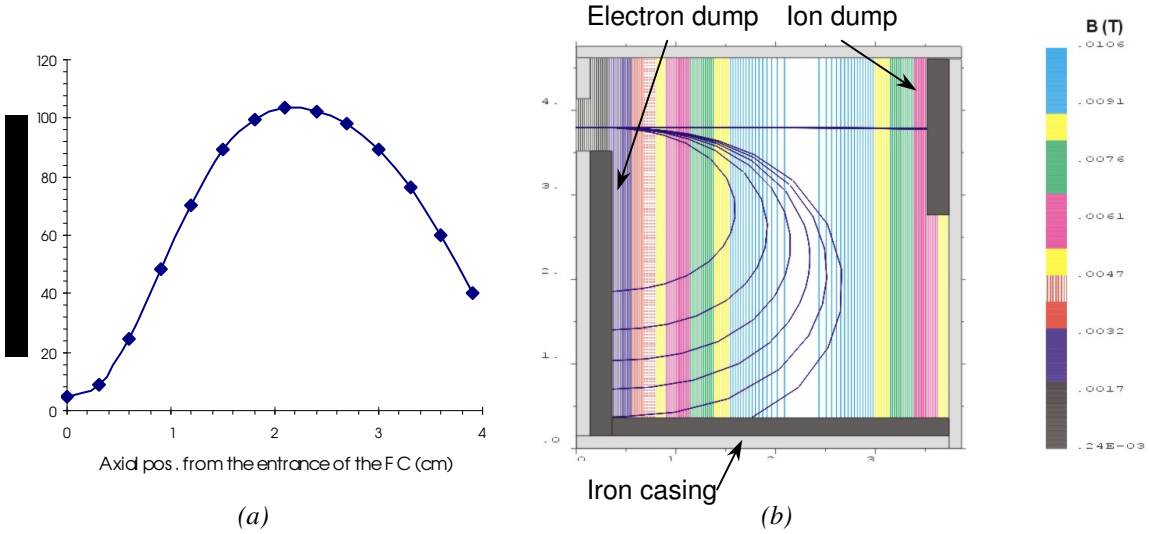

Figure 71. *(a) the measured transverse magnetic field at the center plane of the new FC, (b) KOBRA3-INP simulation of the FC with 0.5 – 3 keV electrons and* B_2^- *-ions. The FC dimensions are in cm.*

The ion dump was biased to a positive voltage with respect to the rest of the cup to prevent the escape of secondary electrons. This is important for accurate current measurements, because if the secondary electrons are escaping from the FC, the current readings from the cup will be too high for positive ions and too low for negative ions.

Figure 72 shows the effect of the FC bias on the faraday cup current in the case of a negative ion beam.

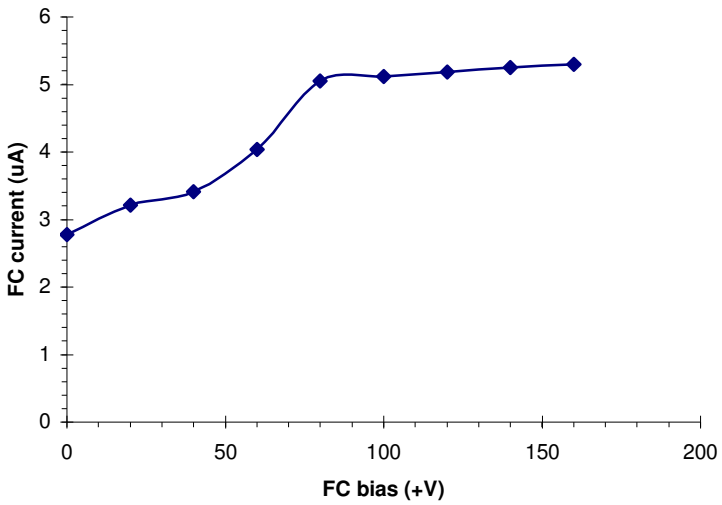

***Figure 72**. Effect of the FC ion dump bias voltage on the measured negative ion current.*

The result in figure 72 shows that a positive voltage of +100 V is sufficient to prevent any escape of secondary electrons. The ion current almost doubles when the bias voltage is increased from 0 to +100 V.

7.2.3 Measurements with Ar^+

The measurements were started by extracting positive argon ions from the volume plasma. Figure 73 shows a positive argon spectrum at 1.0 kW RF power, 4 kV extraction voltage and 5 mTorr source pressure. The single Ar^+ peak is accompanied by minute amounts of impurities, like carbon and nitrogen.

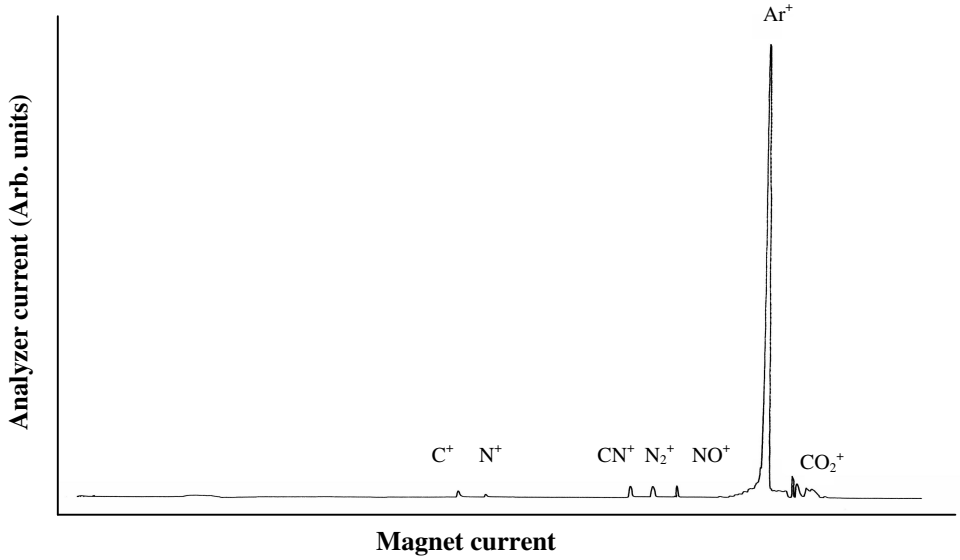

***Figure 73**. Ar^+ mass spectrum at 1 kW of RF power and 4 mTorr source pressure.*

Figure 74 shows the measured Ar^+ current extracted from a 3 mm diameter aperture at 1.0 kW RF power and 4 mTorr source pressure.

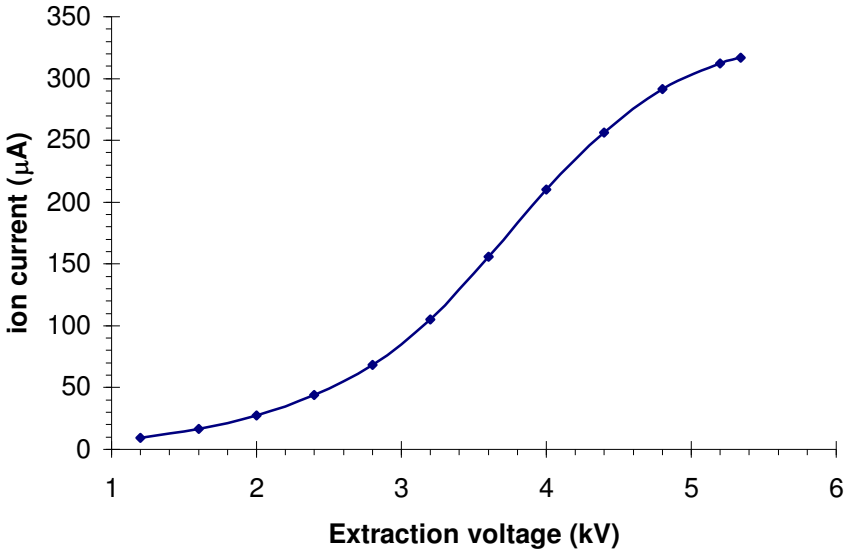

***Figure 74**. Ar^+- current at 1 kW of RF power and 4 mTorr source pressure.*

The maximum ion current in figure 74 corresponds to about 4 mA/cm^2 current density, which is about a factor of 3 to 5 lower than the measured O^+ and Cl^+ ion current densities from the smaller 10 cm diameter multicusp source used in the negative chlorine experiment that was described earlier. The big difference in the current densities, despite the mass and the first ionization potentials of Cl, O and Ar are fairly similar, can be explained by the much lower power density and thus plasma density in the bigger sputter ion source. It must also be noted that the sputtering ion source was optimized for surface production of ions.

7.2.4 Negative ion measurements with LaB_6 sputtering target

The negative ion measurements were started by changing the extraction voltage supply to a negative one. No negative ions were seen in a volume argon spectrum (within the accuracy of the spectrometer) indicating a clean argon plasma.

When the converter was biased to a few hundred volts positive potential, a myriad of peaks appeared in the spectrum. Figure 75 shows the mass spectrum of surface extracted ions from argon plasma at 1.0 kW of RF power, 5 mTorr of source pressure and -600 V converter bias.

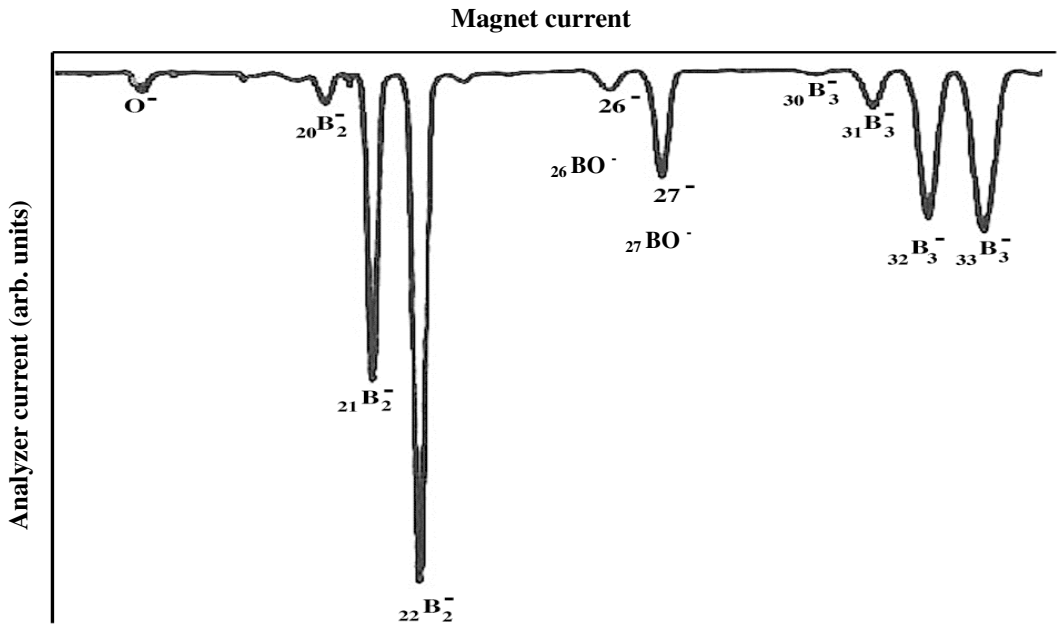

***Figure 75**. Mass spectrum from LaB_6 converter, argon plasma, 1.0 kW RF power, 1 kV extraction voltage, 5 mTorr source pressure and -600 V converter bias.*

No atomic negative boron ions were seen in any spectrums within the accuracy of the spectrometer. A small peak of oxygen was present. Oxygen is reacting with the converter material and is released by the argon ion bombardment. Most striking feature is the two clusters corresponding to negative B_2 and B_3 ions. Boron has two isotopes with mass numbers 10 and 11 with abundances of 20 % and 80 %, respectively. The relative heights of the negative boron peaks in figure 75 match well to abundances of boron isotopes. Only the $_{32}B_3^-$- peak is slightly higher because O_2^- has the same mass number, 32, and is contributing to the peak height. Two BO^-- peaks can also be seen in the spectrum.

The relative heights of the peaks stayed the same when the RF power and the converter bias voltage were varied. About 64 % of the beam current was B_2^-, 26 % B_3^- and 10 % BO^-

When the converter voltage was turned off, no negative ions could be detected in the spectrum within the precision of the spectrometer. This is an indication that all the negative ions are produced in the LaB_6 converter surface by sputtering and surface ionization process.

Figure 76 shows the negative ion spectrum measured with xenon plasma.

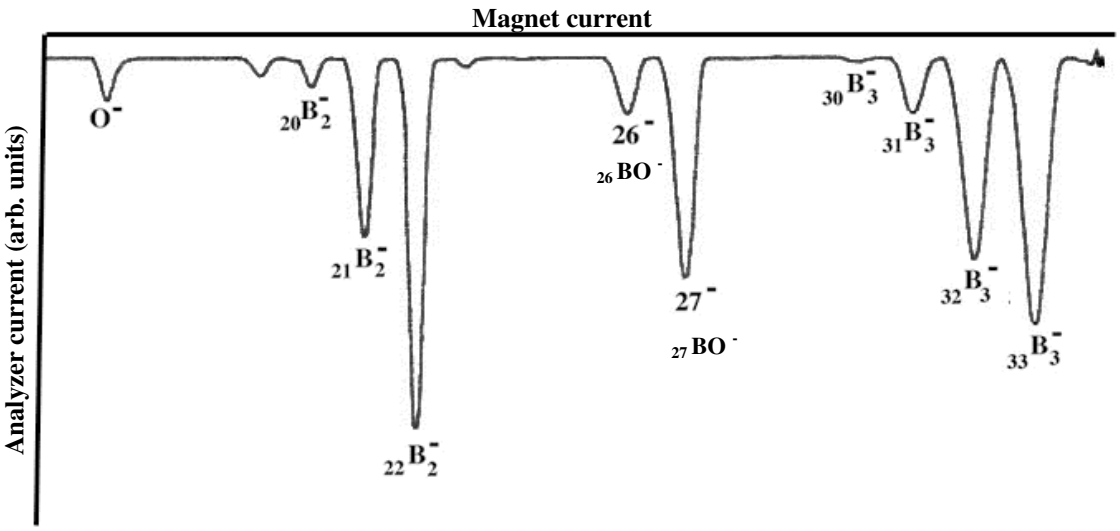

Figure 76. *Mass spectrum from LaB_6 converter, xenon plasma, 1.0 kW RF power, 1 kV extraction voltage, 5 mTorr source pressure and -600 V converter bias.*

The negative ion spectrum obtained from xenon plasma is slightly different from the argon spectrum. The B_3^- and BO^- peaks are relatively higher than in the case of argon, which is due to the heavier mass of xenon compared to argon. This means that xenon ions can sputter heavier particles more easily than argon. The beam fractions were 41 % of B_2^- 39 % of B_3^- and 20 % of BO^-.

In figure 77, the measured B_2^- and B_3^- currents are plotted as a function of RF power for argon and xenon plasma.

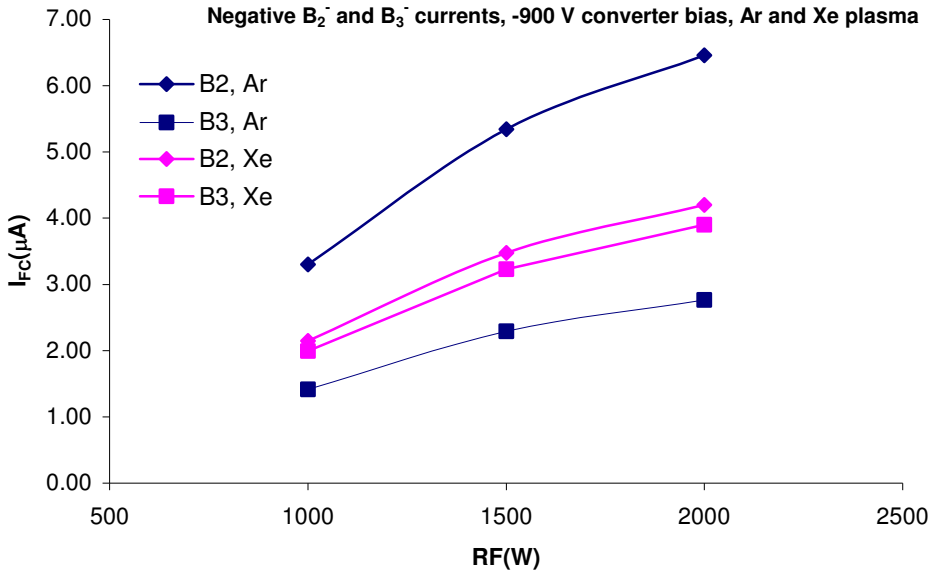

Figure 77. *B_2^- and B_3^- ion currents as a function of RF power at -900 V converter bias, 1 kV extraction voltage and 4 mTorr source pressure.*

The ion currents in figure 77 are saturating slightly at higher RF power. This was due to the fact that the RF antenna had a stainless-steel tube with rather high resistance as conductor and it started to heat up at higher power, as the ohmic losses got bigger.

Figure 78 shows the measured B_2^- current with argon plasma as a function of converter voltage.

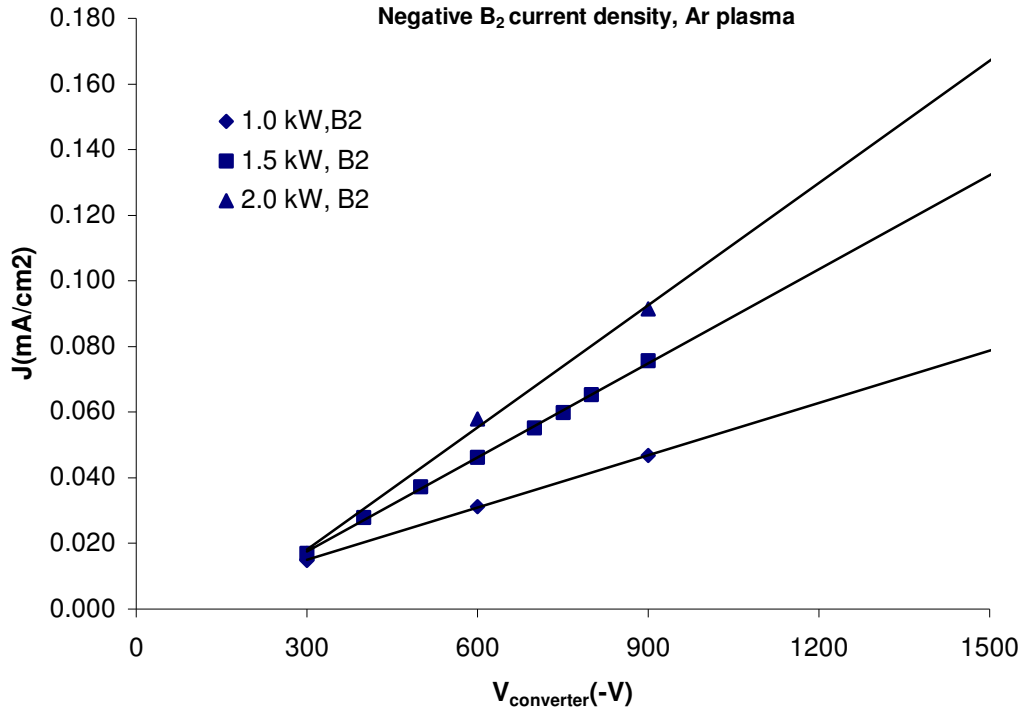

***Figure 78**. B_2^- current density as a function of the converter bias at 1.0 kW, 1.5 kW and 2.0 kW RF power.*

Figure 78 shows that the ion current increased linearly with the converter voltage. The linear behavior was seen with all ion components and for both argon and xenon plasma at all source pressure and RF power values. This shows that the sputtering yield of boron is increasing linearly with the increasing energy of the incoming positive ions to the converter. After the initial conditioning phase, the converter was operated at 1 kV positive bias voltage without any sparking problems.

To compare the linear relation of figure 78 to the sputtering yield calculations, a Monte Carlo simulation program TRIM [53] was used to calculate the sputtering yields of boron from LaB_6 as a function of incoming argon ion energy. The results of the simulation are plotted in figure 79.

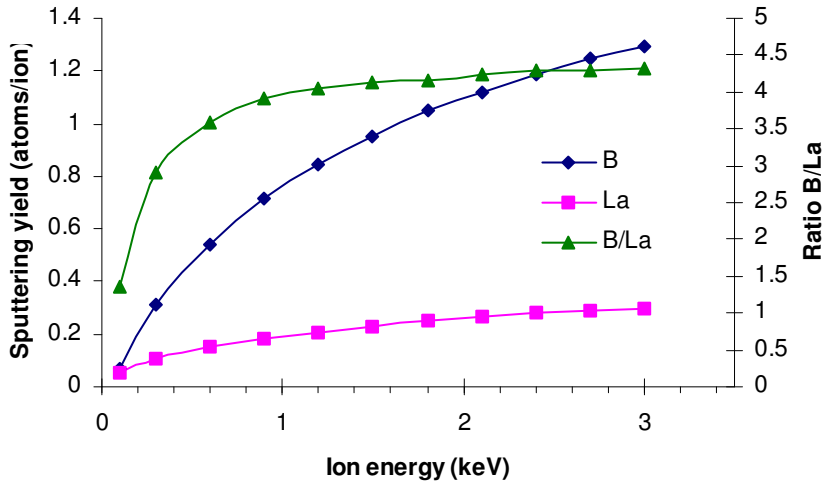

***Figure 79**. TRIM- simulation of sputtering yield of boron and lanthanum from LaB_6 as a function of incoming Ar- ion energy.*

The boron sputtering yield in figure 79 is nearly linear with the ion energy between 0.3 and 0.9 keV, which was the range of the converter voltage in figure 78. At higher ion energies the increase in sputtering yield is slower but no saturation is observed below 3 keV. The ratio B/La would indicate that more La is sputtered from the LaB_6 converter. TRIM calculation program did not take into account the emission of boron clusters, which increases the amount of sputtered boron and the B/La –ratio is likely larger than indicated in figure 79.

The effect of source gas pressure on the extracted negative ion current is plotted in figure 80. The measurement was done with an argon plasma at 1.5 kW of RF power, -400 V of converter bias and 1 kV extraction voltage from a 2 mm diameter extraction aperture. At above 8 mTorr source pressure, the converter started to spark. For this reason the measurement was done below this pressure.

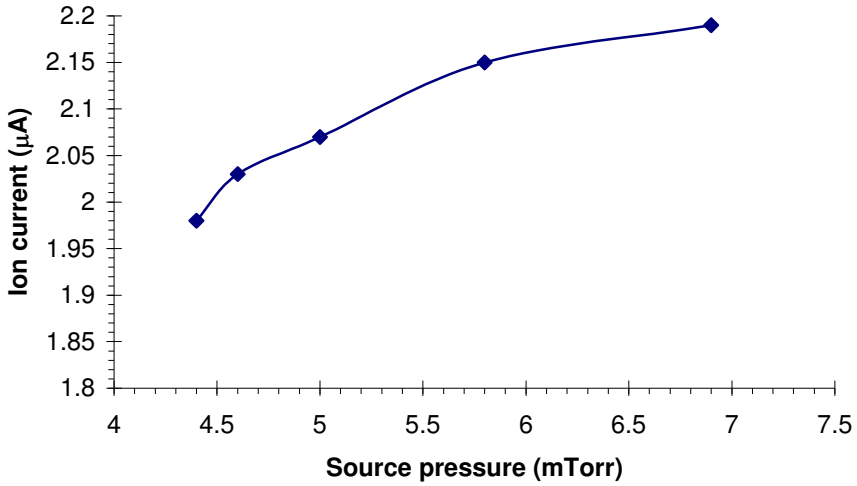

***Figure 80**. Effect of source pressure on negative ion current, Ar-plasma, 1.5 kW RF power, 1 kV extraction voltage and -400 V converter bias.*

The negative ion current was decreasing at lower source pressure, which was due to the decreasing plasma density as the source pressure went down. This could be confirmed visually by monitoring the brightness of the plasma through a quartz window that was installed in the source back plate. The plasma got dimmer with decreasing source pressure below 10 mTorr.

The effect of converter position to negative ion current is plotted in figure 81. The measurement was made at 1.2 kW RF power, 5 mTorr source pressure and 1 kV extraction voltage from a 3 mm diameter extraction aperture.

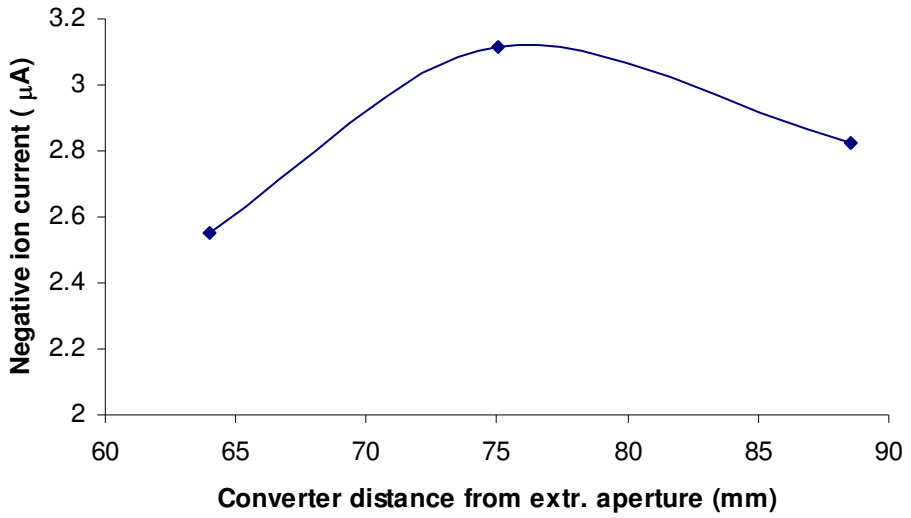

Figure 81. *Effect of converter position to extracted negative ion current.*

The ion current has a maximum when the converter is about 75 mm away from the extraction aperture. This matches quite well with the center of curvature of the converter surface.

The plasma density of the ion source could not be measured directly, but an estimate for the plasma density is given by the converter drain current. The converter current measured as a function of converter voltage is shown in figure 82. As can be seen, the leak current saturates at -20 V converter bias. The current consists of the positive ions impinging the converter surface and the secondary electrons that are emitted as a result of the positive ion bombardment. At beam energies lower than 1 keV, the secondary electron coefficient for any material by heavy ion bombardment is usually lower than 0.1, so it can be neglected [38].

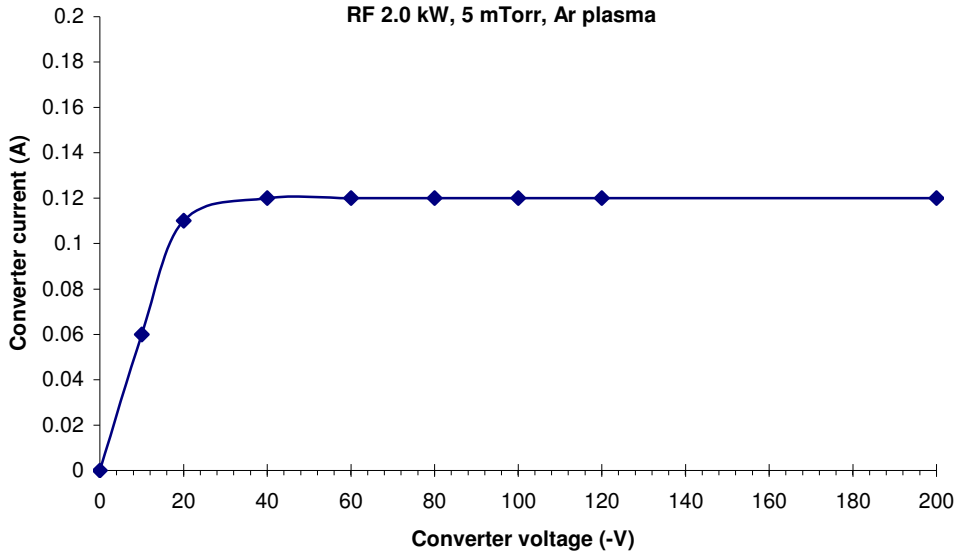

***Figure 82**. Converter current as a function of converter voltage.*

If the temperature of the argon ions is assumed to be around 1 eV, the saturation current of figure 82 would correspond to a plasma density of $9 \cdot 10^{11}$ cm^{-3}.

The negative boron production efficiency was estimated after running the source continuously at 1.6 kW of RF power and 500 V converter bias for 4 hours. Extracted total negative ion current density from a 3.45 mm diameter aperture was *85 $\mu A/cm^2$* with 64 % B_2^-, 27 % B_3^- and 9 % BO^-. The converter was weighed before and after this experiment and the mass loss was determined to be 0.24 g, of which 0.08 g is B and 0.16 g is La. The area of the converter was 3.3 cm^2. With the given information the probability for the sputtered boron atom to be carried from the converter to the plasma electrode as a part of a negative ion was determined to be about 1.3 %. In the above calculation, the negative ion current density was assumed to be the same at the converter as it was measured to be at the plasma electrode. This is a slight overestimate as the beam is focused down from the converter to the plasma electrode. This error was estimated to be balanced by the fact that the negative ion stripping losses in the plasma were neglected.

Table 1 shows a summary of the highest measured negative ion currents and current densities for argon and xenon plasma .

Table 1: Largest measured negative B_2, B_3 and BO ion currents and current densities

	Ar plasma	Xe plasma
I_{B2} (μA)	10	6.3
I_{B3} (μA)	4.2	5.9
I_{BO} (μA)	1.5	2.9
J_{B2} (μA/cm2)	138	89
J_{B3} (μA/cm2)	59	81
J_{BO} (μA/cm2	21	40.4

The beam spot on the plasma electrode was approximately 12 mm in diameter. This corresponds to about 160 μA B_2^- current. The current values of table 1 look promising and a new type of non-cesiated sputtering ion source was designed and built to further improve the extractable negative boron ion current. This new source design is presented next.

7.3 Compact sputtering ion source with external antenna

Based on the multicusp- type sputtering ion source experiment described in section 6.2, a more compact ion source was designed. The goal was to get higher power density in the ion source volume at lower RF power and to have a larger converter surface with smaller radius of curvature to increase the negative ion yield. Emphasis was put on the development of an external antenna design to minimize the loss of plasma density to the internally placed antenna and to minimize antenna lifetime issues.

7.3.1 Measurement setup

The first type of sputtering ion source that was built is shown in figure 83. The source body is 80 mm long, 75 mm inner diameter quartz tube around which the antenna loops are wrapped around. The quartz tube sits in the o-ring grooves on both the front and back plates. The back plate is suspended from the front plate by 6 insulator rods, which also take the mechanical load instead of the quartz cylinder. A 50 mm diameter LaB_6 converter is clamped to the back plate by a stainless steel collar, which is shielded from the plasma by an aluminum oxide ring.

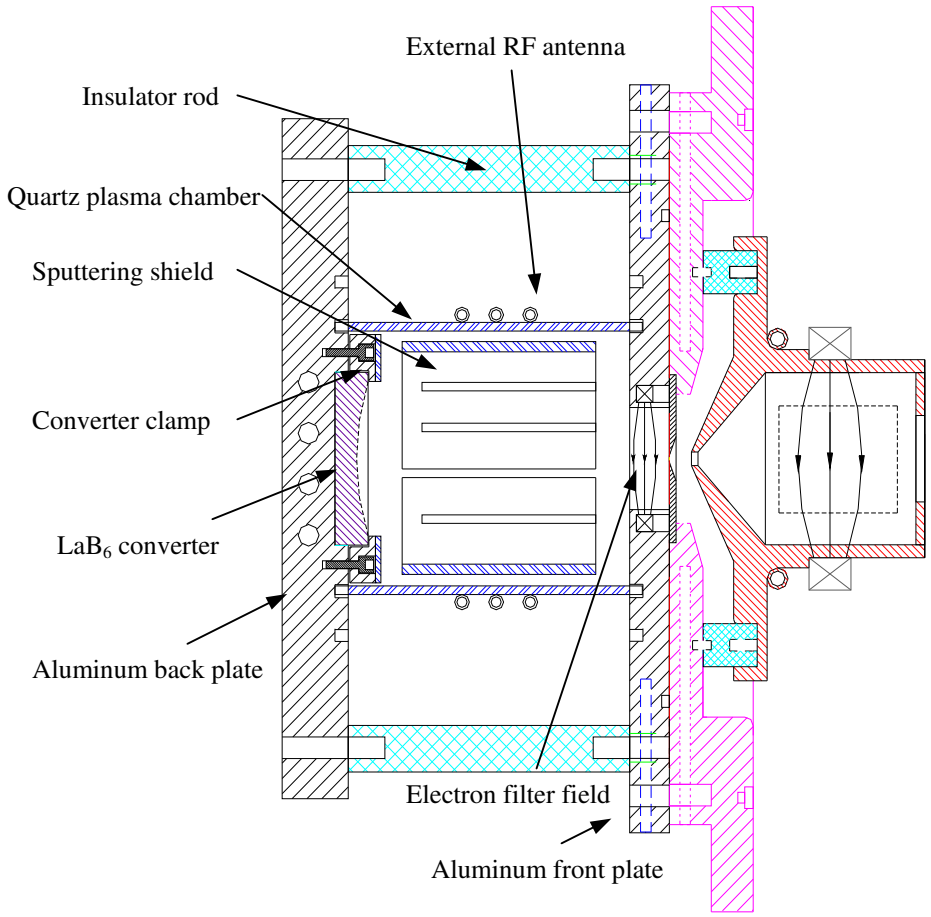

Figure 83. *New LaB_6 sputtering ion source with an external antenna.*

A 70 mm diameter quartz cylinder with 10 slots was installed inside the plasma chamber. As material is sputtered from the converter, the walls of the plasma chamber are covered by lanthanum and boron. Since lanthanum is a metal, the sputtered layer will be conducting. This would create a faraday shield between the RF antenna and the plasma volume in which the RF field will induce circular currents that will lead into the loss of RF power into the sputtered layer instead of the plasma. By installing a slotted sputtering shield with one of the slots going all the way through the length of the tube the formation of a closed conducting layer can be prevented and the RF field will not be cancelled out. The external antenna geometry combined with the sputtering shield will enable a high power, long lifetime operation of the ion source as the antenna is not exposed to the destructive environment of plasma. This is a major advantage in a commercial ion source as any unscheduled delays in the operation can cause considerable costs.

A pair of filter magnet rods were installed inside the front plate. The magnetic field turns away the secondary electrons emitted from the converter surface. The field also lowers the plasma density in front of the extraction aperture and thus lowers the extracted volume electron current.

The RF antenna coil is a simple 3 mm diameter copper tube with cooling water running inside. Two RF frequencies, 13.56 MHz and 27 MHz, have been tested. The experiment was conducted at the same test stand as the negative chlorine experiment described in chapter 5, and the same extraction and source mounting plate were used.

In figure 84 the source back plate with the LaB_6 converter and the front plate with the source chamber and the external antenna are presented.

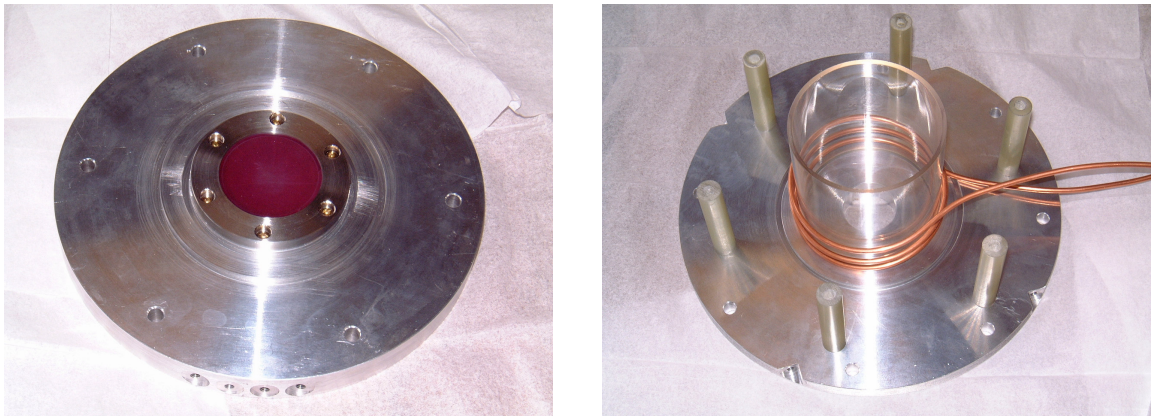

(a) *(b)*

***Figure 84**. (a) Back plate with the LaB_6 converter, (b) front plate with the quartz source chamber and the external 2.5 loop copper antenna.*

7.3.2 Extraction simulations

The plasma and the puller electrode were the same as those used in the negative chlorine experiment described in section 5. High extracted electron currents were anticipated from the dense argon plasma, as there is practically no negative ions present in the volume and the electrons fill up the negative charge density. To decrease the extracted electron current and thus the loading of the power supplies and extraction elements a new, thicker plasma electrode structure was designed. The electric field is not penetrating as deeply

into the source as in the case of a regular, thinner plasma electrode. Figure 85 shows an IGUN simulation of the plasma and extraction electrodes.

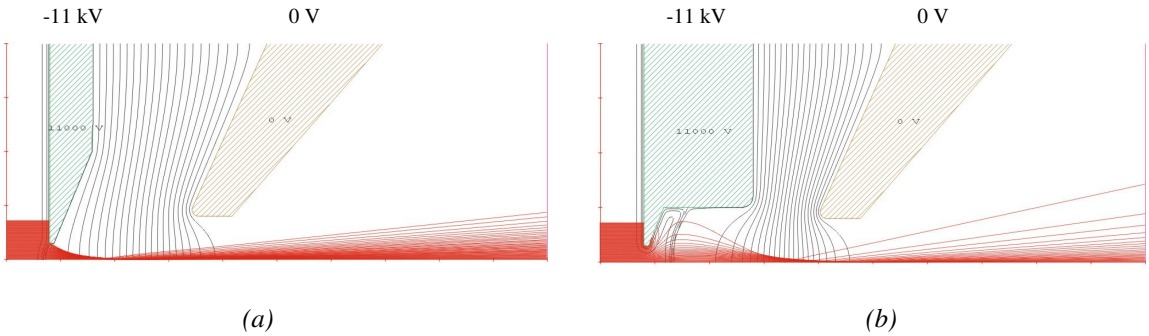

Figure 85. *IGUN simulation of the (a) regular plasma electrode and (b) thicker plasma electrode. The plasma density in both (a) and (b) was 5E10 1/cm^3, extracted electron current in (a) was 21 mA and in (b) 7 mA.*

The IGUN simulations of figure 85 show that by thickening the plasma electrode, the extracting electric field is weakened in the extraction aperture and the plasma meniscus is shifted outwards. The extracted electron current is decreased by a factor of 3.

In figure 86 the effect of the thicker plasma electrode to the surface produced ion beam is calculated using PBGUNS.

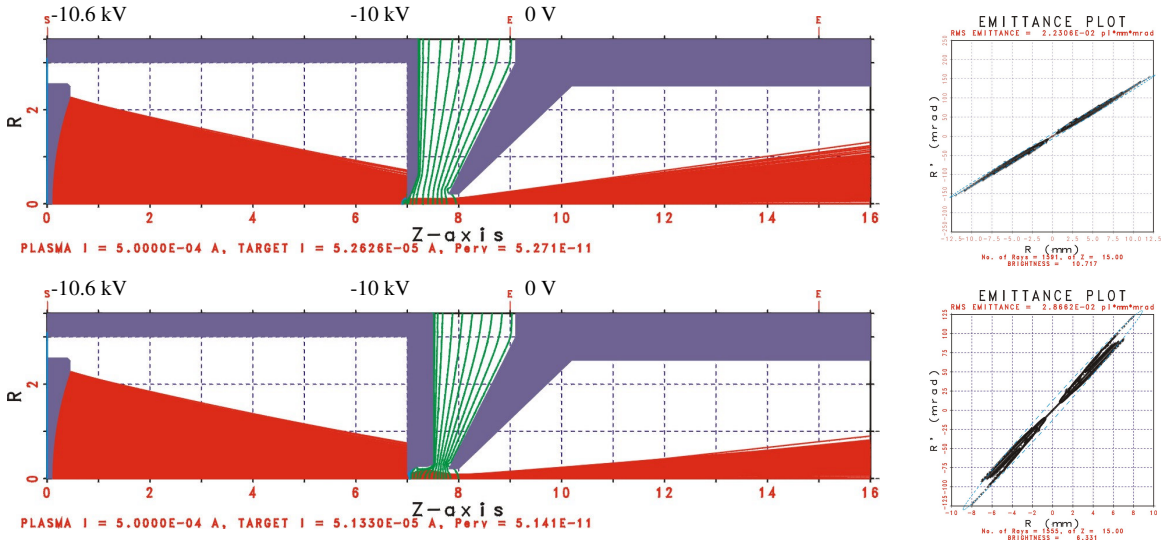

Figure 86. *PBGUNS simulation of 0.5 mA B_2^- ion beam, -600 V converter bias, 2 mm extraction aperture. Top: thin electrode, ε_{RMS} = 2.23E-2 π mm mrad. Bottom:thick electrode, ε_{RMS} = 2.87E-2 π mm mrad.*

The simulations of figure 86 show that the ion current reaching the faraday cup is very similar in both electrode geometries. The emittance is slightly larger in the case of the thicker plasma electrode, because the beam has to travel a longer distance with only the converter energy (600 eV) and is therefore blown out more by the beam space charge. Half of the ion beam current was estimated to be lost in the plasma by electron detachment collisions.

7.3.3 Measurement with Ar^+

Source operation was tested by extracting positive argon ions from the ion source volume. Figure 87 shows the measured ion species extracted from argon plasma.

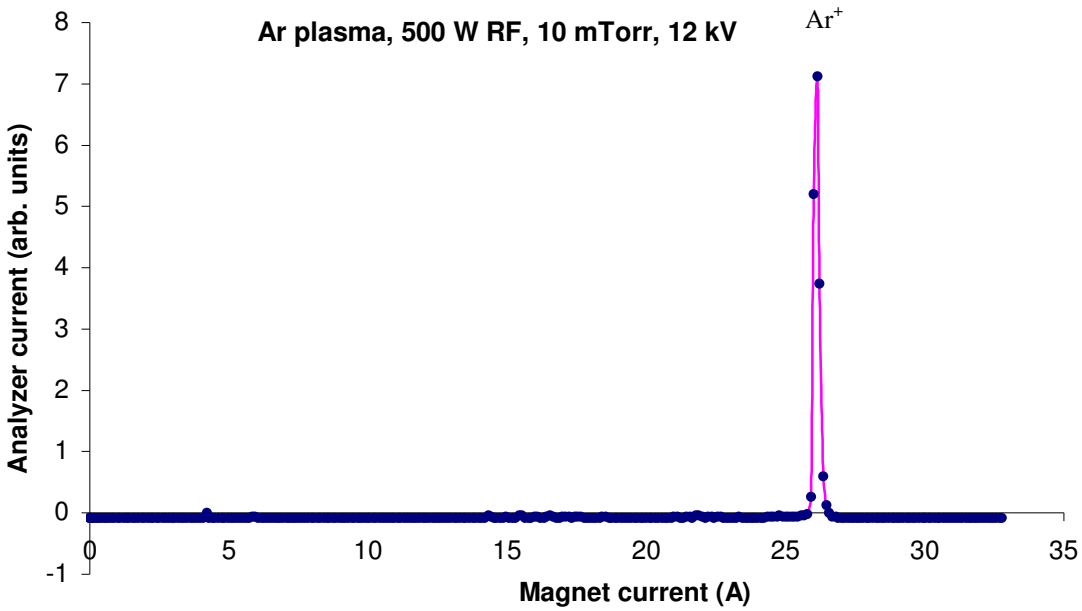

***Figure 87**. Measured mass spectrum from argon plasma at 500 W RF power, 12 kV extraction voltage and 10 mTorr source pressure.*

As figure 87 shows, the plasma was clean and only very minor amounts of impurities were seen in the beginning of the operation. After the source was operated for a while, the ion spectrum showed only the argon peak. No converter voltage was applied in the spectrum in figure 87.

The measured Ar^+-current is shown in figure 88 as a function of the extraction voltage.

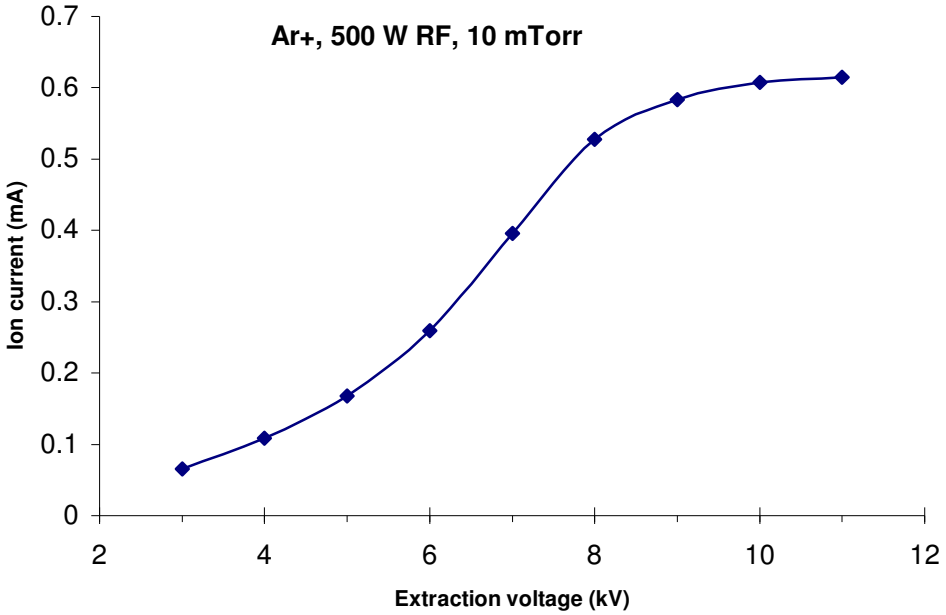

***Figure 88**. Ar^+-current as a function of extraction voltage at 500 W of RF power, 2 mm extraction aperture and 10 mTorr source pressure.*

The ion current saturates at 0.6 mA, which corresponds to a current density of 19 mA/cm^2. This is a factor of five higher than the measured Ar^+ current density in figure 74 from the large multicusp ion source presented in section 6.2. This is an indication that the small ion source with an external antenna can produce bright enough plasma for surface ionization applications at RF power levels around 1.0 kW.

7.3.4 Negative boron measurements with LaB_6 sputtering target

The negative ion measurements were started by making a comparison of the source operating parameters with and without the sputtering shield for hydrogen and argon plasmas. Before the converter was biased and any sputtering had occurred, the ion source performed identically in both cases. After the sputtered material from the converter had covered the walls of the ion source chamber the matching conditions changed slightly, but a good inductive coupling and plasma ignition was still achieved. Figure 89 shows the ion source plasma with and without the sputtering shield.

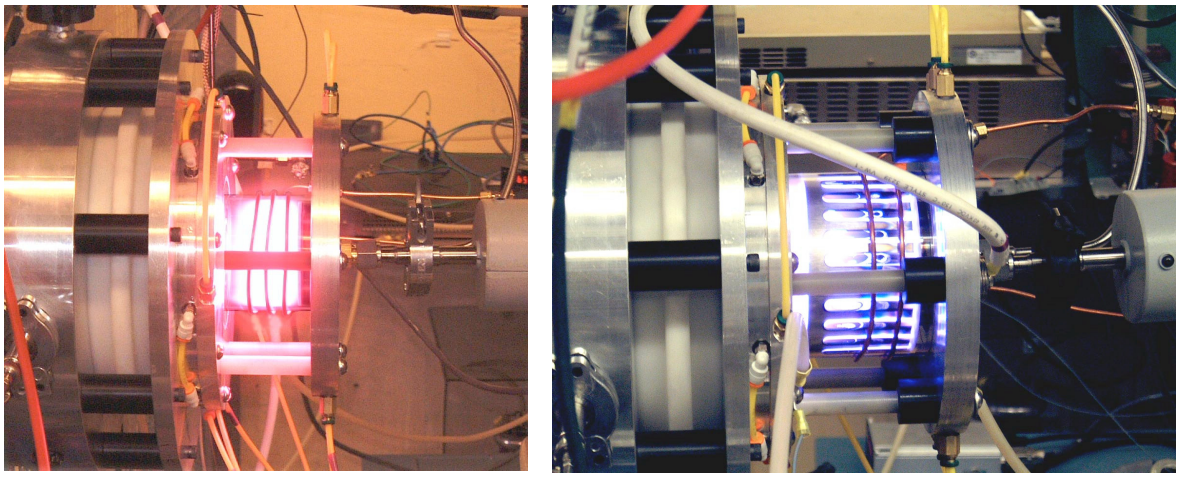

(a) *(b)*

***Figure 89**. (a) Hydrogen plasma without the sputtering shield, (b) argon plasma with the sputtering shield and sputtered material covering the interior of the plasma chamber.*

The ion source chamber length was selected so that the distance from the converter surface to the extraction aperture was 75 mm, which matches the radius of curvature of the converter. The sputtering shield was kept in the source for all measurements. Figure 90 shows a negative ion spectrum from argon plasma at 300 W RF power, 8 mTorr source pressure, 8 kV extraction voltage and -400 V converter bias.

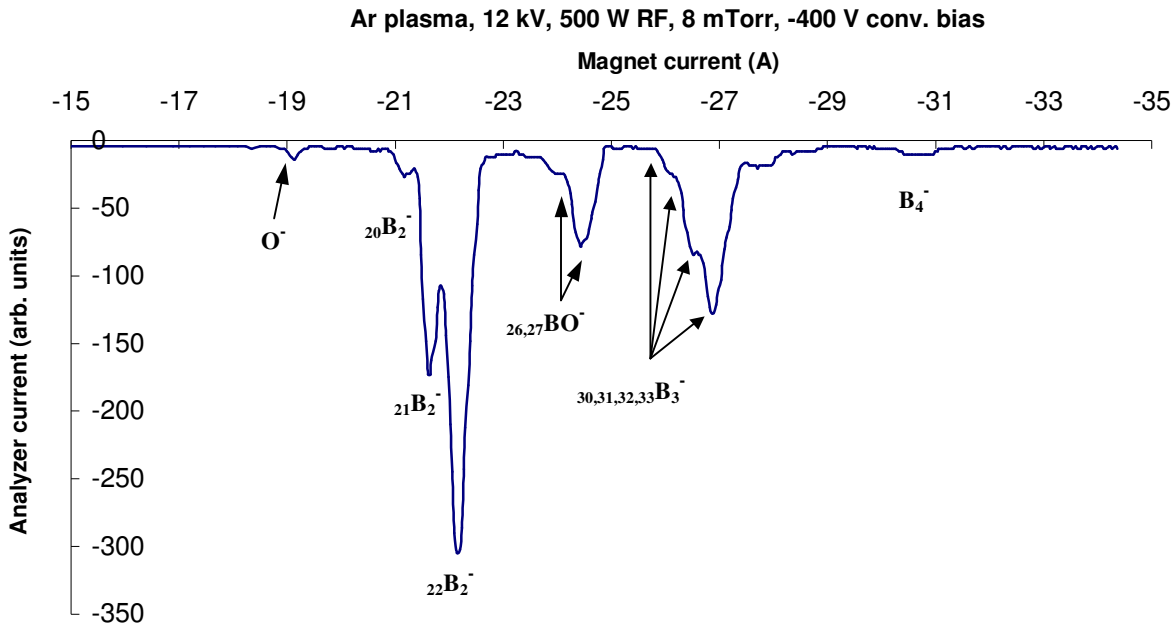

***Figure 90**. Negative ion spectrum from new LaB_6 converter source.*

The spectrum in figure 90 is very similar to the one measured with the larger multicusp sputtering source, which is shown in figure 75. The only difference was that a small, broad peak appeared around mass numbers 42 – 44. This could be negative B_4-ion cluster, but the resolution of the spectrometer was not good enough to confirm this. The lower mass resolution of the spectrometer in comparison to the one used with the multicusp sputtering source is probably due to ion optics. The beam is spreading too much before the dipole magnet and thus the different mass components are overlapping. To fix this problem a collimating aperture should be installed in front of the dipole magnet to define a smaller ion beam size.

The beam fractions stayed the same at different RF power levels and converter voltages. About 62 % of the beam was determined to be B_2^-, 27 % was B_3^-, 10 % was BO^- and 1 % O^-. This is very similar to the beam fractions measured with the large multicusp sputtering source described in section 6.2. Figure 91 shows the measured B_2^- ion current measured with the new sputtering ion source at 300, 500 and 800 W RF power at 10 mTorr source pressure. The B_2^- ion currents measured with the multicusp sputtering source are also plotted as a reference.

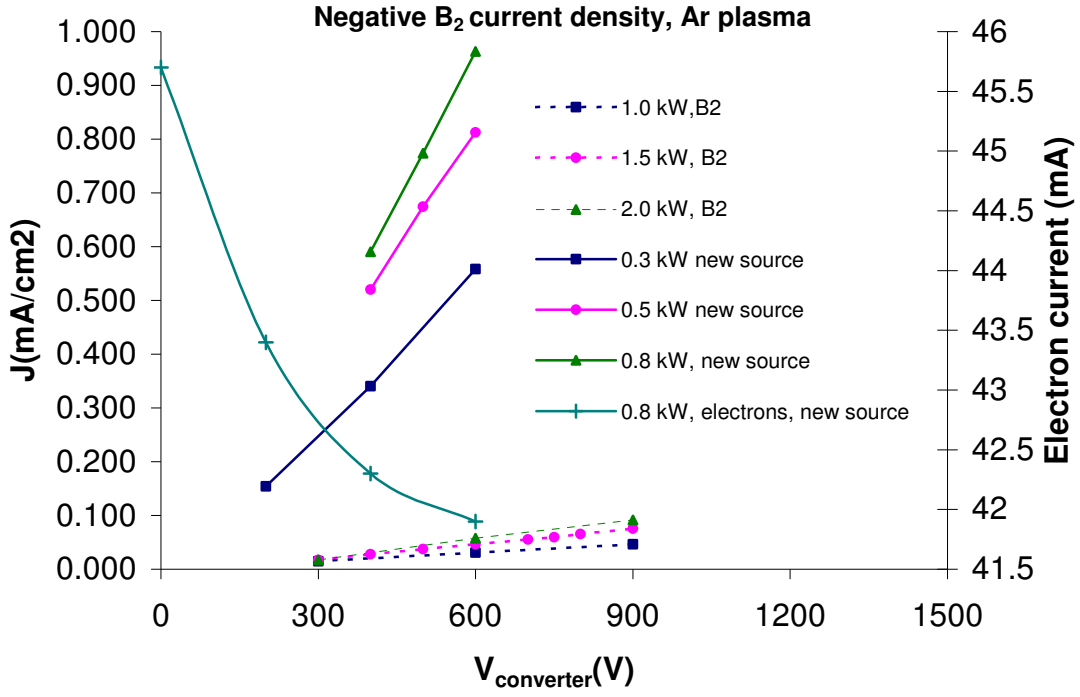

***Figure 91**. The B_2^- current density as a function of the RF power measured with the new sputtering ion source with external antenna and the large multicusp sputtering source. Extracted electron current for the new source at 0.8 kW is also plotted.*

The maximum achieved B_2^- current density with the new sputtering ion source was about 1 mA/cm^2 at 800 W of RF power, 10 mTorr source pressure and –600 V converter bias. The beam spot diameter on the plasma electrode was about 15 mm. If the current density in the beam spot is assumed to be nearly uniform the corresponding total B_2^- current at the plasma electrode plane is 1.8 mA. These current values are very similar to reported B_2^- currents obtained from cesiated, internal antenna sputtering ion sources [52]. Figure 92 shows the beam spot on the plasma electrode.

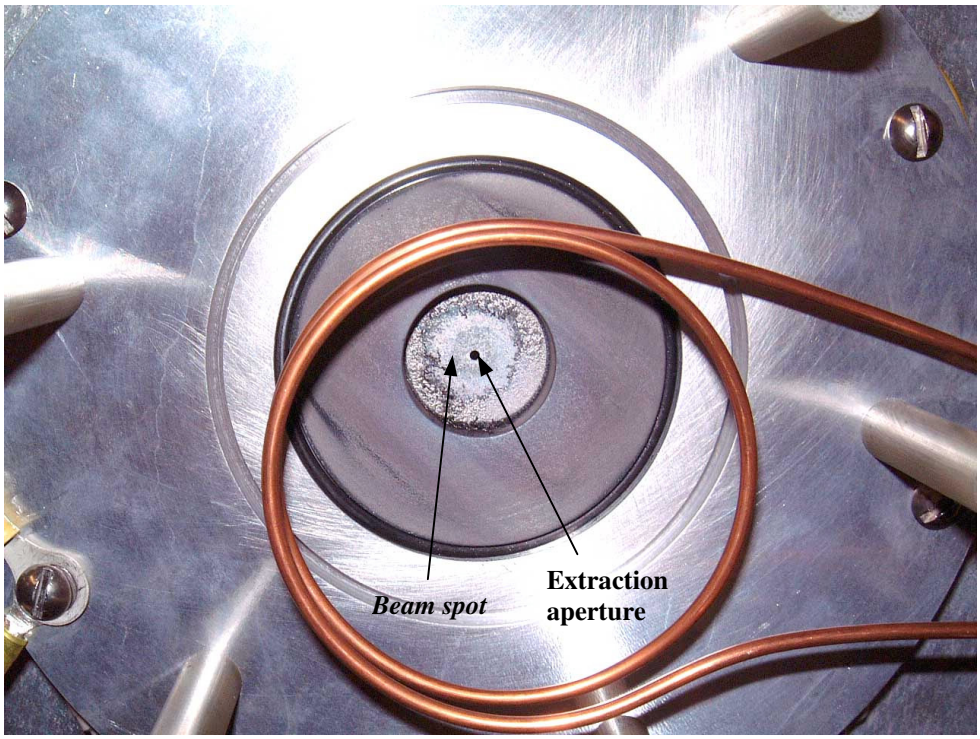

***Figure 92**. The beam spot on the plasma electrode with the 2 mm extraction aperture in the middle.*

The beam spot was shifted slightly into the upper left direction in figure 92. This is due to the electron filter magnetic field.

At higher RF power the source started to heat up and out-gasing from the o-rings started to contaminate the plasma. At converter voltages higher than -600 V the plasma became unstable. This is probably due to the fact that the large converter pulls very large percentage of the plasma ions into itself and it becomes hard to maintain enough positive charge to sustain a stable plasma. To overcome this problem a slightly larger ion source chamber should be built. This would increase the number of plasma particles and enable one to operate with higher converter bias voltages without disrupting the plasma.

In figure 93 the converter leak current is shown as a function of the RF power.

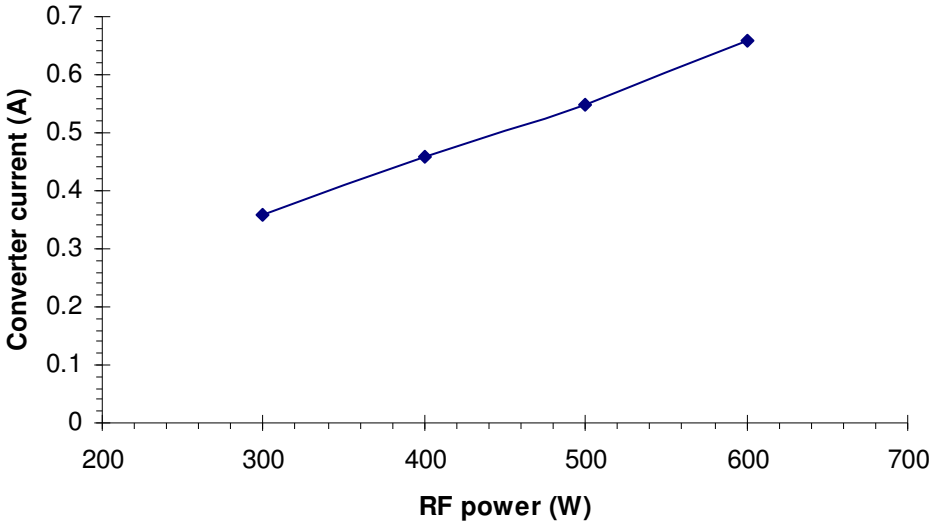

***Figure 93**. The LaB_6 converter saturation leak current as a function of the RF power.*

The power supply drain current was increasing linearly with the RF power. In table 2, the maximum extracted B_2^- current, converter leak current and the converter area for the multicusp sputtering source described in section 6.2 and the new, external antenna source are compared.

***Table 2.** The B_2^- ion current, converter leak current and converter area comparison for the two different sputtering sources used in the measurements.*

	Multicusp source (2 kW RF power)	External antenna source (800 W RF power)
Converter area (cm^2)	3.4 cm^2	16.5 cm^2
Converter current (A)	0.12	0.85
Extracted B_2^- current density (mA/cm^2)	0.14	1

The area of the new converter was a factor of five larger than the area of the old one. The ratio of the external antenna and multicusp source converter currents and ion currents was about seven. These values were measured at 2.0 kW of RF power and –900 V converter bias for the multicusp source and 800 W of RF power and –600 V of converter bias for

the external antenna source. From table 2 it can be seen that far less RF power was needed to achieve similar plasma density in the external antenna source. The fact that the ratio of the ion currents and the converter currents were the same between the two sources, even though the measurement was done at a smaller converter bias in the external antenna source, indicates that the sputtered ion beam was more focused in the new source due to the smaller radius of curvature of the converter. It is also possible that the different antenna geometry and lower RF power in the case of the external antenna source might be less destructive for the sputtered negative ions traveling in the plasma. The source pressure was similar in both ion sources, between 5 and 15 mTorr.

In here it's appropriate to discuss the advantages of the B_2^- and B_3^- ions over the atomic boron ions. In order to decrease the feature sizes in the next generation semiconductor devices, low energy (< 1 keV) boron ion beams will be implanted to form shallow junction transistors [54]. Such low energy ion beams are hard to transport due to beam space charge effects. If the ion is molecular instead of atomic, it gets easier to transport the ion beam for the following reason. If, for example, 1 keV energy is needed for a boron atom to be implanted into a right depth in a substrate material, 2 keV energy can be used to implant B_2 ions and 3 keV energy for B_3 ions and still maintain the 1 keV kinetic energy per boron atom. This is a considerable improvement from the ion optical point of view as the space charge blow up becomes less severe at higher beam energy. Molecular ions also reduce the required ion current, as the implanted boron dose per ion is higher. Figure 94 illustrates the space charge effect in the case of 1 mA ion beam starting with 5 mm initial beam radius for 1 keV B, 2 keV B_2, 3 keV B_3 and 4 keV B_4 ion beams. Zero ion transverse temperature was assumed and the beam was parallel in the beginning of the simulation geometry.

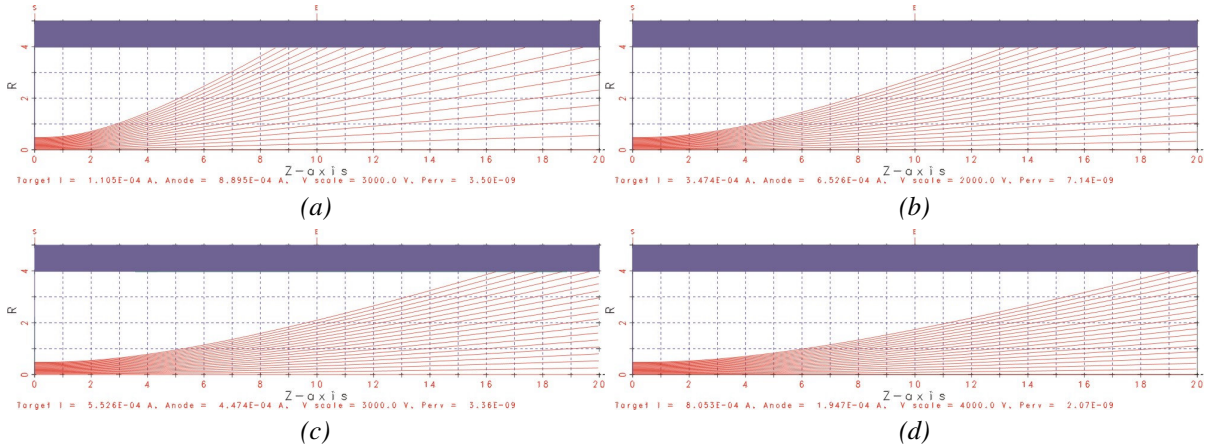

Figure 94*. The effect of the space charge on (a) 1 keV B, (b) 2 keV B_2, (c) 3 keV B_3 and (d) 4 keV B_4 ion beams with 1 mA beam current .*

7.3.5 Comparison of 13.56 MHz and 27.12 MHz RF driven plasma

In many ion source applications it's important to minimize the operating pressure of the ion source. In a sputtering type negative ion source, where the ion beam has to travel up to tens of centimeters in the plasma, it is crucial that the source operating pressure is as low as possible in order to minimize the stripping loss of the negative ions. In another emerging ion source application, neutrons are generated by 100 keV deuterium ion beam in D-D or D-T collisions (D = deuterium, T = tritium) [55]. In many cases the ion source and acceleration system has to be operated in a sealed container to prevent the release of toxic tritium into air. Low source pressure (< 1 mTorr) is required to operate this type of source at a high (> 100 kV) voltage.

The external antenna ion source described in the previous section was used to compare the plasma conditions using 13.56 MHz and 27.12 MHz RF power generators to drive the plasma. Hydrogen gas was used in the test to simulate the deuterium discharge, which is normally used in the neutron generators. Hydrogen beam spectrums and total current densities were measured as a function of source pressure and RF power to compare the relative performances of the two RF frequencies. Figure 95 shows the measured hydrogen spectrums for 13.56 MHz and 27.12 MHz RF frequencies at 1.1 kW RF power, 10 mTorr source pressure and 15 kV extraction voltage.

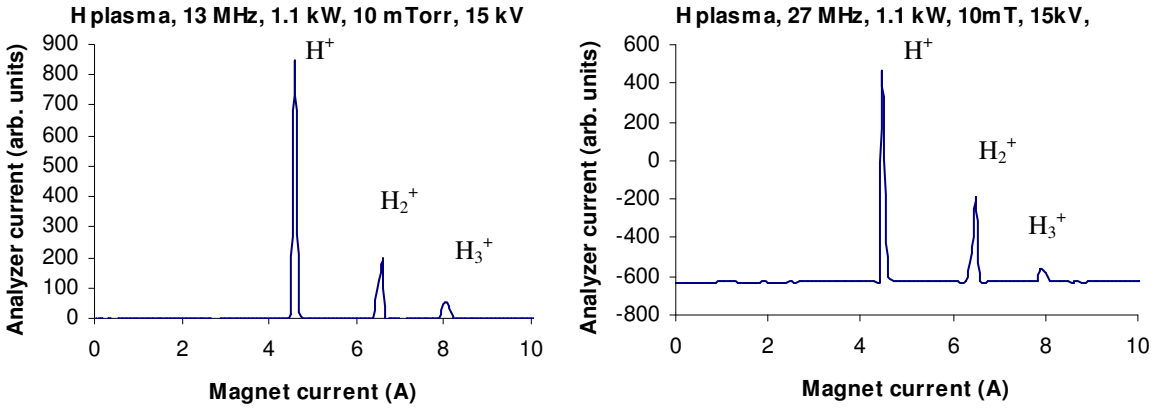

(a) *(b)*

Figure 95. *Positive hydrogen ion spectrum for (a) 13.56 MHz and (b) for 27.12 MHz.*

In neutron applications the atomic ion component is wanted. The spectrums in figure 95 show about 70 % and 78 % proton fractions for 27.12 MHz and 13.56 MHz RF frequencies, respectively. The 13.56 MHz has a slightly higher proton fraction, but generally the difference was very small between the two frequencies.

The measured total hydrogen ion currents for 13.56 MHz and 27.12 MHz are plotted as a function of the RF power in figure 96. The measurement was done at 20 mTorr source pressure and 15 kV extraction voltage.

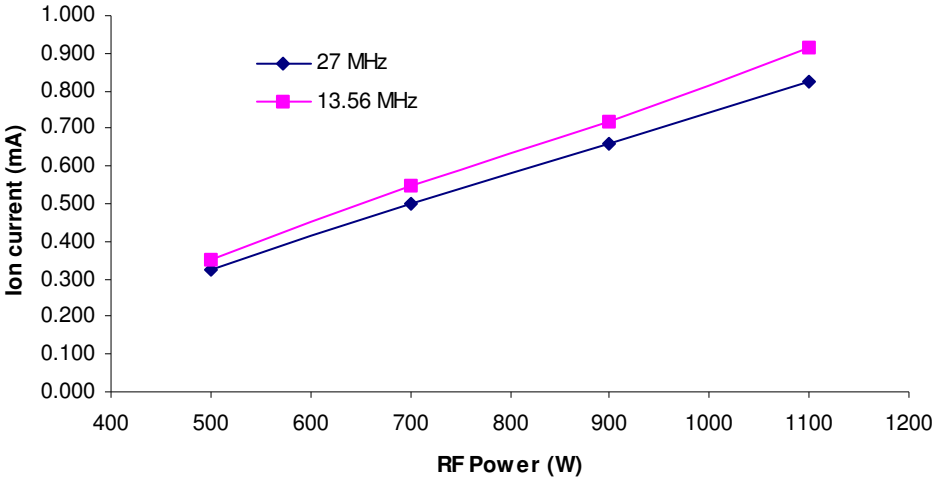

***Figure 96**. The measured total positive hydrogen current as a function of the RF power.*

The total extracted positive hydrogen current was about 10 % higher in the case of 13.56 MHz plasma. The current levels were similar with source pressures above 15 mTorr for both RF frequencies. As the source pressure was lowered, the plasma properties started to differ between 13.56 MHz and 27.12 MHz. Figure 97 shows the measured total hydrogen ion current as a function of the source pressure for the two frequencies at 1.1 kW RF power and 15 kV extraction voltage.

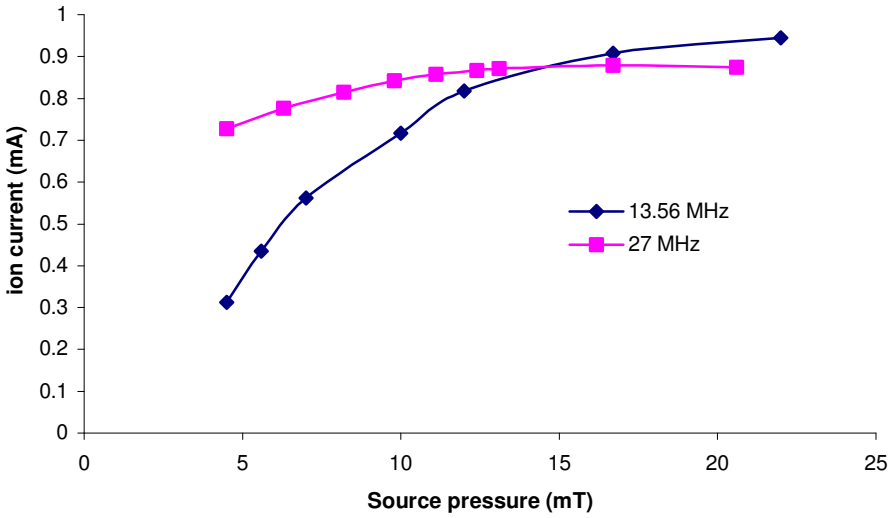

***Figure 97**. The measured total positive hydrogen current as a function of source pressure.*

As can be seen from the figure 97, the 13.56 MHz discharge started to extinct much faster than the 27.12 MHz plasma. As the source pressure was lowered from 20 mTorr to 5 mTorr, the hydrogen ion current in the 13.56 MHz operation decreased from 0.94 mA to 0.31 mA, a factor of three. For 27.12 MHz plasma, the current dropped from 0.88 mA to 0.73 mA, only about 17 %. The discharge remained stable to much lower pressure for 27.12 MHz. The ignition pressure was 100 – 150 mTorr for 13.56 MHz and 8 – 10 mTorr for 27.12 MHz.

The above mentioned results match well with the discussion in sections 2.2 and 3.1 concerning the effect of the RF frequency on plasma properties. These results show that the combination of low ignition pressure and much slower decay of plasma density with decreasing source pressure make the 27.12 MHz RF frequency a more viable driver for sealed neutron generators and negative surface ionization sources.

7.3.6 H^- measurements with the external antenna ion source

Negative hydrogen ions are needed in many applications, ranging from nuclear physics and neutron sources to medical isotope production. In all of these applications there is a need for a reliable, long-life ion source capable of producing H^- beams with intensity and energy ranging anywhere from 5 mA, 6 keV [36] to 50 mA, 65 keV [56]. Traditionally the H^- ion sources have been either filament or internal RF antenna driven multicusp sources. The filament driven sources have a shortcoming in the limited lifetime of the filament and contamination of the ion source and acceleration column by the vaporized filament material. For high power applications the internal antenna RF source has proven to be a better solution, but has also suffered from antenna lifetime issues as the plasma is very destructive environment for the antenna immersed in it. These are the reasons why a short experiment was conducted with the external antenna source presented in section 6.3 to see the viability of such a source for volume H^- production.

The ion source set up was the one presented in figure 83. Cesium getter wires were placed around the extraction aperture to provide cesium and thus improve the H^- production. The level of cesiation was monitored by reading the extracted electron current. When cesium was released from the getters, the electron current started to decrease.

Figure 98 shows the measured volume negative ion spectrum with the Cs-getters inside the source but without any visible signs of cesiation seen in the electron current. The electron current was the same as before the cesium getters were added into the source.

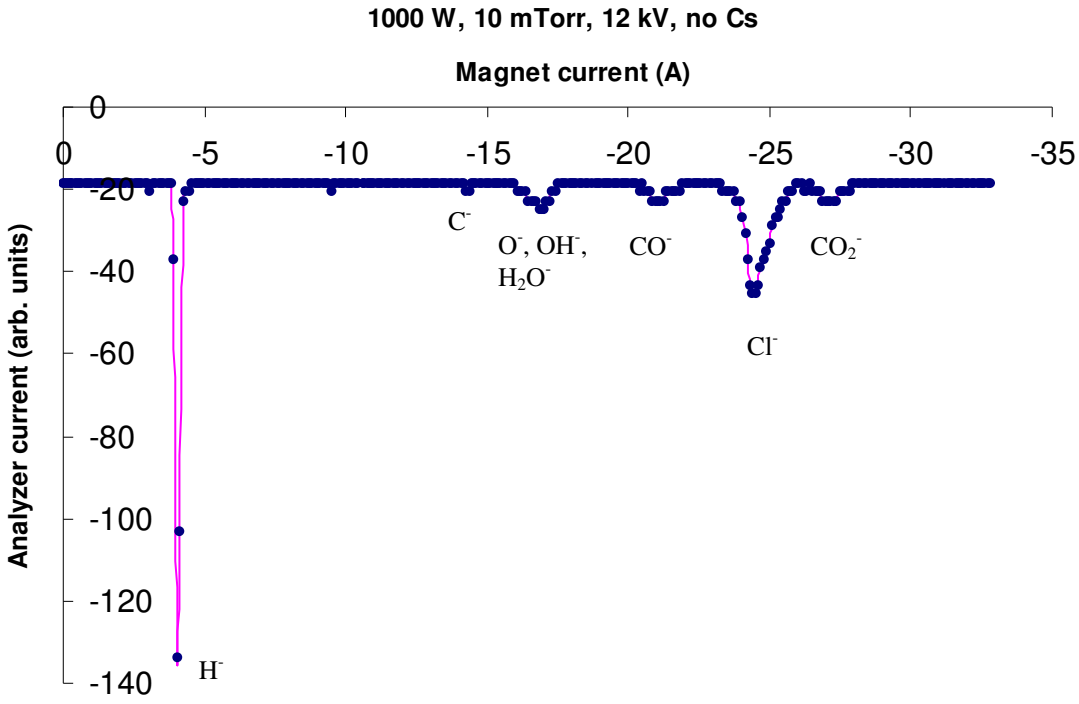

Figure 98. *The measured H^- spectrum at 1 kW of RF power, 10 mTorr source pressure, 12 kV extraction voltage and non-cesiated plasma.*

Some impurities can be seen in the spectrum. The usual oxygen and carbon compounds were accompanied by a chlorine peak, which was a surprise, since a period of time had passed from the chlorine experiments in the same test stand. After an investigation an old cesium getter wire was found among the new ones that were installed for the negative hydrogen measurement. This was one of the wires used in the chlorine experiments and had some absorbed chlorine in it and was thus replaced with a new one.

Figure 99 shows the measured H^- current as a function of extraction voltage from the non-cesiated plasma. The negative hydrogen current was around 6 μA, corresponding to a current density of 0.2 mA/cm^2.

Figure 100 shows the negative ion spectrum after the electron current started to decrease and the ion current increase as partial cesiation of the source was achieved.

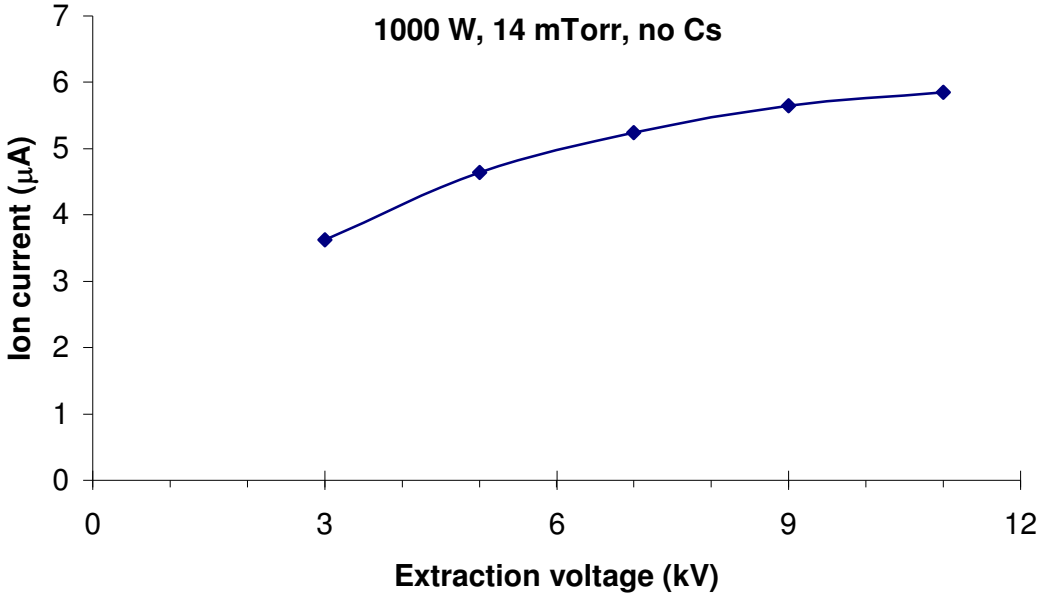

***Figure 99**. The extracted H^- current at 1.0 kW RF power, 14 mTorr source pressure, 2 mm diameter extraction aperture and non-cesiated plasma.*

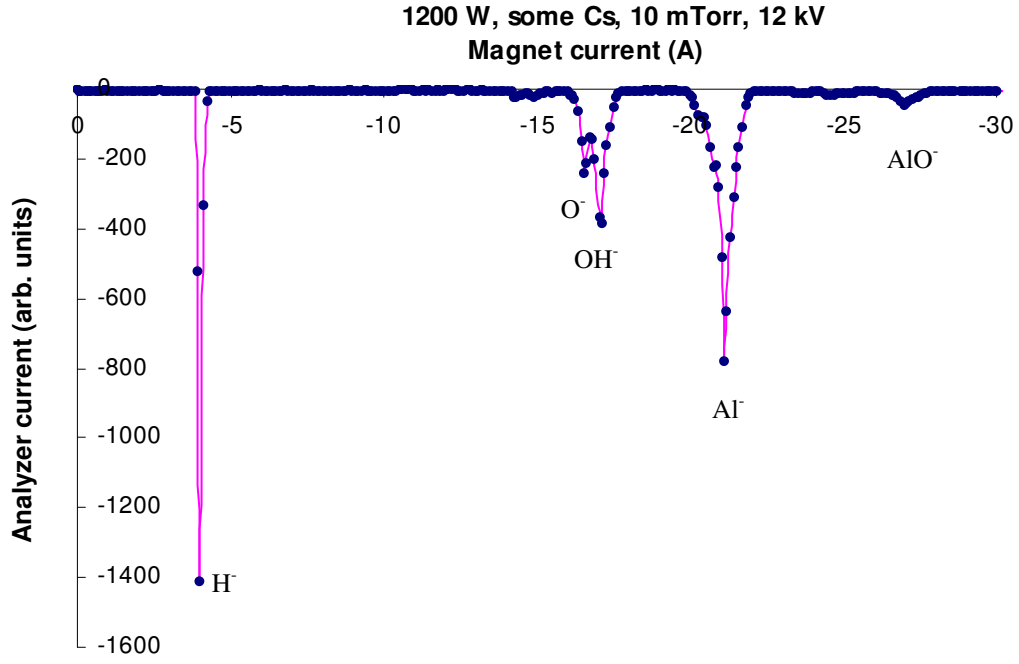

***Figure 100**. Negative volume ion spectrum taken at 1.2 kW of RF power, 10 mTorr source pressure, 12 kV extraction voltage and with some effects of cesium starting to show.*

The partly cesiated spectrum had 49 % H^-, 9 % O^-, 14 % OH^- , 27 % Al^- and 1 % AlO^-. The oxygen and aluminum impurities come from the cesium getter wires, in which the cesium is in an oxide form and is enclosed in an aluminum casing.

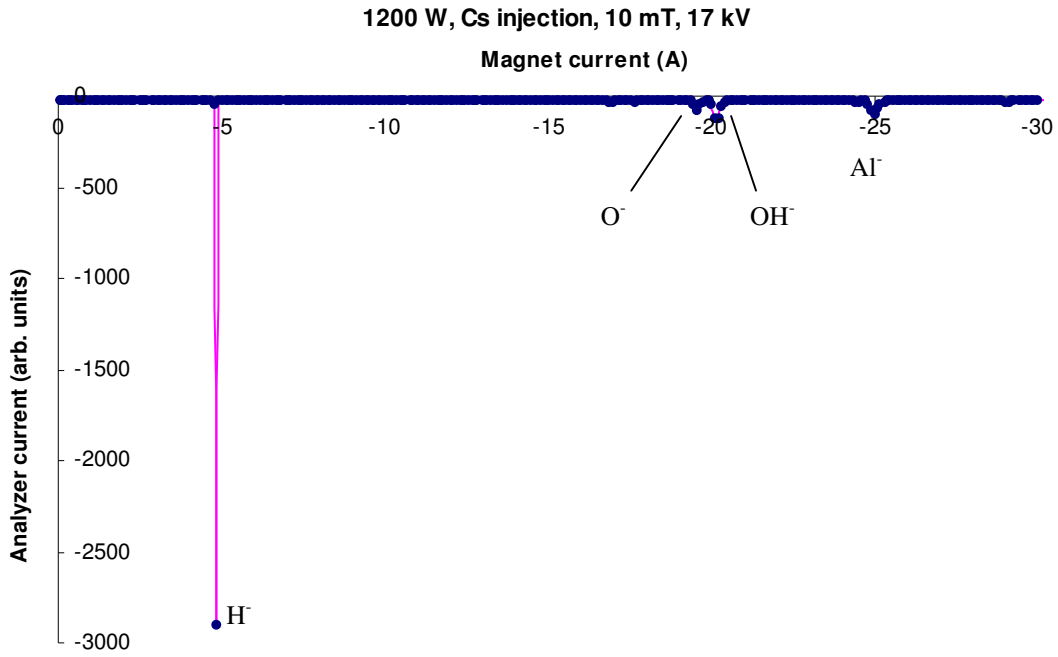

Figure 101. *Negative volume ion spectrum taken at 1.2 kW of RF power, 10 mTorr source pressure, 17 kV extraction voltage and cesiated condition of the ion source.*

Figure 101 shows a measured volume negative spectrum with optimal achieved source cesiation.

The negative ion spectrum had about 92 % H^- and small amounts of O^-, OH^- and Al^-. The cesiation changes the ratio of the H^- and impurity ions radically as can be seen by comparing figures 100 and 101. Without optimal cesiation, the impurities, which have higher electron affinity than hydrogen, are forming negative ions more easily than hydrogen, even though there is much more hydrogen atoms and molecules present in the plasma. When the cesium is released from the getters and a proper level of cesiation is achieved, the H^- yield increases much more than the impurities.

Figure 102 shows a summary of the H^- and electron currents extracted from the external antenna ion source as a function of the estimated cesiation level of the source.

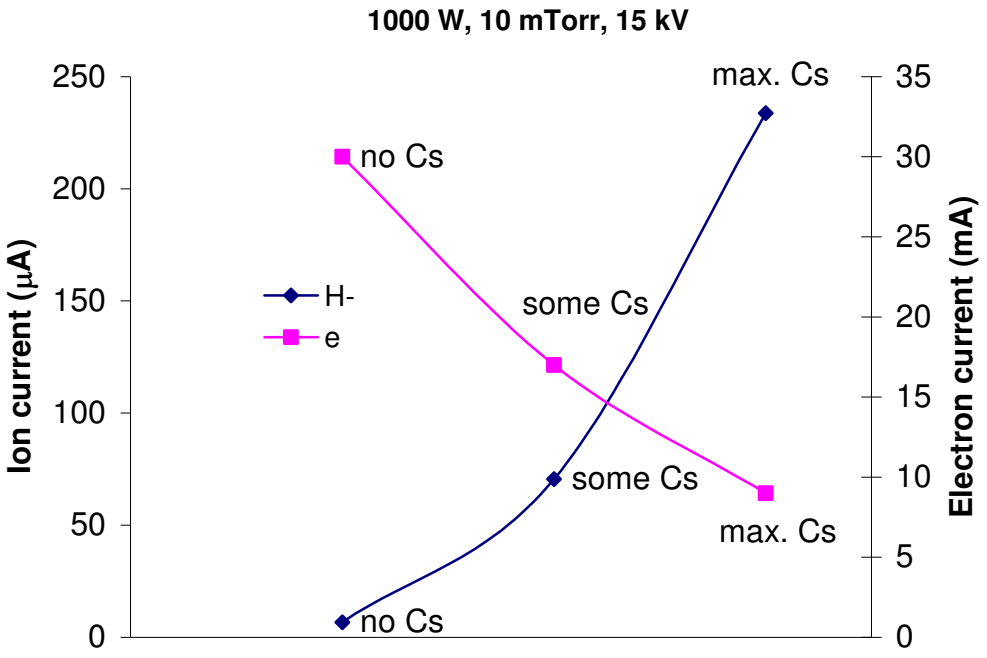

Figure 102. *The extracted H^- and electron currents at three different cesiation levels.*

The H^- current values in figure 102 were calculated by multiplying the total negative ion current with the hydrogen fraction given by the mass spectrums of figures 98, 100 and 101. Figure 102 shows clearly the huge effect of cesium on extracted H^- and electron currents. The maximum current density of volume produced H^- at 1.0 kW of RF power was determined to be 8 mA/cm^2. This value is quite high for such a low RF power, when compared to other volume H^- ion sources [36, 56]. The smallest achieved e/H^- ratio was 40, which is an order of magnitude larger than the lowest reported values from a larger multicusp- type H^- source with an internal antenna and a cesium collar around the extraction aperture [58]. It must be noted that the extracted electron and ion currents were not saturating in figure 102 suggesting that the obtained source cesiation level was not optimal. This experiment was limited to RF powers below 1.5 kW due to the heating of the quartz plasma chamber, which resulted in melting of the o-ring of the source. This problem can be overcome by using aluminum oxide (AlO) as plasma chamber material. AlO can be cooled much better than quartz and heating of the o-rings can be thus eliminated.

8. Conclusions

Traditionally positive ion beams have been considered as the best option for drivers of heavy ion fusion due to the relative ease with which intense positive ion beams can be formed. Positive beams have some serious drawbacks, which include beam-plasma instabilities, the trapping of electrons from target chamber walls and the change of the average charge state of the ions by collisions with the residual gas. This has led to a proposal of using negative ions instead. Negative ions can be stripped easily to form electrically neutral particles, which would give totally space charge neutralized beam free of instabilities. Up to now, the relatively low beam currents have been a reason for not considering negative ions as fusion drivers.

First part of this thesis was performed in an effort to study the achievable current density and beam quality with ions belonging to the halogen group in the table of elements. Halogens have the highest electron affinities of all elements, which make them the most promising candidates for negative ion driver beams. Bromine (mass number 81, electron affinity 3.36 eV) and iodine (mass number 127, electron affinity 3.06 eV) would be suitable for heavy ion fusion due to their large mass and high electron affinity. For an initial estimate of the achievable current density and beam emittance, chlorine was selected as it is available readily in gaseous form and has similar electron affinity (3.61 eV) to bromine and iodine. A multicusp- type RF driven ion source was selected for the negative chlorine experiment.

The source was first tested with oxygen plasma for correct operation and to give a reference of the effect of electron affinity on beam parameters. Current density of 5.7 mA/cm^2 for O^- and 22 mA/cm^2 for O^+ was measured at 2.0 kW of RF power. 90 % of the negative ion beam was O^-. Lowest achieved value for the electron-to-negative ion ratio was 300. The fraction of negative oxygen ions of the total negative charge density of the plasma was estimated to be 63 % by relating the extracted negative ion current and the scaled electron current.

After the oxygen measurements the test stand was prepared for chlorine operation. Maximum current density of 45 mA/cm^2 was measured at 2.2 kW RF power for negative chlorine ions. 99.8 % of the negative ion beam was Cl^-. Electron to negative ion ratio was 7, while positive to negative chlorine ion ratio was 1.3. The fraction of negative chlorine ions of the total negative charge density of the plasma was determined to be as high as 99 %.

The injection of cesium has been observed to increase the negative hydrogen ion current considerably. The effect of cesium was tested in the chlorine plasma. The ion current did not change, which is due to the already high fraction of negative chlorine in the plasma. The addition of cesium into the chlorine plasma had much bigger effect on the electron current, as it decreased by an order of magnitude. This can be explained by the collisions of electrons with the massive cesium atoms. These collisions lower the temperature and thus the influx of electrons into the extraction area.

The emittance of the positive and negative chlorine beams was determined with a pepper pot device. The normalized emittances were measured to be $0.12\,\pi \cdot mm \cdot mrad$ for positive chlorine beam and $0.14\,\pi \cdot mm \cdot mrad$ for negative chlorine beam. The similarity of the emittances and beam currents of the positive and negative chlorine ions indicate that negative halogen ions are a good candidate for drivers of heavy ion fusion in the future.

The second part of this thesis was concentrating on the development of a sputtering type surface ionization source to produce negative boron ions for semiconductor industry applications. Some existing sources of this type are relying on heavy cesiation of a lanthanum hexaboride (LaB_6) sputtering target to increase the negative boron yield to about 1 - 2 mA/cm^2. In commercial ion doping machines the cesium is an unwanted impurity, as it gradually coats the insulator surfaces of the acceleration column and causes voltage break downs. The goal of the work done for this thesis was to build an ion source capable of producing commercially attractive currents of negative boron without using cesium.

In the initial phase of the experiment, a large multicusp- type, RF driven ion source with a 20 mm diameter LaB_6 sputtering target/converter was set up for testing. Argon and xenon gases were used to create the background plasma. No negative boron atoms were observed in the measurements within the accuracy of the mass spectrometer, but large peaks corresponding to B_2^- and B_3^- clusters were seen. A very minor B_4^- cluster was also observed in some measurements. The appearance of boron clusters suggests that the structure of the LaB_6 lattice, which is an octahedron with a boron atom in each corner and a lanthanum atom in the middle, is favorable for cluster emission when bombarded by 1 keV argon ions. In the case of argon plasma, a current density of 0.14 mA/cm^2 of B_2^- and 0.09 mA/cm^2 of B_3^- was achieved. For a xenon plasma, the current densities of B_2^- and B_3^- were 0.06 mA/cm^2 and 0.08 mA/cm^2, respectively.

These currents were too low to be commercially applicable. However, by building a smaller non-cesiated ion source with higher power density, with optimized source design

and a larger converter, it should be possible to increase the negative boron currents further. To achieve this, a compact ion source with an external RF antenna and 50 mm diameter LaB_6 converter was constructed. The source was designed to optimize the B_2^- current by using an argon plasma. Thus far, 1 mA/cm^2 of B_2^- and 0.44 mA/cm^2 of B_3^- has been extracted from the external antenna source at 800 W RF power. The total extractable B_2^- ion current was determined to be 1.8 mA. These values are comparable to values reported by other research groups employing cesiated, internal antenna ion sources. The non-cesiated, external antenna ion source would offer a reliable, clean way of producing negative boron ions for ion implantation applications.

The ionization efficiency of the non-cesiated boron source was determined to be about 1.3 % at 10 mTorr source pressure. The stripping of surface produced negative ions is a limiting factor if the source pressure is above a few mTorr. The large multicusp source and the small external antenna source performed optimally at around 10 mTorr source pressure.

To lower the source operating pressure, an experiment was set up to compare the external antenna ion source performance when driven by 13.56 MHz and by 27.12 MHz RF discharges. The experiment was also aiming to minimize the operating pressures of sealed neutron generators developed in the Plasma and Ion Source Technology Group at LBNL.

The ion source performed well with both RF frequencies at source pressures above 20 mTorr. The measured hydrogen ion currents and mass spectrums were essentially the same with both frequencies. When the source pressure was decreased below 15 mTorr, the 13.56 MHz plasma started to die out much faster than the 27.12 MHz plasma. When the pressure dropped from 20 mTorr to 5 mTorr, the ion current decreased by a factor of three for the 13.56 MHz and only 17 % for the 27.12 MHz RF frequency. This is a clear indication that the higher RF frequency is better suited for low pressure ion source operation.

The suitability of the external antenna ion source was tested for volume production of H^- ions. Traditionally H^- ion sources are either filament or internal RF antenna driven multicusp sources. The disadvantage of filament sources are the contamination of the plasma from the filament and the difficulty of getting proper cesiation, which is required to optimize the H^- yields and to minimize the extracted electron current. Internal antenna RF sources, as well as filament sources, are suffering from lifetime issues at higher RF power levels. The ion source with the external antenna is not limited by the lifetime of the antenna, and the source performance proved to be on par with the two above

mentioned H^- source geometries. H^- current density of 8 mA/cm^2 was achieved at the maximum cesiation level at only 1.0 kW of RF power. The e/H^- -ratio was 40, which could be further reduced by installing a collar similar to the one used in the negative chlorine experiment around the extraction aperture. By replacing the quartz plasma chamber used in the measurements done for this thesis by aluminum oxide cylinder, the cooling of the plasma chamber can be improved considerably and thus high RF power operation and high H^- currents can be achieved easily.

References

[1] Ian G. Brown, *The Physics And Technology of Ion Sources*, Wiley & Sons, New York (1989), ISBN 0-471-85708-4

[2] F. F. Chen, *Introduction to Plasma Physics,* Plenum Press, New York (1974), ISBN 0-306-30755-3

[3] B. Chapman, *Glow Discharge Processes,* Wiley & Sons, New York (1980), ISBN 0-471-07828-X

[4] R. J. Goldston, P.H.Rutherford, *Introduction to Plasma Physics*, IOP Publishing Ltd, New Yok (1995), ISBN 0-7503-0183

[5] E. W. McDaniel, *Collision Phenomena in Ionized Gases*, Wiley & Sons, New York (1964)

[6] K-N Leung, T. K. Samec, A. Lamm, *Physics Letters A* **51**, pp.490-2 (1975)

[7] K. W. Ehlers and K. N. Leung, *Rev. Sci. Instrum*. **50**, pp. 1353 (1979)

[8] T. Morishita, M. Ogasawara, A. Hatayama, *Rev. Sci. Instrum*. **69**, pp. 968-970 (1998)

[9] R. A. Bosch, R. L. Merlino, *Phys. Fluids* **30**, pp. 1998 (1986)

[10] S. Dushman, *Rev. Mod. Phys*. **2**, pp. 381–476 (1930)

[11] Mathcad calculation software, MathSoft, Inc.

[12] K. N. Leung, *Rev. Sci. Instrum*. **71**, pp. 1064 – 1068 (2000)

[13] T. Schenkel, J. W. Staples, R. W. Thomae, *Rev. Sci. Instrum*. **73**, pp. 1017 – 1019 (2002)

[14] J. Staples, T. Schenkel*, Proceedings of the 2001 Particle Accelerator Conference*, pp. 2108 – 2110 (2001)

[15] Y.-K. Kim and M.E. Rudd, *Phys. Rev.* A **50**, pp. 3954 (1994).

[16] K. W. Ehlers and K. N. Leung, *Rev. Sci. Instrum.* **52**, pp. 1452 (1981)

[17] H. Massey, *Negative Ions*, Cambridge University Press (1976).

[18] T. Andersen, H. K. Haugen and H. Hotop, *J. Phys. Chem. Ref. Data*, **28**, pp. 1511 (1999)

[19] L. G. Christophorou, *Electron Molecule Interactions and their Applications: Volume 2*, Academic Press, New York (1984).

[20] Sze, S. M., *Semiconductor Devices – Physics and Technology*, Wiley & Sons, New York (1985).

[21] K. W. Ehlers, K. N. Leung, *Rev. Sci. Instrum*. **51**, pp. 721 – 727 (1980)

[22] K. Wasa, S. Hayakawa, *Handbook of Sputter Deposition Technology: Principles, Technology and Applications*, Noyes Publications, (1992), ISBN: 0815512805

[23] P. Sigmund*, Phys. Rev*. **184**, pp. 383 (1969)

[24] G. K. Wehner, D. L. Rosenberg, *J. Appl. Phys*. **31**, pp. 177 (1960)

[25] A. Wucher, B. J. Garrison, *Phys. Rev. B* **46** (8), pp. 4855 (1992)

[26] K. Franzreb, A. Wucher, H. Oechsne, *J. Anal. Chem.* **341**, pp. 7 (1991)

[27] J. Ishikawa, H. Tsuji, Y. Gotoh, S. Azegami, *Particles and Fields Series 53: Production and Neutralization of Negative Ions and Beams, 6th Int. Symp*., AIP Conference Proceedings No. 287, pp. 66 – 74 (1994)

[28] M. L. Yu, *Phys. Rev. Lett.* **40**, 574 (1978)

[29] B. Wolf, *Handbook of Ion Sources,* CRC Press, Inc. (1995), ISBN 0-8493-2502-1

[30] G. D. Alton, *Surf. Sci.* **175**, pp. 226 – 240 (1986)

[31] P. Allison, J. D. Sherman, H. V. Smith, *Report LA-8808-MS*, Los Alamos Nat. Lab., (1981)

[32] A. J. T. Holmes, *Phys. Rev. A* **19**, pp. 389 (1979)

[33] R. Becker, W. B. Herrmannsfeldt, *Rev. Sci. Instrum*. **63**, pp. 2756 (1992)

[34] R. Becker, K. N. Leung and W. Kunkel, *Rev. Sci. Instrum*. **69**, pp. 1107 (1998)

[35] M. A. Leitner, D. C. Wutte, and K. N. Leung, *Rev. Sci. Instrum*. **69**, pp. 965 (1998)

[36] T. Kuo, R. Baartman, G. Dutto, S. Hahto, E. Liukkonen and J. Ärje, *Rev. Sci. Instrum.* **73**, pp. 986 (2002)

[37] S. Hahto, K. Leung, A. Persaud, and J. Reijonen, *Rev. Sci. Instrum*. **73,** pp. 967 (2002)

[38] C. F. Barnett, *Atomic Data For Fusion, ORNL-6086 Volume 1-3*, (1990)

[39] J. E. Boers, *Proc. of the 1995 Particle Accelerator Conference*, pp. 2312 (1995)

[40] P. Spädtke, *KOBRA3-INP user manual, version 3.39* (2000)

[41] The U.S. Program of Fusion Energy Research and Development, *The President's Committee of Advisors on Science and Technology (PCAST), (1995)*

[42] J. Reijonen , M. Eardley, R. Keller, J. Kwan and K.N. Leung, *Proceedings of the 1999 Particle Accelerator Conference*, pp. 1943 (1999)

[43] L. R. Grisham, *Nucl. Instrum. Meth. Phys. Res.* **A 464**, pp. 315 (2001)

[44] S. K. Hahto, S. T. Hahto, K. N. Leung, J. W. Kwan and L. R. Grisham, *Rev. Sci. Instrum*. **74** (6), (2003)

[45] M. A. Leitner, R. A. Gough, K. N. Leung, M. L. Rickard, P. K. Scott, A. B. Wengrow, M. D. Williams, and D. C. Wutte, *Rev. Sci. Instrum*. **69**, pp. 962 (1998)

[46] J. H. Billen, *Poisson Superfish Manual*, Los Alamos National Laboratory

[47] K. N. Leung, K. W. Ehlers and M. Bacal, *Rev. Sci. Instrum*. **54**, pp. 56 (1983)

[48] L. T. Perkins, G. J. De Vries, P. R. Herz, W. B. Kunkel, K. N. Leung, D. S. Pickard, A. Wengrow and M. D. Williams, *Rev. Sci. Instrum*. **67**, pp. 1057 (1996)

[49] Y. Lee, *Ph.D. Thesis, University of California, Berkeley* LBNL-41980 (1998)

[50] K. N. Leung, C. A. Hauck, W. B. Kunkel and S. R. Walther, *Rev. Sci. Instrum.* **60**, pp. 531 (1989)

[51] J. Ishikawa, *Rev. Sci. Instrum*. **71**, pp. 1036 (2000)

[52] G. D. Alton, *Rev. Sci. Instrum*. **65**, pp. 1141 (1994)

[53] J. F. Ziegler, SRIM2003 user manual, (2003)

[54] SIA Roadmap for USLI Technology, 1994.

[55] N. Cerullo, J. Esposito, K. N. Leung and S. Custodero, *Rev. Sci. Instrum*. **73**, pp. 3614 (2002)

[56] R. Keller *et. al., Rev. Sci. Instrum*. **73**, pp. 914 (2002)

[57] M. Tuszewski, *Phys. Plasmas* **4** (5), pp. 1922 (1997)

[58] K. Saadatmand, G. Arbique, J. Hebert, R. Valicenti and K. N. Leung, *Rev. Sci. Instrum*. **67**, pp. 1318 (1996)